

**IN VIVO ASSESSMENT OF LAMINA CRIBROSA MICROSTRUCTURE IN
GLAUCOMA**

by

Bo Wang, B.S.

Bachelor of Science in Bioengineering, University of Pittsburgh, 2010

Submitted to the Graduate Faculty of
Swanson School of Engineering in partial fulfillment
of the requirements for the degree of
Doctor of Philosophy in Bioengineering

University of Pittsburgh

2016

UNIVERSITY OF PITTSBURGH
SWANSON SCHOOL OF ENGINEERING

This dissertation was presented

by

Bo Wang

It was defended on

March 14, 2016

and approved by

Gadi Wollstein, MD, Professor, Department of Ophthalmology and Bioengineering

Ian A. Sigal, PhD, Assistant Professor, Department of Ophthalmology and Bioengineering

George D. Stetten, MD, PhD, Professor, Department of Bioengineering

Richard A. Bilonick, PhD, Assistant Professor, Department of Ophthalmology

Dissertation Director: Joel S. Schuman, MD, Professor, Department of Ophthalmology and

Bioengineering

Copyright © by Bo Wang

2016

IN VIVO ASSESSMENT OF LAMINA CRIBROSA MICROSTRUCTURE IN GLAUCOMA

Bo Wang, Ph.D.

University of Pittsburgh, 2016

Glaucoma is an optic neuropathy that is the second leading cause of blindness worldwide. The disease is characterized by damage to the retinal ganglion cells, resulting in irreversible vision loss. While the exact pathogenesis remains unclear, damage due to glaucoma is believed to first occur at the lamina cribrosa (LC), a collagenous meshwork in the optic nerve head through which all retinal ganglion cell axons pass on their way to the brain.

The mechanical theory of glaucoma postulates that elevated intraocular pressure deforms the LC, leading to a biological cascade resulting in retinal ganglion cell death. However, the interaction between intraocular pressure and glaucoma is complex; a substantial heterogeneity exists in the intraocular pressure at which a given patient experiences glaucoma. Recent studies have identified that perhaps intracranial pressure, which acts posterior to the LC, may play an important role in the disease process.

Given the complex 3D microstructure of the LC, *in vivo* studies thus far have been limited to assessment of changes in its surface. However, because the axons are traversing through the entire volume of the LC, the axonal damage can occur at any level of the LC, rather than only at its surface. Therefore, full understanding of the damage caused by glaucoma requires systematic characterization of the 3D LC microstructure.

In order to better characterize the 3D LC microstructure, we demonstrate here a novel automated 3D LC segmentation method that is reproducible and capable of accurately detecting

the LC microstructural component. Using our segmentation analysis, we find in a primate model that the LC microstructure deforms according to both intraocular pressure as well as intracranial pressure, with significant interaction between the two. We then move to the translational aspect of our study to characterize the healthy LC in human eyes and identify a number of structural and biomechanical differences in the LC microstructure compared to glaucoma eyes. Our findings demonstrate that a novel automated 3D assessment of the LC microstructure is capable of 1) identifying in vivo difference in the LC microstructure and LC biomechanics in glaucoma eyes and 2) improving our understanding of glaucoma pathogenesis.

TABLE OF CONTENTS

PREFACE.....	XIX
ABBREVIATIONS.....	XXI
1.0 INTRODUCTION.....	1
1.1 GLAUCOMA	1
1.2 LAMINA CRIBROSA.....	3
1.3 THE ROLE OF INTRAOCULAR PRESSURE AND INTRACRANIAL PRESSURE.....	5
1.4 OPTICAL COHERENCE TOMOGRAPHY	8
1.5 IN VIVO ASSESSMENT OF THE LAMINA CRIBROSA	13
1.6 PROJECT AIMS	15
1.6.1 Aim 1: To develop and evaluate a semi-automated method of segmentation and analysis of LC microstructure.....	15
1.6.2 Aim 2: To evaluate the effects of acute modulation of both intraocular and intracranial pressure on the primate LC	15
1.6.3 Aim 3: To characterize the effects of glaucoma on the human LC.....	16
2.0 RECRUITMENT OF HUMAN SUBJECTS.....	17
2.1 INCLUSION CRITERIA.....	17
2.2 EXCLUSION CRITERIA.....	18
2.3 TESTING PROTOCOL.....	18

3.0	DESCRIPTION OF DEVICES.....	19
3.1	OPTICAL COHERENCE TOMOGRAPHY	19
3.1.1	Spectral Domain Optical Coherence Tomography	19
3.1.1.1	Bioptigen SD-OCT	19
3.1.1.2	Cirrus HD-OCT	20
3.1.2	Swept Source Optical Coherence Tomography	21
3.2	VISUAL FIELD TESTING	22
4.0	DEVELOPMENT AND EVALUATION OF LAMINA CRIBROSA SEGMENTATION.....	23
4.1	EXPERIMENT 1-1: TO CREATE A SEMI-AUTOMATED SEGMENTATION AND ANALYSIS METHOD OF THE LC MICROSTRUCTURE.....	23
4.1.1	Methods	24
4.1.2	Results.....	28
4.1.3	Discussion	30
4.2	EXPERIMENT 1-2: TO ASSESS THE REPRODUCIBILITY OF A SEMI-AUTOMATED SEGMENTATION METHOD OF LC MICROSTRUCTURE.....	33
4.2.1	Methods	34
4.2.1.1	Image Acquisition and Processing with Swept Source-OCT	34
4.2.1.2	Statistical Analysis	34
4.2.2	Results.....	35
4.2.3	Discussion	40
4.3	SUMMARY	42
5.0	EFFECT OF INTRAOCULAR AND INTRACRANIAL PRESSURES ON THE LAMINA CRIBROSA MICROSTRUCTURE	44

5.1	EXPERIMENT 2-1: ASSESSING THE EFFECTS OF ACUTE IOP AND ICP CHANGE ON LC MICROSTRUCTURE.....	44
5.1.1	Animals and Methodology	45
5.1.1.1	Animals	45
5.1.1.2	Anesthesia	46
5.1.1.3	Pressure Control	46
5.1.1.4	Experimental Setting	47
5.1.1.5	OCT Imaging.....	48
5.1.1.6	Image Analysis.....	48
5.1.1.7	Reproducibility.....	50
5.1.1.8	Statistical Analysis	51
5.1.2	Results.....	51
5.1.2.1	Repeatability.....	53
5.1.2.2	How LC Microstructure Changed with IOP.....	53
5.1.2.3	How LC microstructure changed with ICP.....	54
5.1.3	Discussion	54
5.2	EXPERIMENT 2-2: ASSESSING THE RESPONSE OF LC MICROSTRUCTURE TO BOTH IOP AND ICP.....	56
5.2.1	Animals and Methodology	57
5.2.1.1	Statistical Analysis – Model 1, Linear Models	57
5.2.1.2	Statistical Analysis – Model 2, Interaction Model	58
5.2.1.3	Statistical Analysis – Model 3, Quadratic model	59
5.2.2	Results.....	60
5.2.2.1	Model 1 – TLPD and Quality.....	60

5.2.2.2	Model 1 – IOP, ICP and Quality	61
5.2.2.3	Model 2 – Interaction models.....	62
5.2.2.4	Model 3 – Quadratic Model	68
5.2.3	Discussion	71
5.2.3.1	Model 1 – Linear Models.....	72
5.2.3.2	Model 2 – Interactions model.....	74
5.2.3.3	Model 3 – Quadratic Model	75
5.3	SUMMARY	76
6.0	CHARACTERIZATION OF THE EFFECT OF GLAUCOMA ON HUMAN LAMINA CRIBROSA	77
6.1	3-1: COMPARING LC MICROSTRUCTURE IN HEALTHY AND GLAUCOMATOUS EYES	77
6.1.1	Methods	78
6.1.1.1	Statistical Analysis	78
6.1.2	Results.....	79
6.1.3	Discussion	82
6.1.3.1	Age Related Changes	83
6.1.3.2	Comparing Healthy and Glaucomatous Eyes	83
6.1.3.3	Microstructure Parameters and Functional Damage.....	84
6.2	EXPERIMENT 3-2: DIFFERENCES IN INDIVIDUAL LC PORE PATH BETWEEN HEALTHY AND GLAUCOMATOUS EYES	85
6.2.1	Methods	86
6.2.1.1	Tracking Analysis	86
6.2.1.2	Assessment of Pore Trajectory Relative to the Disc	87
6.2.1.3	Assessment of Pore Tortuosity.....	89

6.2.1.4	Statistical Analysis	89
6.2.2	Results.....	89
6.2.2.1	Depth of LC Pore Path Tracking.....	89
6.2.2.2	Pore Trajectory Relative to the Disc	89
6.2.2.3	Pore Tortuosity.....	90
6.2.3	Discussion	91
6.2.3.1	Depth of LC Pore Path Tracking.....	92
6.2.3.2	Pore Trajectory	93
6.2.3.3	Pore Tortuosity.....	94
6.3	EXPERIMENT 3-2: DIFFERENCES IN INDIVIDUAL LC PORE PATH BETWEEN HEALTHY AND GLAUCOMATOUS EYES	95
6.3.1	Methods	96
6.3.1.1	Total Lamina Cribrosa Assessment	96
6.3.1.2	Individual Pore Analysis	98
6.3.2	Results.....	102
6.3.2.1	Total Lamina Cribrosa Assessment	102
6.3.2.2	Individual Pore Analysis	104
6.3.3	Discussion	106
6.3.3.1	Total Lamina Cribrosa Assessment	107
6.3.3.2	Individual Pore Analysis	108
6.4	SUMMARY	109
7.0	DISSERTATION SYNOPSIS.....	110
7.1	LIMITATIONS.....	111
7.2	FUTURE WORK.....	112

7.3	CONCLUSION	113
	BIBLIOGRAPHY	114

LIST OF TABLES

Table 1.	Average measurement and imprecision estimate for each segmentation method using SS-OCT. Obs – Observer. CTVF – Connective Tissue Volume Fraction.....	30
Table 2.	Average and imprecision for lamina cribrosa parameters.	39
Table 3.	Relative imprecision of lamina cribrosa parameters in relation to clinical diagnosis.	40
Table 4.	Estimate of the effect of intraocular pressure (IOP) and image quality on lamina cribrosa (LC) microstructure. Bold font marked statistically significant effect. Au – arbitrary units.	53
Table 5.	Estimate of the effect of intracranial pressure (ICP) and image quality on lamina cribrosa (LC) microstructure. Bold font marked statistically significant effect.	54
Table 6.	List of model name as well as the parameters used inside the model.....	58
Table 7.	List of interaction models tested as part of the analysis.	59
Table 8.	Estimate of the effect of translaminar pressure difference (TLPD) and image quality on lamina cribrosa (LC) microstructure. Bold font marked statistically significant effect. Au – arbitrary units.	61
Table 9.	Estimate of the effect of intraocular pressure (IOP), intracranial pressure (ICP) and image quality on lamina cribrosa (LC) microstructure. Bold font marked statistically significant effect. Au – arbitrary units.	62
Table 10.	Comparison of the various models with interactions for beam thickness. Lower AIC denotes the better model. * denotes interaction effect between the variables. Bold denotes best performing model as judged by AIC.....	63
Table 11.	Comparison of the various models with and without interactions for pore diameter. Lower AIC denotes the better model. * denotes interaction effect between the variables. Bold denotes best performing model as judged by AIC.....	64
Table 12.	Comparison of the various models with and without interactions for beam thickness to pore diameter ratio. Lower AIC denotes the better model. * denotes interaction effect between the variables. Bold denotes best performing model as judged by AIC.	65

Table 13. Comparison of AIC of models with only interactions with models with interactions and quadratic components..... 69

Table 14. Difference in LC microstructure between healthy and glaucomatous eyes. The fixed effect represents the linear mixed effect model of the difference between healthy and glaucomatous eyes. Positive fixed effect indicates an increase in the parameter with disease. Statistically significant parameters are marked with bold font. 81

Table 15. Structure function relationship between LC microstructure and visual fields mean deviation (VF MD). The fixed effect represents the linear mixed effect model of change per VF MD. Positive fixed effect indicates an increase in the parameter with worsening disease. Bold indicates statistically significant results..... 82

LIST OF FIGURES

Figure 1.	(A) Cross sectional diagram of the eye. Blue box indicates the location of the optic nerve head. Black box indicates the zoomed in region of (B). (B) Outflow pathway (blue dashed line) is altered in open angle glaucoma while in angle closure glaucoma (red dashed line), the outflow pathway is occluded and aqueous humor access to the trabecular meshwork is blocked. Adapted from nei.nih.org.....	1
Figure 2.	Characterization of the connective tissue changes of the optic nerve head and lamina cribrosa with glaucoma. (A) A healthy optic nerve head, with the lamina cribrosa beams and pores. Note the detailed microstructure of the lamina cribrosa. (B) Glaucoma damage results in thinning, excavation and posterior insertion of the lamina cribrosa. Adapted from Quigley et al. [24]	4
Figure 3.	Diagram of the optic nerve head demonstrating the location at which intraocular pressure (IOP – light blue) and intracranial pressure (ICP – red) acts on the lamina cribrosa. While IOP acts anteriorly to the optic nerve head, the ICP acts posteriorly and circumferentially.	7
Figure 4.	Diagram of time-domain OCT device. Adapted from Marschall et al. [56].....	9
Figure 5.	Description of the scan patterns used in this study. (A) A-scans are an individual scan down the depth of the tissue, red line indicate a graphical representation of the reflectivity along an individual A-scan. (B) B-scans represent a linear collection of adjacent A-scans and is typically used for cross-sectional visualization of tissue. (C) A 3D volume is generated by putting together a series of consecutive B-scans. (D) A C-mode or en-face image, is generated by reslicing the volume at a given plane (blue rectangle).....	10
Figure 6.	Diagram of spectral-domain OCT. Adapted from Marschall et al. [56].....	11
Figure 7.	Diagram of swept source OCT system. Adapted from Marschall et al. [56].....	12
Figure 8.	(A) Sagittal sections showing LC anterior surface (red dashed line) and posterior LC surface (yellow dashed line). Current in vivo studies involve manually analyzing these sections for macrostructural features such as total thickness. (B) Coronal sections showing LC microstructure.....	14
Figure 9.	Commercial spectral domain OCT scan of the optic nerve by Cirrus HD-OCT. The analysis show thinning of the retinal nerve fiber layer in both the right and left eye,	

	slightly more prominent in the left. The summary measurement used was average retinal nerve fiber layer thickness (black box).....	21
Figure 10.	Initialization of the images. (1) The series of B-scans are first resliced (white dashed line) to look at (2) a series of C-mode slices. (3) A Gaussian filter is applied to remove image noise.	25
Figure 11.	Automated segmentation of the LC microstructure. After (1) de-noising the image, the entire stack underwent contrast limited adaptive histogram equalization (CLAHE) and (3) local thresholding and masking to identify the pores. (4) Segmentations of the pores were overlaid on top of the original image.....	26
Figure 12.	The unprocessed C-mode slice (a) and corresponding segmentation (b) for a scan of a healthy eye taken with the SS-OCT device. For pores identified by both automated and manual segmentations, the automated pores are colored red and the manual ones are colored blue, so that overlapping segmentation appears as purple. Pores identified only by the automated method are colored yellow and those seen solely in the manual segmentation are colored green. Pores detected only by manual segmentation were mostly located adjacent to blood vessel shadow margins.....	29
Figure 13.	Two consecutive optical coherence tomography scans of the lamina cribrosa of the same eye. Original C-mode (left) and segmentation overlain (right) where beams (green) and pores (red) are marked. Differences in segmentations between the two scans primarily existed due to local disparities in regions analyzed.....	36
Figure 14.	Two consecutive optical coherence tomography scans of the lamina cribrosa of the same eye. Original C-mode (left) and segmentation overlain (right) where beams (green) and pores (red) are marked. Differences in segmentations between the two scans (red arrows) primarily existed due to local disparities in regions analyzed.	37
Figure 15.	Shifts in the scanning angle alter B-scan (A) and C-mode (B) images and alter the microstructure seen on a single frame from the center of the volume. The scan angle changes were simulated using image processing software (ImageJ).....	38
Figure 16.	3D view of lamina cribrosa beams demonstrated the similarity of the microstructural features (same eye as Figure 13).....	39
Figure 17.	(A) Experimental setup. Intraocular pressure (IOP) and intracranial pressure (ICP) were controlled using a gravity-based perfusion system. OCT imaging of the lamina cribrosa (LC) (red box) was performed 5 minutes after altering IOP and ICP. At every given ICP, IOP was altered and the OPTIC NERVE HEAD was imaged after 5 minutes at every IOP condition. After completing all IOP conditions, a new ICP was set and the IOP conditions repeated.	47
Figure 18.	Assessment of segmentation quality. Examples of images rated as 1, 2, and 3.	49
Figure 19.	Image analysis procedure. (A) Images were adjusted for isotropic dimensions, (B) and rotated to match the angle of Bruch membrane opening (BMO). (C) Images were	

translated in the axial direction to match the axial height of the BMO. (D) The microstructures were aligned manually via 3D rotation and translation. (E) Visible LC was denoted and a common overlapping region (white color region) was used for analysis..... 50

Figure 20. Image quality metrics. Histogram of (A) IOP setting per image quality and (b) ICP setting per image quality (C) image quality per monkey..... 52

Figure 21. Diagram demonstrating the optic nerve under two different pressure conditions. In both cases, the translaminar pressure difference would be 5mmHg..... 56

Figure 22. Change in LC beam thickness to pore diameter ratio with intraocular (IOP) and intracranial (ICP) pressure. (A) Contour plot showing change in beam pore ratio as a function of IOP and ICP. Black lines indicate the contour line at a particular value. Transparent gray dots indicate points sampled in the dataset. A sample of the contour plot at a set of (B) ICP (ICP = 10mmHg, light green; ICP = 40mmHg, dark green) and (C) IOP (IOP = 10mmHg, purple, IOP = 45mmHg) demonstrate the complex interaction between IOP and ICP on beam thickness. 66

Figure 23. Change in LC pore diameter with intraocular (IOP) and intracranial (ICP) pressure. (A) Contour plot showing change in beam pore ratio as a function of IOP and ICP. Black lines indicate the contour line at a particular value. Transparent gray dots indicate points sampled in the dataset. A sample of the contour plot at a set of (B) ICP (ICP = 10mmHg, light green; ICP = 40mmHg, dark green) and (C) IOP (IOP = 10mmHg, purple, IOP = 45mmHg) demonstrate the complex interaction between IOP and ICP on pore diameter. 67

Figure 24. Change in LC beam thickness to pore diameter ratio with intraocular (IOP) and intracranial (ICP) pressure. (A-C) Contour plot showing change in beam thickness as a function of IOP and ICP. Black lines indicate the contour line at a particular value. Transparent gray dots indicate points sampled in the dataset. A sample of the contour plot at a set of (B) ICP (ICP = 10mmHg, light green; ICP = 40mmHg, dark green) and (C) IOP (IOP = 10mmHg, purple, IOP = 45mmHg) demonstrate the complex interaction between IOP and ICP on beam thickness to pore diameter ratio..... 68

Figure 25. Quadratic model of how IOP and ICP influence beam thickness. (A) Heat map of how IOP and ICP affect the beam thickness, red indicates lower values, while yellow indicate higher value. Blue dots indicate the points with actual data in the results. Lines indicates the samplings taken to create plot (B) and (C). (B) Beam thickness to pore diameter as an influence of IOP, with two separate ICP shown (10 – brown, 45 – green). (C) Beam thickness to pore diameter as an influence of ICP, with two separate IOP shown (10 – purple, 45 – teal). 69

Figure 26. Quadratic model of how IOP and ICP influence pore diameter. (A) Heat map of how IOP and ICP affect the beam thickness, red indicates lower values, while yellow indicate higher value. Blue dots indicate the points with actual data in the results. Lines indicates the samplings taken to create plot (B) and (C). (B) Beam thickness to

	pore diameter as an influence of IOP, with two separate ICP shown (10 – brown, 45 – green). (C) Beam thickness to pore diameter as an influence of ICP, with two separate IOP shown (10 – purple, 45 – teal).....	70
Figure 27.	Quadratic model of how IOP and ICP influence beam thickness to pore diameter ratio. (A) Heat map of how IOP and ICP affect the beam thickness to pore diameter ratio, red indicates lower values, while yellow indicate higher value. Blue dots indicate the points with actual data in the results. Lines indicates the samplings taken to create plot (B) and (C). (B) Beam thickness to pore diameter as an influence of IOP, with two separate ICP shown (10 – brown, 45 – green). (C) Beam thickness to pore diameter as an influence of ICP, with two separate IOP shown (10 – purple, 45 – teal).....	71
Figure 28.	Lamina cribrosa C-mode of healthy (A-B) and glaucomatous (C-D) eyes. No systematic differences are subjectively apparent between healthy and glaucomatous eyes.....	79
Figure 29.	Segmentation examples. (A) C-mode stacks of the LC of a healthy eye stepping down 50 μm slices. (B) The same slices after segmentation with laminar beams in green and laminar pores in red. 3D reconstruction of the LC (C) beams and (D) pores.....	80
Figure 30.	(A) Original C-mode view of the lamina cribrosa. Red outline represented the region that is zoomed in part (C). (B) Pore paths were traced with respect to depth via the centroid of the segmented pores. (C) 3D view of a tracing from a subset of pores (27 out of 81).....	87
Figure 31.	(A) Method of identification of pore path relative to the center of the optic nerve. Two sample paths: one moving towards the optic nerve center (path 1, blue) and was defined as a positive value and one moving away from the center (path 2, green) and defined as a negative value. (B) Example of LC identified to have pores going towards the optic nerve center (vertical red line) and (C) away from the center (vertical red line).....	88
Figure 32.	(A) Schematic demonstration of examples of negative path change (pores path travel away from ON center going from anterior to posterior) and positive path change (pores path travel towards the ON center). (B) Boxplot of pore path change with respect to diagnosis (H – healthy, GS – glaucoma suspect, GL – glaucomatous eyes) and (C) scatter plot of pore path change with visual field mean deviation.....	90
Figure 33.	(A) Pore tortuosity was defined by dividing the distance traveled by the pore centroid (yellow line) by the shortest distance between the top and bottom pores (purple line). (B) Schematic showing examples of low tortuosity (green) and high tortuosity (red). (C) Boxplot of tortuosity as a function of diagnosis (H – healthy, GS – glaucoma suspect, GL – glaucomatous eyes). (D) Probability density distribution of pore tortuosity as a function of disease (Red – healthy, Blue – glaucoma suspect, Red –	

- glaucomatous eyes). (E) Pore tortuosity as a function of visual field mean deviation, with the green lines denoting the 95% confidence interval of the healthy eyes. 91
- Figure 34. C-mode scans (top row) at baseline (left column) and elevated IOP (right column). Magnification (middle row) shows changes in LC beam and pore microstructure with elevated IOP, such as altered pore size (green arrow). Segmented images (bottom row) with the automated outline overlain in purple. 96
- Figure 35. Ophthalmodynamometer. The head of the device (left) is applied to the eye to elevated intraocular pressure. Adapted from Kagemann et al. [144]. 97
- Figure 36. Automated identification of corresponding pores at baseline pressure (left) and at elevated pressure (right). The matching pores between the two scans were numbered so that they correspond to the number in the elevated IOP scan. Note that even in scans with bad quality, accurate identification of pores were achieved. 99
- Figure 37. Method for determining range of maximum and minimum pore size change due to chance. The actual pore size (black circle) is allowed to increase (red circle) or decrease (blue circle) in size 1 full pixel thickness all the way around the pore. This full thickness increase is significantly larger than the imprecision of the measurement. This is used to create a boundary beyond which pore size change is unlikely to have occurred due to chance. 100
- Figure 38. Assessment of individual pore area change. (A) Examples of a series of pores at baseline (left) and under elevated IOP (right). Pores that increase in size was colored red, while pores that decreased in size in blue. (B) Plot of how change in pore area was dependent on the original pore area. Green represents no change in pore area, which results in a log base 2 change of 0. 101
- Figure 39. One LC C-mode (out of 61) under two pressure conditions showing the identification of individual LC pores at baseline and with elevated pressure. Matching pores are identified by individual number. Areas near blood vessels and with poor visibility were excluded from analysis. 102
- Figure 40. Boxplots of (A) beam thickness, (B) pore diameter and (C) beam thickness to pore diameter ratio changes between baseline to 30 Grms. Changes from baseline to 50 Grms are presented in D – F. 103
- Figure 41. Scatterplot of (A) beam thickness, (B) pore diameter and (C) beam thickness to pore diameter ratio change under a force of 30 Grms compare to the change under at a force of 50 Grms. Black line is the equality line. Green – healthy, blue – glaucoma suspects, red – glaucoma. 104
- Figure 42. Boxplot of percent change in pore area under IOP elevation between the diagnostic categories. H – healthy, GS – glaucoma suspect, GL – glaucoma. 105
- Figure 43. Individual LC pores change as a function of pore area at baseline with most changes occurring in smaller pores and the moving average is consistently above zero. 106

PREFACE

This thesis and the research described within was truly a team effort, which could not have been accomplished without the help, guidance, and support of the Glaucoma Imaging Group at the University of Pittsburgh. Over the last 4 years, I have had the opportunity to learn tremendous amounts of information with regards to OCT imaging, glaucoma, and ophthalmology. Although I am still far from being an expert in any of these fields, the work done here has given me a desire to dedicate myself towards learning, understanding, and improving the diagnosis and treatment of ocular diseases.

The most important element of any great group are the members who contribute their unique skills set as well as quirks. Dr. Schuman, thank you for your mentorship, support, and belief in me through this process. You, Dr. Wollstein, and Dr. Ishikawa have shown me that it is not always necessary to have a PhD to perform great research. Dr. Wollstein, I am grateful for your patience and constant guidance during my summers in lab and during graduate school. You have helped me overcome many hurdles in designing and carrying out the experiments included in this thesis. Dr. Ian Sigal, I thank you for all our discussions on ocular biomechanics, as well as life in general. Dr. Bilonick, thank you for showing me the beauty of R and statistics. Dr. Ishikawa, I appreciate all the help you have provided with the image analysis tools described in this thesis. Dr. Kagemann, I appreciate you teaching me so much about OCT. I would like to express my thanks to the fellow student members of GIG who have supported me along the way,

especially Zach, Jess, Katie, Dingle and Tigran, without whose help much of this work would not have been accomplished. This thesis is as much yours as it is mine.

Thank you to the friends I have made in Pittsburgh, who had provided moral support throughout this process, especially the many of you who have played soccer with me over the years in various clubs, leagues and pickup games and managed to keep me off the couch.

Of course, this thesis would not have been possible without the loving support of my parents, who have always taught me that anything is possible as long as I put my mind to it. Last but not least, I would like to thank my wonderful wife Carolyn, who has somehow put up with me over the years, and recently gave birth to our beautiful daughter while navigating through residency. I am eternally grateful for your companionship, love, and support. I look forward to our future adventures together.

ABBREVIATIONS

3D – three-dimensional

A-scan – axial scan

B-scan – cross sectional scan

C-mode – coronal section of volume

ICP – intracranial pressure

IOP – intraocular pressure

TLPD – translaminar pressure difference (IOP – ICP)

LC – lamina cribrosa

OCT – optical coherence tomography

SD-OCT – spectral domain optical coherence tomography

SS-OCT – swept source optical coherence tomography

AIC – Akaike Information Criterion

1.0 INTRODUCTION

1.1 GLAUCOMA

First paragraph. Glaucoma is an optic neuropathy that is the second leading cause of blindness worldwide.[1] An estimated 61 million people suffer from glaucoma, and of those, 8.4 million are bilaterally blind from the disease.[2] As glaucoma is still primarily a disease of aging, [3], [4] disease prevalence is expected to increase in the coming years due to general aging of the world's population.[5] This impending increase in disease burden strongly argues for the need to identify as well as improve our understanding of the disease.

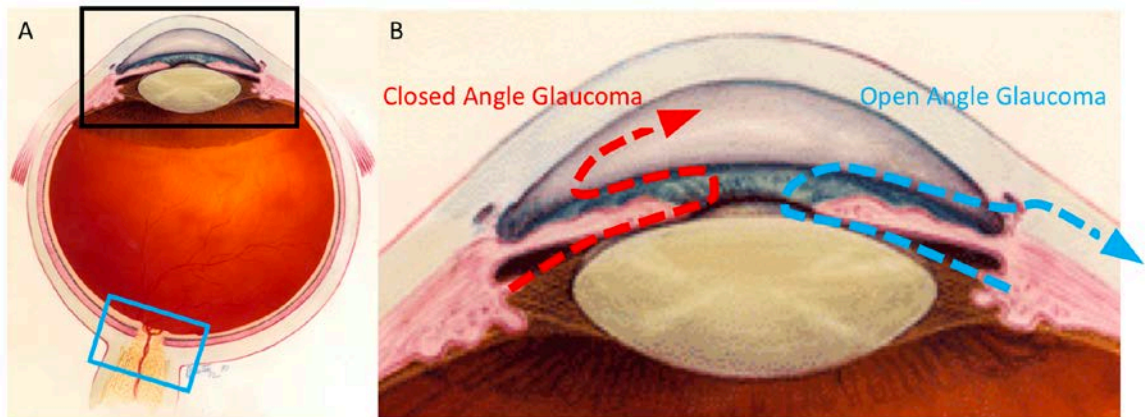


Figure 1. (A) Cross sectional diagram of the eye. Blue box indicates the location of the optic nerve head. Black box indicates the zoomed in region of (B). (B) Outflow pathway (blue dashed line) is altered in open angle glaucoma while in angle closure glaucoma (red dashed line), the outflow pathway is occluded and aqueous humor access to the trabecular meshwork is blocked. Adapted from nei.nih.org.

While initially thought of only as a disease of elevated intraocular pressure, [6] the definition of glaucoma has evolved considerably since its discovery. Presently, glaucoma is defined as a range of disorders resulting in characteristic damage to the optic nerve of the eye (Figure 1A). [7] The optic nerve is a region in the posterior eye where all retinal ganglion cell axons from the entire eye converge on their way to the brain. Damage to the optic nerve due to glaucoma results in loss of the retinal ganglion cell axons that send the visual input the brain. This clinically manifests as visual field loss that gradually worsen along the course of the disease. In all types of glaucoma, it is believed that intraocular pressure is the main culprit for damage to the optic nerve.

The intraocular pressure causing damage to the optic nerve in glaucoma is controlled in the front of the eye. As seen by the blue dashed line in Figure 1B, the ciliary body secretes aqueous humor, which flows to the anterior chamber through the pupil. The aqueous humor leaves the anterior chamber via the trabecular meshwork, Schlemm canal and episcleral veins.

Glaucoma is typically divided into two major categories: open-angle glaucoma [8], [9] and closed angle glaucoma. [10] In open angle glaucoma, the aqueous humor has free access to the trabecular meshwork, which drains the fluid out of the eye (Figure 1). Despite having free access to the trabecular meshwork, there is still damage to the optic nerve head of the eye, with a wide variability in terms of pressure at which damage occurs. While there are no externally visible abnormality of the trabecular meshwork, this elevation in pressure is caused by poorly functioning trabecular meshwork, [11] clogged materials in the meshwork [12] or loss of trabecular meshwork cells, [13] as well as potential defects in the downstream drainage system. In closed angle glaucoma, the access to the trabecular meshwork is blocked leading to an increase in intraocular pressure (Figure 1). Closed angle glaucoma is typically more common in

East Asian ancestry. [14] While both types of glaucoma lead to optic neuropathy and visual fields loss, their pathogenesis and clinical presentation are quite distinct.

1.2 LAMINA CRIBROSA

While glaucoma result in pathologic changes throughout the eye [11] and visual system, [15], [16] the primary focus of this thesis is in assessing the optic nerve head of the eye. There exists considerable evidence that the lamina cribrosa within the optic nerve head play an important role in the pathogenesis of glaucoma. [17] It is a fenestrated connective tissue meshwork that provides mechanical support and nourishment for the retinal ganglion cell axons on their way from the eye to the brain. It is also a mechanical weak point in the eye and is thought to be the primary site of glaucomatous damage.[18] Early studies have demonstrated mitochondrial accumulation at the level of the optic nerve head in experimental glaucoma, which could indicate that mechanical choking of axoplasmic flow occurs at the optic nerve head.[19], [20] More recently, it has been shown in a number of animal models that axonal transport is disrupted at the level of the optic nerve head, more specifically at the lamina cribrosa.[19], [21]–[23]

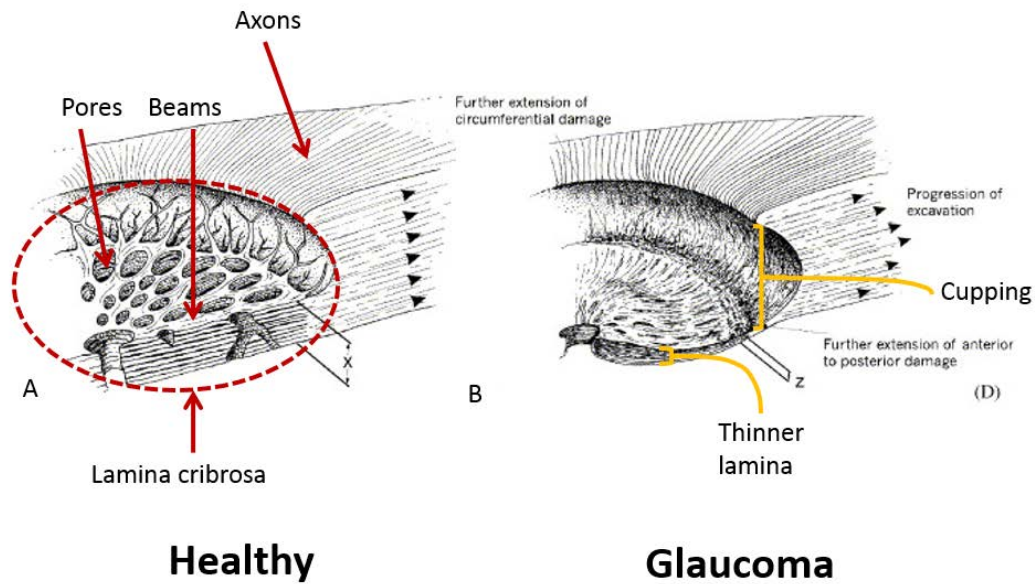


Figure 2. Characterization of the connective tissue changes of the optic nerve head and lamina cribrosa with glaucoma. (A) A healthy optic nerve head, with the lamina cribrosa beams and pores. Note the detailed microstructure of the lamina cribrosa. (B) Glaucoma damage results in thinning, excavation and posterior insertion of the lamina cribrosa. Adapted from Quigley et al. [24]

The lamina cribrosa (LC) was first described by Wilcek et al [25] in 1947 and has been studied extensively using histology due to its role in glaucoma. Quigley et al. had published a number of studies in 1980s forming the basis of our understanding of how the LC is altered by glaucoma (Figure 2). [24], [26], [27] Histology showed that eyes with glaucoma tend to have a characteristic cupping and excavation of the optic nerve head and LC. Furthermore, damage from glaucoma resulted in thinning of the LC. More recent studies of primate experimental glaucoma demonstrate that there is enlargement of the LC connective tissue, perhaps due to remodeling,[28] as well as posterior movement of the LC due to disinsertion, recruitment or migration.[29] Furthermore, biological studies suggest that astrocytes may play an important role in remodeling of the LC extracellular matrix as a result of the initial insult caused by elevated

intraocular pressure.[30] All these findings indicate that the LC is a complex structure undergoing dynamic changes in response to IOP related insults. Therefore, a full characterization of the LC microstructure changes is critical in understanding its relationship to the glaucomatous process.

1.3 THE ROLE OF INTRAOCULAR PRESSURE AND INTRACRANIAL PRESSURE

As alluded to earlier, the definition of glaucoma has undergone a tremendous change since it was first described.[6] Elevated intraocular pressure (IOP) is no longer an integral part of the definition of glaucoma due to considerable variability in pressure at which any given individual will develop clinically significant symptoms or signs of the disease.[8] Many patients develop typical glaucoma despite having IOP within population-derived normal ranges (also known as normal tension glaucoma) of 10mmHg – 21 mmHg[31] while others have elevated IOP without evidence of optic nerve damage during their lifetime (ocular hypertension).[32] Ocular hypertension is more prevalent than primary open angle glaucoma, and a third of people with primary chronic glaucoma have normal tension glaucoma.[33], [34] In fact, epidemiologic studies indicate that the vast majority of open angle glaucoma patients in Asian countries such as Japan[35] and China[36] have normal tension glaucoma.

Despite such variability in disease susceptibility, intraocular pressure still plays a critical role in the diagnosis and management of glaucoma. High intraocular pressure is predictive for both development[37] and progression of disease.[38], [39] Furthermore, those with normal tension glaucoma still benefit from additional pressure reduction, even though their IOP is within

normal range.[40] Despite these factors, intraocular pressure is the only modifiable risk factors in glaucoma.[41] Medical as well as surgical management of the disease primarily involve lowering IOP by decreasing aqueous humor production or increasing aqueous humor outflow.[42]

Considerable variation in the IOP at which an individual develops disease has led for a search for other variables that may influence the disease process. [43] Studies have looked to identify biological, vascular as well as biomechanical factors affecting one's susceptibility to disease.[17] All these factors could contribute to the wide variation in the pressure at which retinal ganglion cells undergo apoptosis which resulting in glaucoma. Recent studies have demonstrated that intracranial pressure (ICP), which acts posterior to the LC, may play a crucial role in the disease process (Figure 3). [44], [45] Berdahl et al reported that the intracranial pressures of eyes with glaucoma were significantly lower compared to those of healthy eyes.[44] The same study also showed that ICP was elevated in patients with ocular hypertension. As such, a number of authors have hypothesized that the translaminar pressure difference, which is the difference between IOP and ICP, may play an important role in determining whether one will develop glaucoma.[46], [47]

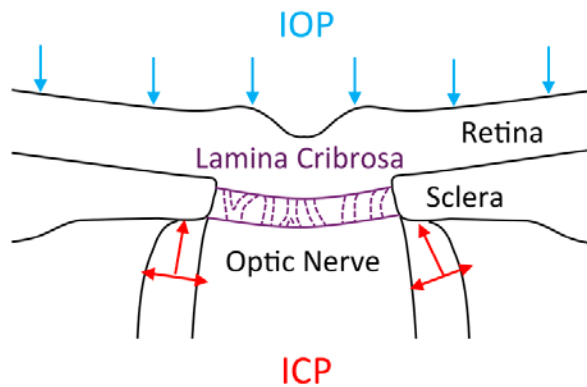


Figure 3. Diagram of the optic nerve head demonstrating the location at which intraocular pressure (IOP – light blue) and intracranial pressure (ICP – red) acts on the lamina cribrosa. While IOP acts anteriorly to the optic nerve head, the ICP acts posteriorly and circumferentially.

Findings from studies investigating the relationship between ICP and glaucoma demonstrated that high ICP may have a protective effect against glaucoma damage, potentially by modulating the translaminar pressure difference across the LC. [44], [48], [49] For example, in normal tension glaucoma patients with normal IOP, low ICP can cause the translaminar pressure difference to remain elevated, making those eyes prone to glaucoma damage. On the other hand, in cases of ocular hypertensive patients, the translaminar pressure difference remains normal because their high IOP is counterbalanced by their high ICP. Prospective human studies have shown that the translaminar pressure difference is elevated in patients with normal tension glaucoma as well as primary open angle glaucoma. [48]

Controlled modulation of the ICP is mainly accomplished through invasive procedures and therefore all experimental setups to alter ICP are performed in animal models. Studies have indicated a close correlation between ICP and the pressure in the posterior nerve. [47] Morgan et al show that the optic nerve head moves in accordance to the gradient between intraocular and

intracranial pressures, acting to oppose one another.[50] However, the Morgan et al study only assess the surface of the optic nerve head, without any consideration for how the LC or LC microstructure are affected. Furthermore, in a primate model with fixed IOP, extended ICP decrease is shown to result in glaucoma-like structural damage in half of the subjects.[51] However, these animal studies did not assess the effects of IOP or ICP on LC microstructure. Furthermore, the translaminar pressure difference (TLPD) may oversimplify the biomechanics of the local environment. As can be seen in Figure 3, IOP and ICP act in different regions of the LC. Therefore, further investigation is required to assess whether they truly cancel each other out. The interaction between IOP and ICP are likely complex and require further investigation. A systematic characterization of acute in vivo responses of the LC to changes in IOP and ICP is necessary to understand how these pressure changes may be a potential cause for axonal disruption.

1.4 OPTICAL COHERENCE TOMOGRAPHY

In vivo imaging of how the LC changes in different conditions is now possible using optical coherence tomography (OCT). OCT was a culmination of early work based on optical coherence-domain reflectometry, which was initially proposed as a one-dimensional ranging technique. [52]–[54] OCT was first described in the seminal Science paper by Huang et al in 1991,[55] which built on the early work on one-dimensional ranging by moving the scanning head to build a 2D image now commonly referred to as a B-scan.

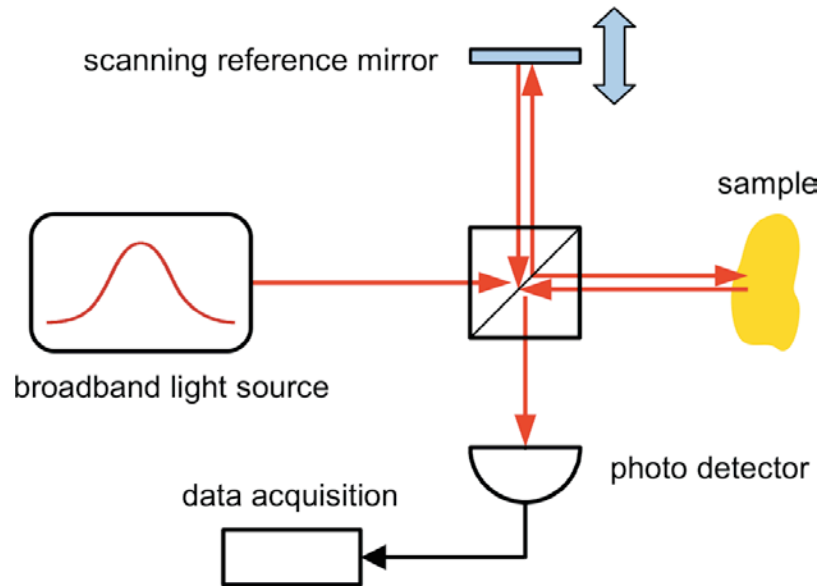


Figure 4. Diagram of time-domain OCT device. Adapted from Marschall et al. [56]

In early versions of OCT, commonly referred to as time-domain OCT, depth was encoded by translation of the reference mirror in time (Figure 4).[57] This greatly limited scanning speed to around 400Hz as each individual A-scan required moving the scanning reference mirror through the entire depth of the sample before moving the A-scan position. This limited the acquisition of 3D images in vivo due to motion artifacts in longer scans.[58] Imaging speed was drastically improved later on using spectral domain OCT, which allowed the time delay to be encoded as a spectrum, thereby eliminating the need for the moving reference mirror (Figure 6).[59] Over time, there has been drastic increases in both the scanning speed as well as resolution of OCT devices since they were first described.[57] Commercial spectral domain OCT devices for human imaging have scan rate between 27kHz (Cirrus HD-OCT, Zeiss) to 40kHz (Spectralis OCT, Heidelberg Engineering). The increase in scan speed allows the acquisition of 3D scan volumes now being the norm. 3D acquisition is done by putting together a series of adjacent B-scans (Figure 5).

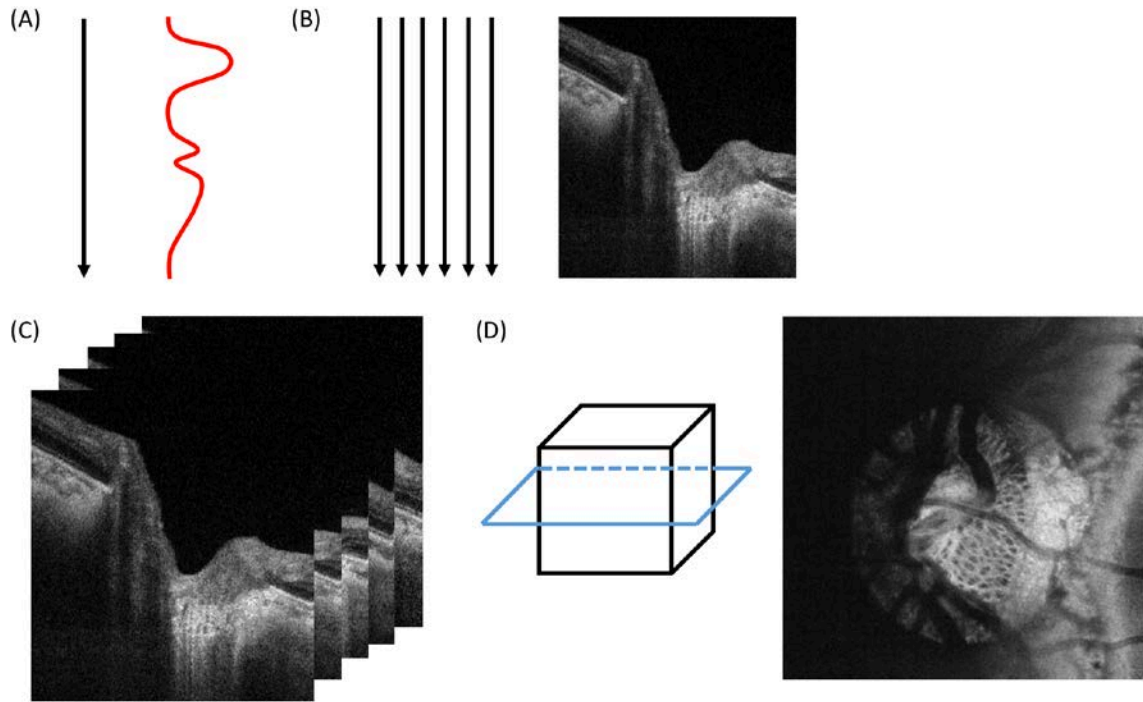


Figure 5. Description of the scan patterns used in this study. (A) A-scans are an individual scan down the depth of the tissue, red line indicate a graphical representation of the reflectivity along an individual A-scan. (B) B-scans represent a linear collection of adjacent A-scans and is typically used for cross-sectional visualization of tissue. (C) A 3D volume is generated by putting together a series of consecutive B-scans. (D) A C-mode or en-face image, is generated by reslicing the volume at a given plane (blue rectangle).

A key feature of OCT is its high axial and lateral resolution, permitting detailed 3D characterization of tissue structure. Lateral resolution is limited by the numerical aperture of the scanning device, as well as aberrations within the scanning media for posterior pole imaging. Numerical aperture of OCT devices is typically lower than conventional microscopy, due to the need for imaging across a larger scan depth. The lateral resolution of OCT is limited to around $15\mu\text{m}$, which is worse than the theoretical diffraction-limited resolution (around $3\mu\text{m}$) due to aberrations within the scanning media and air. This limitation can be overcome using adaptive optics [60], [61], which improves the lateral resolution to approximately $5\mu\text{m}$. The axial

resolution of OCT system is more easily controlled and is described in Equation 1. Since the device is an interferometer, it is dependent on both the bandwidth of the light source as well as the central wavelength. The choice of central wavelength in OCT imaging is limited to those that minimize water absorption and penetrate well into the eye. For conventional posterior pole imaging, this means selecting central wavelengths around 830-840nm, as well as 1 μ m. However, axial resolution can be increased using a broadband light source, or a combination of multiple light sources.

$$\delta_z = \frac{2 \ln(2)}{\pi} \frac{\lambda_c^2}{\Delta\lambda}$$

Equation 1: Theoretical axial resolution of OCT system. Axial resolution, δ_z ; Center wavelength, λ_c ;

Bandwidth, $\Delta\lambda$.

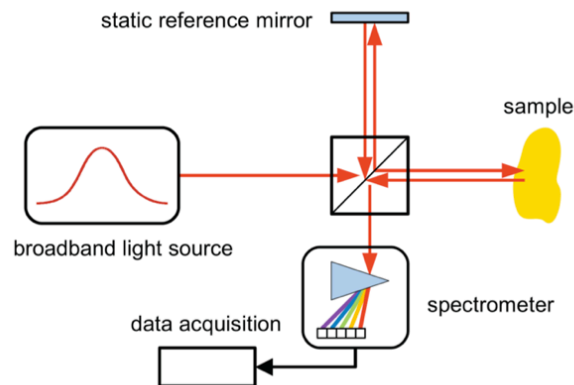


Figure 6. Diagram of spectral-domain OCT. Adapted from Marschall et al. [56]

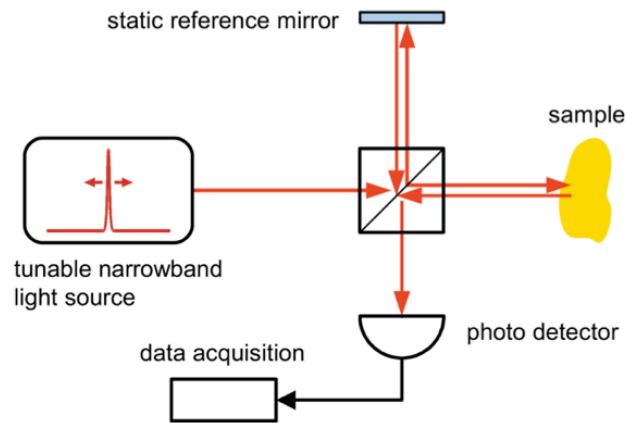


Figure 7. Diagram of swept source OCT system. Adapted from Marschall et al. [56]

Another iteration of the OCT technology used in this project is the swept source (SS-) OCT. Swept source OCT (Figure 7) is very similar in concept to spectral domain OCT (Figure 6). In both cases, depth is encoded by the Fourier transform of the spectrometer reading. However, unlike spectral domain OCT, which uses a broad-band light source, swept source OCT uses a swept wavelength tunable laser to target all the individual frequencies. This allows the device to reduce the signal roll-off with depth present in spectral domain OCT devices, improving the ability to acquire high quality images from deep structures of the eye. [62] This has the advantage of significantly increasing coherence length, imaging speed, and signal to noise. Despite being described in the late 1990s by Chinn et al,[63] SS-OCT was not readily available due to lack of fast, high quality and low cost swept laser sources until recently.[57] The presence of swept source has once again dramatically increased the scanning speed. Commercial machines scanning at 100kHz A-scans are now available and experimental systems have reached scan speeds of up to 1MHz.[64], [65]

1.5 IN VIVO ASSESSMENT OF THE LAMINA CRIBROSA

With new developments in OCT technology, many research groups have recognized the capability for OCT to assess the lamina cribrosa. Imaging of the detailed LC microstructure was first demonstrated using spectral domain OCT by Kagemann et al in 2008.[66] Since then, numerous studies have appeared in the literature describing the LC and how it changes with disease.[67]–[69] Several studies demonstrated an overall LC thinning with glaucoma corresponding with earlier histology studies.[24], [67] Furthermore, a few studies have demonstrated the presence of LC defects corresponding to the location of vision loss in the optic nerve.[70]–[72]

One area of deficit in the current field of studying the lamina cribrosa is the lack of microstructure analysis. Much of the work is limited to analyzing macroscopic features such as local surface defects in the anterior LC[72] and total LC thickness[67], without regards to the complex collagenous meshwork that makes up the LC (Figure 4, Figure 8). Without analysis of LC microstructure, a crucial information is missing considering that the retinal ganglion cell axons have to go through the pores within the lamina for the entire thickness of the lamina in their way to the brain. Localized axonal damage may occur in isolated regions of the LC, causing focal blockage of axoplasmic flow and ganglion cell damage which would be missed if only macroscopic analysis was performed. Furthermore, because IOP and ICP are affecting the optic nerve from different directions (Figure 3), the anterior LC may react to stress differently than the posterior LC. Therefore, a method to analyze the full 3D LC microstructure would improve our understanding of glaucoma pathogenesis, provide a novel diagnostic tool for glaucoma and new direction for treatment option.

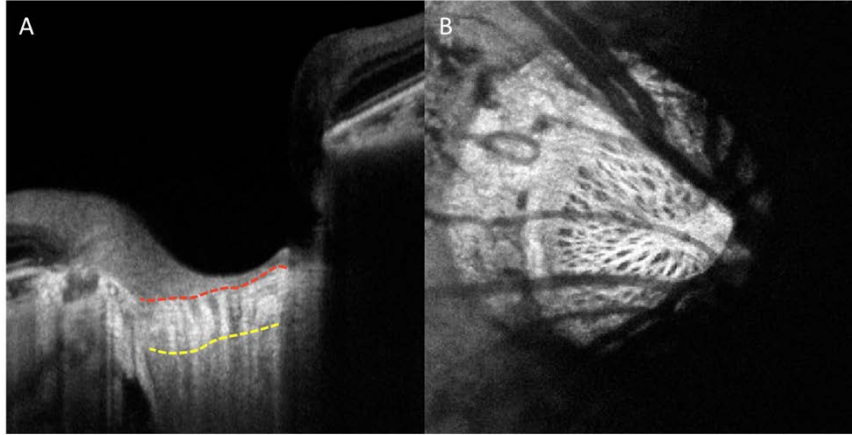


Figure 8. (A) Sagittal sections showing LC anterior surface (red dashed line) and posterior LC surface (yellow dashed line). Current in vivo studies involve manually analyzing these sections for macrostructural features such as total thickness. (B) Coronal sections showing LC microstructure.

OCT offers a number of advantages and disadvantages in assessment of the LC compared to other imaging modalities. Conventional whole body imaging devices, such as computed tomography (CT) and magnetic resonance imaging (MRI), do not have adequate resolution to resolve the fine structure of the LC. Even the state-of-the-art experimental devices, using high magnetic fields and large amounts of ionizing radiation are still almost an order of magnitude worse in resolution. However, both MRI and CT offers the advantage of high tissue penetration, allowing the assessment of the entire optic nerve region, including the posterior sections often not visible on OCT. Even high frequency ultrasound designed for the eye [73] suffer from depth of penetration problems in the posterior eye. Thus, OCT represents the best tool for in vivo assessment of the LC.

1.6 PROJECT AIMS

The aim of this project is to use OCT to perform the first detailed in vivo assessment of the LC microstructure. The overall hypothesis of this thesis is that OCT can be used to assess LC microstructure which will provide critical information for glaucoma diagnosis and pathogenesis. In order to test this hypothesis, the project was separated into three Aims, as outlined below.

1.6.1 Aim 1: To develop and evaluate a semi-automated method of segmentation and analysis of LC microstructure

Due to the complexity of LC microstructure, current work on the LC primarily involves manual segmentation of LC macrostructure. [67] Since manual segmentation of the 3D LC microstructure is prone to measurement variability related to the subjective delineation as well as being time-consuming and clinically infeasible, we aim to develop and validate a method to semi-automated and robust method for segmentation and quantification of the LC microstructure.

1.6.2 Aim 2: To evaluate the effects of acute modulation of both intraocular and intracranial pressure on the primate LC

Numerous studies have suggested that ICP may modulate the effect of IOP in the optic nerve. However, the mechanical deformations resulting in this effect is not currently known. Understanding how these pressures can influence glaucomatous damage requires a systematic characterization of the acute response of the LC microstructure to changing IOP and ICP. We

will utilize the tools developed in Aim 1 to assess how LC microstructure deforms in vivo due to pressure.

1.6.3 Aim 3: To characterize the effects of glaucoma on the human LC

In Aim 3, we will take the knowledge gained from animal studies in Aim 2 to improve our assessment of human glaucoma. Histological studies have shown changes in LC microstructure in glaucoma, but post-mortem tissue changes raise concerns about the applicability of the findings in living eyes.[24], [26] We will characterize in vivo the 3D structure of healthy human LC and then compare it with glaucoma eyes. Furthermore, we will determine the association between LC microstructure features with disease severity.

Taken together this project will provide innovative information crucial for understanding the role of the LC as the primary target of the glaucomatous process.

2.0 RECRUITMENT OF HUMAN SUBJECTS

We enrolled healthy, glaucoma-suspect and glaucoma subjects from the UPMC Eye Center (Pittsburgh, PA). All studies were conducted in accordance with the tenets of the Declaration of Helsinki [74] and the Health Insurance Portability and Accountability Act. The institutional review board of the University of Pittsburgh approved these studies, and all subjects gave a written consent prior to participation. Healthy eyes were defined as those with normal appearance of the optic nerve head and retinal nerve fiber layer, IOP <21mmHg, full visual fields, and no other ocular pathologies. Glaucoma suspects eyes had abnormal appearing optic nerve, asymmetrical optic nerve cupping, or IOP>21mmHg, all accompanied by normal VF test results. The non-symptomatic eye of unilateral glaucoma patients were also considered as glaucoma suspect. Glaucomatous eyes had characteristic optic nerve head cupping, retinal nerve fiber layer defect, and reproducible glaucomatous visual field defect.

2.1 INCLUSION CRITERIA

All men and women aged 18 and older that meeting the above criteria were and included in the study.

2.2 EXCLUSION CRITERIA

Exclusion criteria for the study included subjects with 1) non-glaucomatous ocular diseases, 2) neurologic and non-glaucomatous causes for visual field damage, and 3) intraocular surgery other than non-complicated cataract or glaucoma surgery. Subjects with refractive error greater than ± 6.00 Diopters and cylinder power > 3.00 Diopters. These exclusion criteria were used to limit the effect of potential confounders on structural imaging.

2.3 TESTING PROTOCOL

All subjects underwent a comprehensive ophthalmic evaluation, including intraocular pressure (IOP), VF testing, commercial spectral domain-OCT (Cirrus HD-OCT), and swept source-OCT imaging of the LC, all acquired within 6-month window.

IOP measurement was performed using Goldmann applanation tonometry, which is widely considered to be the gold standard in IOP measurement. Goldmann applanation tonometry is based on the Imbert Frick principle, which dictates that the pressure inside a perfectly elastic sphere is equal to the force applied divided by the area of flattening.

VF testing was performed using standard achromatic perimetry, 24-2 Swedish interactive threshold algorithm standard (Humphrey Field Analyzer; Zeiss, Dublin, CA). VF testing with greater than 30% fixation loss, false-positive or false negative responses were excluded from the study.

3.0 DESCRIPTION OF DEVICES

The following section describes the tools used in this study to assess the eye.

3.1 OPTICAL COHERENCE TOMOGRAPHY

3.1.1 Spectral Domain Optical Coherence Tomography

3.1.1.1 Bioptigen SD-OCT

A commercial SD-OCT, the Bioptigen SD-OCT (Bioptigen, Research Triangle, NC) was used for all our animal studies. The device uses the commercial patient scanner and optics engine coupled a modified light source with a broadband superluminescent diode (Superlum, Dublin, Ireland; $\lambda=870$ nm, $\Delta\lambda=200$ nm). This achieved an estimated axial resolution of $2\mu\text{m}$ (limited by the spectrometer, as the theoretical limit is $1.6\mu\text{m}$) and a $15\mu\text{m}$ transverse resolution. The device offers significantly higher axial resolution compared standard commercial devices, due to its very high bandwidth light source. Furthermore, Bioptigen SD-OCT allows full control of all scanning parameters, including scan size, sampling density and scan type, which is typically not available on human scanners. The device was demonstrated to be capable of imaging the human LC microstructure in early studies by Kagemann et al. [66]

3.1.1.2 Cirrus HD-OCT

A commercial SD-OCT, Cirrus HD-OCT (Zeiss, Dublin, CA), was used for standard assessment of retinal nerve fiber layer thickness. It features an 840 nm center wavelength, achieving an estimated axial resolution of 5 μ m and 15 μ m transverse resolution. The device has a scan rate of 27,000Hz. Despite a number of other potential SD-OCT devices to choose from, the Cirrus was chosen due to its wide use in clinical ophthalmology, well characterized parameters [75], [76] and throughout isotropic 3D sampling of optic nerve head.

All subjects were scanned a 6.0 mm x 6.0 mm x 2.0 mm (200 x 200 x 1024 samplings) region centered on the optic nerve head. The quality of the SD-OCT images were judged subjectively by evaluating the OCT fundus images for eye movements and missing areas. OCT data with signal strength below 7 (manufacturer's recommended cutoff) were excluded. The automated segmentation routine from the manufacturer was used to measure the retinal nerve fiber layer thickness in a 3.4 mm-diameter circle centered around the optic nerve head. [58]

ONH and RNFL OU Analysis: Optic Disc Cube 200x200 OD ● | ● OS

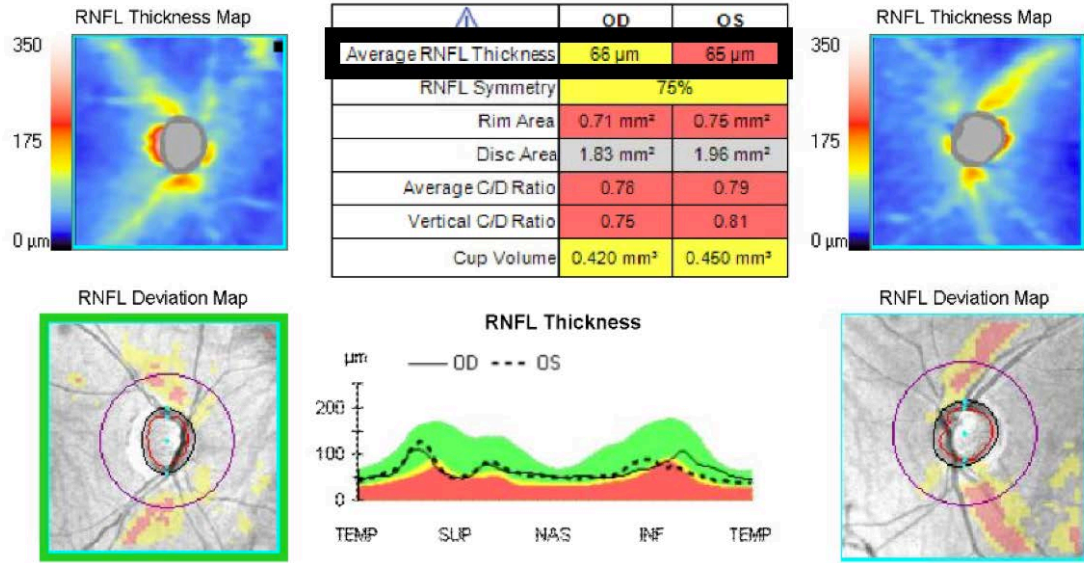


Figure 9. Commercial spectral domain OCT scan of the optic nerve by Cirrus HD-OCT. The analysis shows thinning of the retinal nerve fiber layer in both the right and left eye, slightly more prominent in the left. The summary measurement used was average retinal nerve fiber layer thickness (black box).

3.1.2 Swept Source Optical Coherence Tomography

The swept source-OCT device used in this study is a prototype device manufactured by our collaborators at the Massachusetts Institute of Technology (Cambridge, MA). The device features 100 kHz scan rate and a light source centered at 1050 nm, resulting in a 5 μm axial resolution and a 20 μm lateral resolution. The device is described in greater detail in a previous publication by Grulkowski et al [77].

All eyes were scanned in a 3.5 mm x 3.5 mm x 3.64 mm (400 x 400 x 896 samplings) volume centered on the LC and optic nerve head. This scan size was chosen to maximize our ability to capture both the LC and the surrounding optic nerve tissue. The focus depth of the

device was set at the level of the LC to maximize image quality within the area of interest. Two orthogonally oriented scan volume (horizontal and vertical orientation raster) were co-registered to remove motion artifacts.[78] This registration algorithm has been previously shown to remove minor motion artifacts and improve signal to noise ratio of the resulting co-registered scan.[78] Scans with large eye movements causing failure of the registration algorithm were excluded from the study, as were the scans without visible LC microstructure from which no useful data could be obtained.

3.2 VISUAL FIELD TESTING

Visual field testing is one of the primary method of assessing functional visual deficits in glaucoma. The most commonly used method of visual field testing is standard automated perimetry, with a white stimulus projected on a white background. The ability of the patient to identify stimulation of different regions of their visual field is used to create a visual map of locations where the subjects performed comparably to an age-adjusted average of healthy population. The most commonly used testing algorithm is the Swedish Interactive Threshold Algorithm (SITA), [79] which was developed to shorten the test and improve efficiency. While visual loss in glaucoma is complex, different visual field patterns often emerge. These findings can be summarized in visual field mean deviation (VF MD), reflecting the depression of the patient's threshold sensitivity compared to age-matched healthy subjects. Lower VF MD (more negative) indicates worse performance on the visual fields, and VF MD near 0 indicate normal visual fields.

4.0 DEVELOPMENT AND EVALUATION OF LAMINA CRIBROSA SEGMENTATION

High-speed OCT systems permit rapid acquisition of the LC in 3D, capturing the fine details of lamina cribrosa microstructure.[66], [80] Yet, in vivo LC analysis in current glaucoma research is still performed on single 2D cross-sectional scans using manual segmentation[67], [72], [81] due to the complexity of the LC microstructure. It is very important to create and test a semi-automated segmentation method that would capture the 3D microstructure of the LC. In order to be clinically viable, the algorithm needs to be fast and perform at a level similar to a manual observer, which is used as a gold standard. We hypothesize that a semi-automated segmentation algorithm of LC microstructure will have high sensitivity and specificity to delineate LC microstructure compared to manual delineation.

4.1 EXPERIMENT 1-1: TO CREATE A SEMI-AUTOMATED SEGMENTATION AND ANALYSIS METHOD OF THE LC MICROSTRUCTURE

Automated tools have played a critical role in the development of OCT technology and its rapid adoption into clinical and research in ophthalmology. Automated segmentation of the retina [82] and optic nerve head [83] are frequently done for assessment of both glaucoma as well as other ophthalmic pathologies. These segmentation tools helped clinicians to interpret the result and

played a large part in the commercial success of the machines. As such, in order for LC microstructure analysis to have potential clinical relevance, the first step is to develop an automated segmentation and analysis method of LC microstructure. Furthermore, automated segmentation would allow quantification of a complex structure that is otherwise extremely difficult to assess. The hypothesis of this experiment is that an automated segmentation algorithm will segment the LC microstructure with high sensitivity and specificity.

4.1.1 Methods

OCT images of the LC were typically noisy and featured an uneven background (Figure 10). There were significant variations in image intensity, ranging from dark shadows behind blood vessels to highest reflectivity pixels in the center of the optic nerve where the prelaminar tissue is thinnest and only a few blood vessels to block the OCT light. Thus, it was not possible to use a global threshold for segmentations due to the variations in intensity. With this in mind, the following describes the steps used in the developed segmentation algorithm:

Step 1: Image was smoothed using 3D Gaussian filter with a 3 pixel σ_z and a 1 pixel $\sigma_{x,y}$ to reduce high frequency noise (Figure 10). OCT is partly degraded by the presence of speckle noise, caused by the limited bandwidth of the interference signal.[84] While speckle noise is similar to salt and pepper noise, which is most optimally removed by median filtering,[85] we chose to use Gaussian filters due to their simplicity and speed.

Step 2: Contrast limited adaptive histogram equalization was performed to enhance the image quality. [86] The parameters include: 1) Block size – the local region over which the histogram equalization is applied and 2) Slope – degree of contrast stretching over the block size.

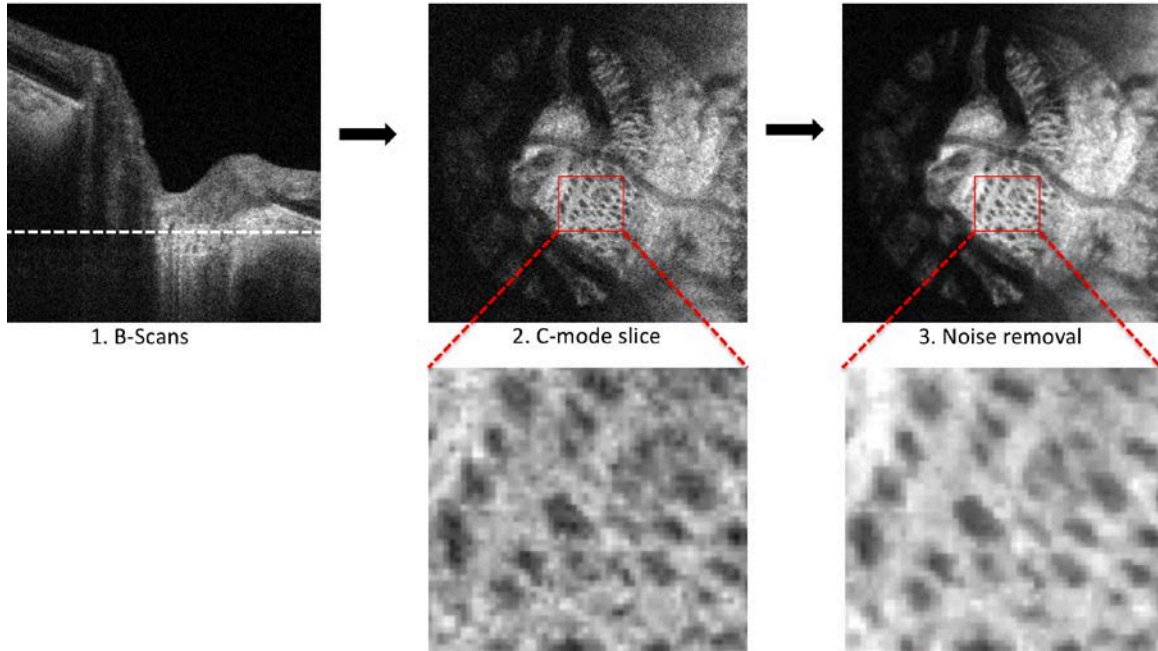


Figure 10. Initialization of the images. (1) The series of B-scans are first resliced (white dashed line) to look at (2) a series of C-mode slices. (3) A Gaussian filter is applied to remove image noise.

Step 3: An automated local thresholding technique developed by Niblack [87] was used to binarize the image, differentiating pores in the C-mode slice from the surrounding LC structure (Fig. 2.3). The local thresholding algorithm follows the equation below. As seen in this equation, there were significant complexities within the different parameters. We performed a thorough analysis of all parameters and compared them to the gold standard manual delineations. The top performing parameters were then selected and compared subjectively to ultimately select the top performing parameter.

$$I_{\text{segmented}} = \begin{cases} \text{Background,} & \text{If } I_{\text{original}} > \mu + k\sigma + c; \\ \text{else, object} & \end{cases}$$

Equation 2: Niblack local thresholding. Block size – the region over which local thresholding is applied. I – Pixel intensity at current pixel. μ – Mean pixel intensity in the block centered on the current pixel. σ – The standard deviation within the local block. k – Pixel intensity standard deviation

Step 4: A 3D median filter was passed over the segmented volume with $1 \times 1 \times 3$ kernel size (Fig. 2.4). The z filtering removed segmented pixels due to intensity drops in a single C-mode. This allowed the automated algorithm to account for 3D continuity.

Step 5: A manually defined mask was applied to the region peripheral to the LC, restricting the segmented components to those within the region of interest (Fig. 2.4). Full processing took approximately 1 second per image.

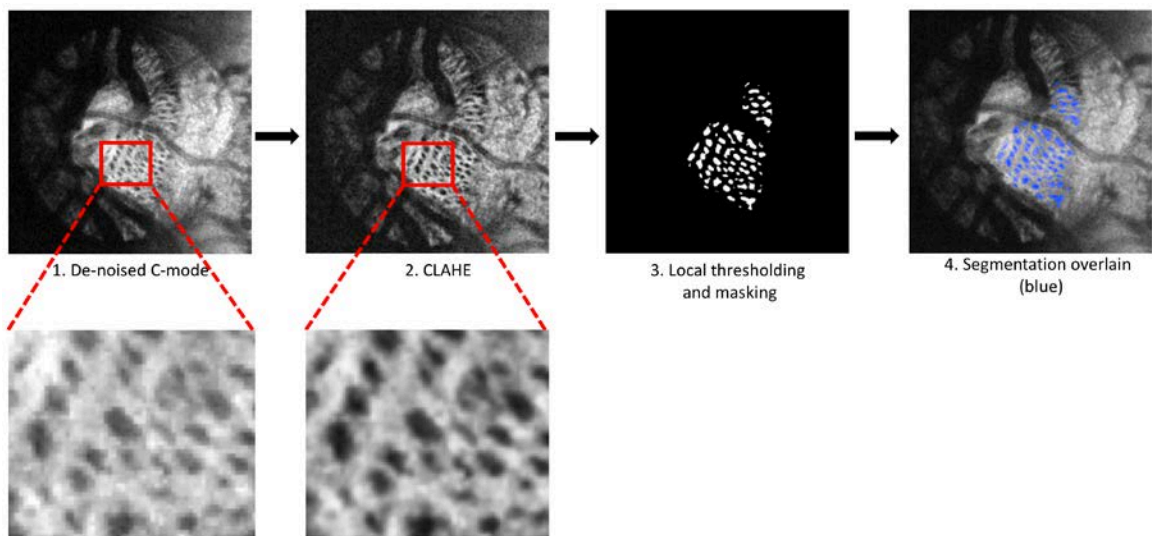


Figure 11. Automated segmentation of the LC microstructure. After (1) de-noising the image, the entire stack underwent contrast limited adaptive histogram equalization (CLAHE) and (3) local thresholding and masking to identify the pores. (4) Segmentations of the pores were overlaid on top of the original image.

Segmentation was also manually performed by two experienced observers masked to one another, clinical information, and the outcome of automated segmentation. While the segmentation works in 3D, a single frame was chosen per eye due to the time consuming nature of delineating all pores in a 3D stack. Frames for manual segmentations underwent the same smoothing and local contrast enhancement as those performed for the automated segmentation to ensure comparable conditions for analysis. After such preprocessing, the human observers manually demarcated regions of the image that appeared to be pores using the TrakEM2 feature of the ImageJ image analysis software.[88] When necessary, adjacent C-mode slices were consulted to discriminate pores from noise, by observing the continuity of local regions of low pixel intensity through the stack. The same peripheral mask used in the automated segmentation was applied to the manual segmentations. Manual delineation took on average approximately 18 minutes per image, which equated to nearly 6 hours for a single volume scan.

The pore segmentation was compared between the automated and manual methods, first qualitatively and then quantitatively by calculating sensitivity and specificity using pixels classified as pores on a per-pixel basis. The gold standard pore segmentations were taken as the pixels both observers agreed upon within the boundary of a pore. In addition, the following parameters were measured using ImageJ, and then compared using a measurement error model: pore number, average pore area, average pore aspect ratio, average pore thickness, and average beam thickness. Pore area and aspect ratio were calculated by considering each segmented pore as a particle and averaging over all particles in the frame. Aspect ratio refers to the ratio of the major axis to minor axis of an ellipse fitted to each pore. Beam thickness is taken as the average thickness of the region inverse to the pores within the boundaries of the LC surface, while pore thickness is a radial thickness measurement of segmented pores. Thicknesses were computed by

expanding circles from each point within the segmented region until the boundary was first reached. Each point was assigned a value corresponding to the radius of the largest circle containing that point, from which a global mean ‘thickness’ could be calculated.[89], [90] The connective tissue volume fraction (CTVF) is a ratio of the segmented laminar beams to total LC area within a slice.

The measurement error model estimated the latent “true” value for each parameter within a subject and calculated the bias (systematic error) and imprecision (random error) component for each observer and the automated technique based on the set of values within the population. In order to allow for comparison between imprecisions, the computed values were adjusted for the scale bias. R Language and Environment for Statistical Computing program, was used for the statistical analysis (version 2.15.1; R Foundation for Statistical Computing, Vienna, Austria; <http://www.R-project.org>)[91]–[93].

4.1.2 Results

The study included 14 healthy and 16 glaucoma subjects with an average age of 55.2 ± 18.6 years, and an average visual field mean deviation (MD) of -6.39 ± 5.95 dB amongst glaucoma subjects.

Subjective evaluation of the automated segmentation method determined that there were no pores that were obviously misclassified (Figure 12). Subjective comparison of pore segmentation showed strong agreement between segmentation methods in regions of the lamina with good signal strength. Segments of the image with poorer signal corresponded with the regions of disparity between the segmentation methods (Figure 12). However, there appeared to be as much disagreement between observers as there was between an observer and automated segmentation.

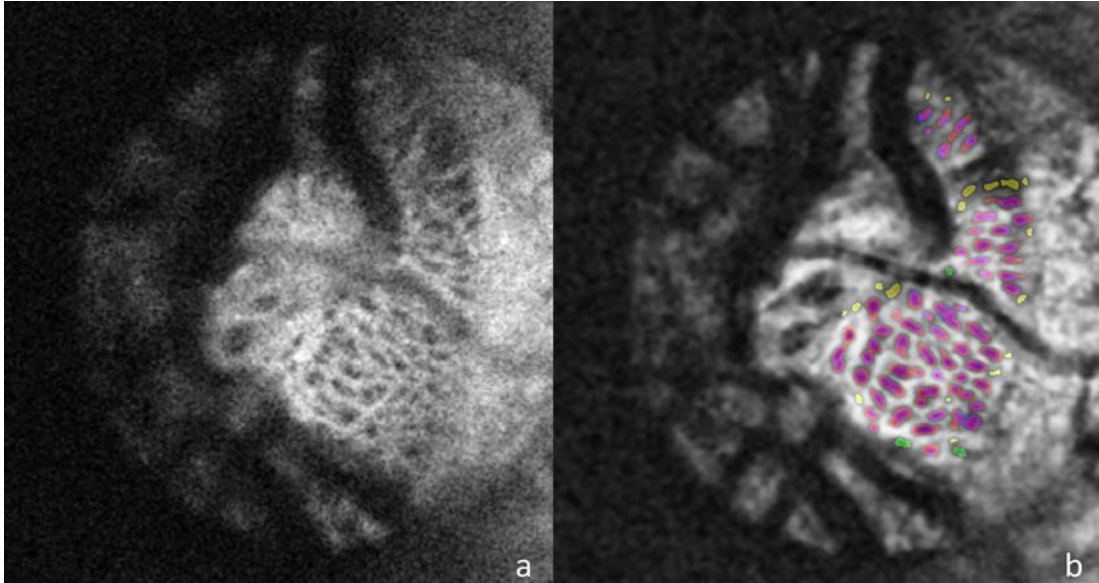


Figure 12. The unprocessed C-mode slice (a) and corresponding segmentation (b) for a scan of a healthy eye taken with the SS-OCT device. For pores identified by both automated and manual segmentations, the automated pores are colored red and the manual ones are colored blue, so that overlapping segmentation appears as purple. Pores identified only by the automated method are colored yellow and those seen solely in the manual segmentation are colored green. Pores detected only by manual segmentation were mostly located adjacent to blood vessel shadow margins.

Using manual segmentation as gold standard, average sensitivity and specificity of the automated segmentation was 82.3% and 91.0%. The inter-observer agreement constituted 85.5% of segmented pixels. Table 1 summarizes the measurements values, as well as the imprecision for the two graders and the automated segmentation. The estimated imprecisions, once the scale bias of the parameters are accounted for, are similar when comparing between manual segmentations and when comparing between manual and automated segmentations. Due to the small number of observations, there were no difference in the imprecisions between manual and automated methods, and confidence intervals on imprecision values could not be reliably

established. None of the parameter averages or imprecision values showed statistically significant differences between the manual and automated methods.

Table 1. Average measurement and imprecision estimate for each segmentation method using SS-OCT. Obs – Observer. CTVF – Connective Tissue Volume Fraction.

Parameter	Average			Imprecision		
	Auto	Obs. 1	Obs. 2	Auto	Obs. 1	Obs. 2
Pore number	99.7	94.1	87.8	19.04	20.40	21.59
Pore area (pixels ²)	201.2	211.4	268.9	42.0	29.3	42.9
Pore aspect ratio	2.05	1.77	1.71	0.096	0.118	0.100
Pore Thickness (pixels)	11.19	12.81	15.36	0.61	0.45	0.00
Beam Thickness (pixels)	20.29	22.53	22.62	1.51	0.54	0.53
CTVF	0.748	0.748	0.693	0.02	0.03	0.02

4.1.3 Discussion

In this experiment, we demonstrate an automated method of segmenting LC microstructure. When comparing to the gold standard manual segmentation, we find that the automated segmentation has excellent sensitivity and specificity. Furthermore, the imprecision of the automated segmentation is no different than that of the two manual observers.

The excellent and quick performance of the segmentation algorithm means that we will be able to perform automated analysis of LC microstructure in future experiments. This is significantly faster than the manual methods, enabling the technology to be clinically useful for assessing LC microstructure.

The automated LC segmentation analysis we propose includes multiple steps. A local contrast enhancement is chosen because the average image intensity varied through individual B-scans in the 3D volume. However, our primary interest is in quantifying pores, which have local drops in intensity. The local enhancement provides better pixel-scale contrast that aids visualization of pore edges without substantially changing the appearance of global features. The Gaussian filter adequately removes noise, improving the overall image quality. The 3D median filter with a large Z radius discriminates local intensity drops in isolated C-mode slices from those present in multiple sequential slices and more likely to be classified as pores by a human observer. Taken together, the performance of the automated segmentation is subjectively judged to adequately delineate the LC microstructure using swept source OCT.

The disagreement between observers for manual segmentation reveals the difficulty with subjective assessment as a gold standard for LC segmentation (Figure 12, Table 1). Nevertheless, acceptable sensitivity and specificity of the automated method is noted. The automated analysis tends to provide lower pore thickness values and an overall more elliptical shape of the pores (higher aspect ratio) than manual segmentations. Such finding may be a result of our human observer's intrinsic expectation of pores being small round objects. The difference in aspect ratio may also be due to the automated method connecting adjacent pores separated by low contrast connective tissue, which human subjects are more capable of differentiating. This may also contribute to the relatively low pore thickness values, since connections tend to be thinner than the pores they connect. It may seem counterintuitive that pore thickness decreases as two pores are merged since pore area increases. However, if one considers an hourglass-shaped pore, each end will have greater thickness (as defined in the methods) than the connecting

bottleneck, and the overall mean thickness would be reduced by including this connection in calculating the average thickness.

Pore segmentations are filtered in the Z-direction to remove noise due to intensity drops in single slices. This may result in the merging or splitting of pores, which bifurcate and merge with depth as they pass through the LC. The depth position of a split or merge varies subjectively, and the decision of observers sometimes disagreed with the outcome of the automated method. Pore number, size, and aspect ratio are sensitive to the splitting and merging of pores, and to a lesser degree so are beam and pore thickness. Ratio measurements provide a macroscopic look at the fine structure without over-weighting pixels with indefinite classifications. Nevertheless, measurement imprecision or variability is similar for manual and automated analysis, with values within 4.0% of one another (compared to 3.7% between observers). When combined with the favorable outcome of subjective evaluation, the similarity in imprecision and lack of statistically significant difference in any of the parameters indicated that the automated method is an effective tool for LC segmentation.

A limitation of this study is the relatively small number of scans that were analyzed. The heavily labor-intensive and time-consuming nature of manually delineating numerous pores in each scan restricted the feasibility of a larger cohort. As a result, confidence intervals on imprecision values could not be reliably established. In fact, this limitation highlights the necessity of such an automated technique, particularly when used on a dense 3D volume routinely and rapidly acquired by OCT. Furthermore, the segmentation has poorer performance in regions of poor image quality, especially in the peripheral LC and near blood vessels. As such, these regions are typically excluded from analysis, unless small observable local drops in intensity are present.

In this experiment, the performance of the proposed segmentation algorithm was compared to manual segmentation in 2D images. Yet, it should be emphasized that this segmentation method is fully operational on 3D scans, providing a novel method for microstructural segmentation of 3D OCT scans of the LC. The method is also applicable to other imaging modalities (including some commercial devices) visualizing LC microstructure. However, differences in image size, contrast, and noise characteristics should be considered in order to attain good segmentation performance and tuning of the parameter will be required.

4.2 EXPERIMENT 1-2: TO ASSESS THE REPRODUCIBILITY OF A SEMI-AUTOMATED SEGMENTATION METHOD OF LC MICROSTRUCTURE

In the previous experiment, we described an automated method of segmenting and analyzing the 3D microstructure features of the LC from OCT imaging, which significantly reduced the time to analyze the LC.[94] In order for the segmentation algorithm to be of value for clinical and research use, it must be reproducible as well as fast and accurate. Because it is impossible to compare in vivo measurements acquired with OCT with ground truth physical measurements, assessing the reproducibility is the standard step in validating the efficacy of new segmentation algorithms.[76], [95], [96] Any tool with high inter-scan variability will make it difficult to assess change in a given subject and decrease its relevance. In this experiment, we assessed the reproducibility of the automated segmentation of in vivo LC 3D microstructure scanned using OCT that we developed in Experiment 1-1. We hypothesize that a semi-automated segmentation analysis will offer high measurement reproducibility.

4.2.1 Methods

A total of 49 eyes (8 healthy, 19 glaucoma suspect, 12 glaucoma) from 39 subjects representing the range of healthy and diseased eyes typically seen in glaucoma practice, were enrolled to the study. Disease status and clinical examination were performed as described in the Recruitment of Human Subjects section.

4.2.1.1 Image Acquisition and Processing with Swept Source-OCT

All subjects underwent 2 swept source-OCT scans of the optic nerve head. The two OCT scans were taken within approximately one minute of each other, with the focus and OCT machine readjusted after each scan. The scans were processed using ImageJ [97] segmentation tool (<http://rsbweb.nih.gov/ij/>), as previously described in Experiment 1-1. [94]

In order to examine the effect of scanning angle on LC microstructure measurements, a single OCT volume was rotated $\pm 10^\circ$ with respect to the slow scanning axis using ImageJ. [97]

4.2.1.2 Statistical Analysis

Reproducibility was assessed by determining the imprecision SD of repeated measurements using a measurement error model, accounting for the use of both eyes from some of the subjects. [92] The imprecision SD measures the typical size of the random error made by the device when a measurement is made, assuming a bias of 1 since the same method is used to analyze the repeated scans.[98] Relative imprecision was calculated by dividing the imprecision by the measurement's average. Low imprecision between two scans indicated high reproducibility. Statistical analysis was performed using R Language and Environment for Statistical Computing program (version 2.15.1). [91]

4.2.2 Results

Average age for all subjects was 57 ± 14 years with an average visual field mean deviation of -0.4 ± 0.9 dB for healthy ($n = 8$), -0.6 ± 1.3 dB for glaucoma suspects ($n = 19$), and -4.5 ± 7.5 dB for glaucoma subjects ($n = 12$). Automated segmentation of two different scans of the same eye is shown in Figure 13. Observable differences between automated segmentation of the two scans primarily occurred due to differences in region of the LC included in the analysis (Figure 14). Some of the differences could be explained by a small alteration in scan angle between images creating distortions in the region of LC within a plane (C-mode) and along a cross-section (B-scans) (Figure 15).

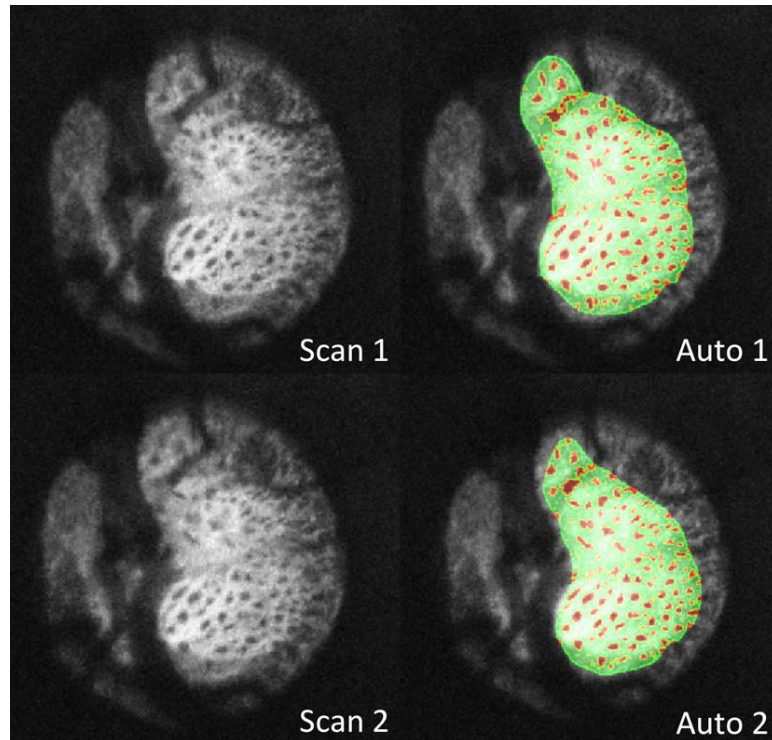


Figure 13. Two consecutive optical coherence tomography scans of the lamina cribrosa of the same eye. Original C-mode (left) and segmentation overlain (right) where beams (green) and pores (red) are marked. Differences in segmentations between the two scans primarily existed due to local disparities in regions analyzed.

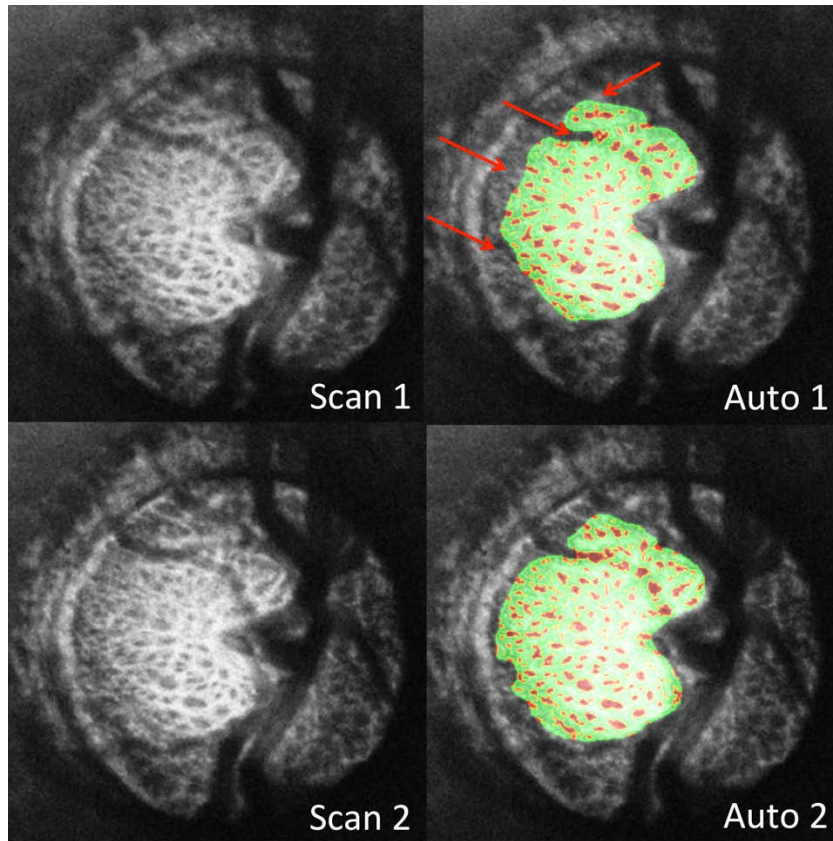


Figure 14. Two consecutive optical coherence tomography scans of the lamina cribrosa of the same eye. Original C-mode (left) and segmentation overlain (right) where beams (green) and pores (red) are marked. Differences in segmentations between the two scans (red arrows) primarily existed due to local disparities in regions analyzed.

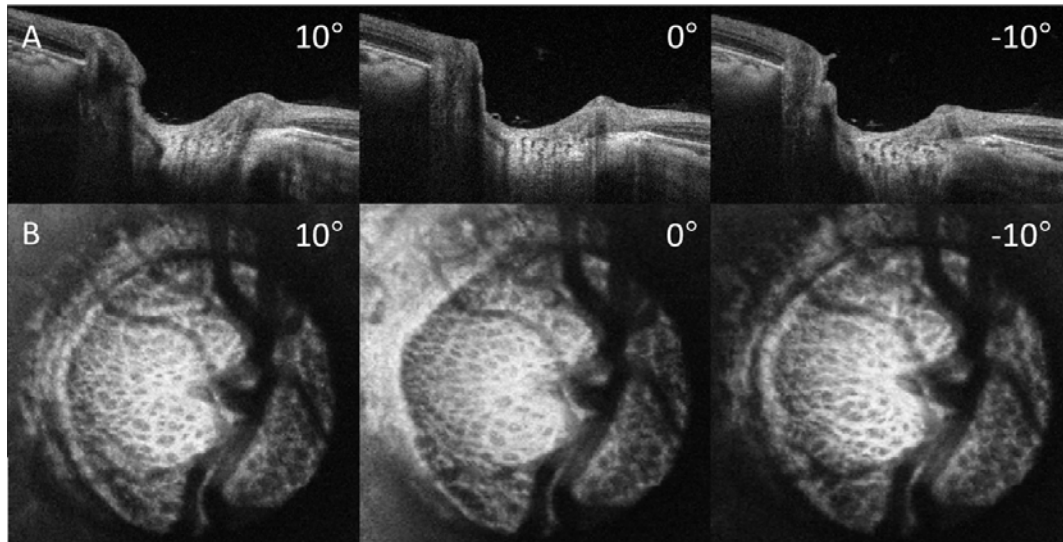


Figure 15. Shifts in the scanning angle alter B-scan (A) and C-mode (B) images and alter the microstructure seen on a single frame from the center of the volume. The scan angle changes were simulated using image processing software (ImageJ).

Despite these edge effects, 3D view of the visible LC appeared highly repeatable (Figure 16). The average number of C-mode slices over which pores were measured was 69 ± 13 slices per eye (range: 38 - 101). This corresponds to a physical depth of $281 \pm 54\mu\text{m}$.

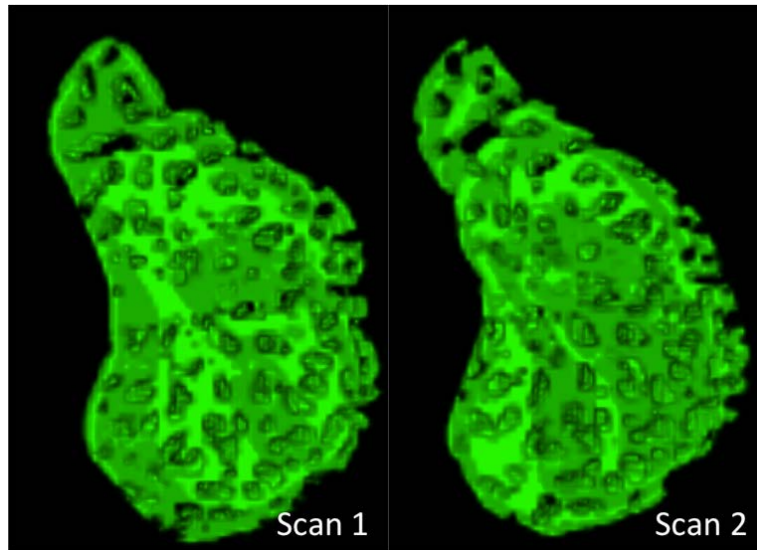


Figure 16. 3D view of lamina cribrosa beams demonstrated the similarity of the microstructural features (same eye as Figure 13).

The relative imprecision of all LC microstructural parameters using data from all eyes was ≤ 4.2 (Table 2). When comparing the relative imprecision between the diagnostic categories there was no significant difference with the exception of pore diameter, which was higher in healthy eyes compared to glaucoma eyes (Table 3).

Table 2. Average and imprecision for lamina cribrosa parameters.

Parameters	Average (SD)	Imprecision	Relative Imprecision (%)
Pore Diameter (μm)	24.2 (1.9)	0.4	1.8
Pore Diameter SD (μm)	9.8 (0.8)	0.2	2.0
Pore Aspect Ratio	2.00 (0.11)	0.04	1.8
Pore Area (μm^2)	1660 (206)	50	3.0
Beam Thickness (μm)	48.8 (2.7)	1.0	2.0
Beam Thickness SD (μm)	16.1 (1.7)	0.7	4.2
Beam Thickness to Pore Diameter Ratio	2.0 (0.1)	0.1	1.8

Table 3. Relative imprecision of lamina cribrosa parameters in relation to clinical diagnosis.

Parameters	Healthy (n = 8)	Glaucoma Suspect (n = 19)	Glaucoma (n = 12)
Pore Diameter (μm)	2.8%	1.5%	1.2%
Pore Diameter SD (μm)	2.7%	1.6%	2.2%
Pore Aspect Ratio	2.1%	1.7%	1.8%
Pore Area (μm^2)	3.0%	2.4%	4.2%
Beam Thickness (μm)	2.0%	2.2%	1.8%
Beam Thickness SD (μm)	4.7%	4.7%	2.7%
Beam Thickness to Pore Diameter Ratio	1.9%	1.9%	1.4%

4.2.3 Discussion

In this experiment, we demonstrated that an automated 3D LC segmentation analysis tool we developed in Experiment 1-1 provided highly reproducible information on the 3D LC microstructure in a cohort representing the typical mixture of subjects handled in glaucoma service. The relative imprecision of all parameters was no larger than 4.2%.

Conceptually, we expected that parameters generated by 3D analysis (beam thickness, pore diameter, and beam thickness to pore diameter ratio) would show better reproducibility than those generated by averaging across sequential C-mode slices (pore aspect ratio and pore area). Whereas averaging across all sequential C-mode slices does represent the entire visible LC, the measurement could vary due to small shifts in scan angle. For example, shadows due to blood vessels might cause pores to appear in one scan angle, but not another. Therefore, parameters highly dependent on the scanning angle, such as pore count, are not reliable in OCT studies of the LC. Nevertheless, we demonstrated that both 3D and averaging across sequential C-mode provide robust and reproducible measurements of the LC microstructure (Table 2).

Differences in regions of analyzed LC between two different C-mode scans were noted in some of the eyes (Figure 14). The analysis tool was designed conservatively in determining the analyzable LC to insure that the segmented region was indeed part of the LC, and not noise. However, while the LC outlines might be slightly different in consecutive scans, the global 3D microstructure of the LC was still preserved (Figure 16).

The pore area and aspect ratio reported in this study were nearly identical to those reported by Ivers et al. from a small cohort of healthy subjects, where adaptive optics (AO-) SLO was used and the pores were segmented manually.[99] Akagi et al., reported similar aspect ratio but larger pore area using manual segmentation of AO-SLO images of both healthy and glaucomatous eyes.[100] Both previously described studies were limited by 2D analysis, as SLO has poor axial resolution, which may explain differences between studies. Furthermore, differences between the studies might be related to the different disease severity between the studies, analyzable LC, pore selection, and definition of the pore margin. Pore area, as measured in vivo in our study, was slightly larger than the area reported in histologic studies (~1460 and 920 μm^2), which might be related to the tissue shrinking during histological processing, the quantification of the surface pores only or due to the fact that both histologic studies included only healthy eyes. [101], [102] The LC parameters reported in Experiment 1-2 are all within 10% of the ones reported in Experiment 1-1.[94]

The relative imprecision varied between the diagnostic classes (Table 3). In general, there was a tendency of highest imprecision in the healthy group and lowest in the glaucoma suspects, though for most parameters the range was small. Only the imprecision for pore diameter was significantly higher in healthy compared to glaucoma eyes. The higher imprecision in the healthy

subjects may be due to the thicker prelaminar tissue in these subject, which decreases the scan quality and segmentation reliability at the level of the LC.

The main limitation of this study, similar to most other in vivo imaging studies analyzing the LC, was related to the ability to capture the entire LC, which was highly dependent on the characteristic of the blood vessels and prelaminar tissue overlying the LC. This inevitable limitation was related to the complex structure of the LC region and the physical properties of the OCT technology. Yet, the low imprecision reported in this study confirmed that the differences in the various parameters between consecutive scans for a given eye was small and therefore microstructural changes could be detected reliably.

In conclusion, automated segmentation for assessing 3D LC microstructure demonstrated low imprecision and high reproducibility. This analysis method represented a useful tool for future 3D analysis of the LC in vivo.

4.3 SUMMARY

We have demonstrated here that we were able of developing an automated segmentation algorithm that significantly reduces the time it takes to perform LC microstructure analysis. The analysis was completed over 100x faster than manual segmentation and performed at the same level as a manual observer. Furthermore, high repeatability in the analysis means that this technique would be useful in both cross sectional as well as longitudinal studies. As such, it sets the foundation for a technique of automated analysis of LC microstructure.

The ability to automatically quantify in vivo human 3D LC had several important advantages and implications. First, it is important to note that in vivo assessment offers some

advantages over assessment of LC microstructure in histology. In vivo imaging does not suffer from distortions due to the loss of pressure (intraocular pressure, intracranial pressure, or blood pressure), distortions in tissue during histology preparation or tissue degradation after death. Second, in vivo imaging also permitted repeated scanning and longitudinal analysis, as well as studies comprising of a more representative population than those who donate their eyes. Third, 3D analysis enabled thorough quantification of the complex 3D structure of the LC, which was more comprehensive than 2D or surface-projection studies performed so far in vivo. Fourth, automated segmentation analysis helped remove the subjectivity of manual segmentation and permitted rapid investigation of a large number of eyes. Finally, in vivo assessment would allow us to identify dynamic changes in the LC microstructure, such as pressure change, without being affected by post mortem changes.

5.0 EFFECT OF INTRAOCULAR AND INTRACRANIAL PRESSURES ON THE LAMINA CRIBROSA MICROSTRUCTURE

There still lacks an understanding of how IOP and ICP affects the LC microstructure of the eye, if at all. As there exists no method of non-invasively controlling and recording ICP in humans, we will be using an animal model to understand the acute effect of IOP and ICP changes on the LC microstructure of the eye, using the tools developed in Aim 1.

5.1 EXPERIMENT 2-1: ASSESSING THE EFFECTS OF ACUTE IOP AND ICP CHANGE ON LC MICROSTRUCTURE

It is crucial to first understand how the LC microstructure is altered due to pressure in an animal model before moving on to human studies, where there exist more confounding variables (race, co-morbidities etc.) as well as the ethical implications of invasively altering ICP. A primate model allows us to test how a large number of IOP and ICP combinations affect the LC microstructure of the eye in a controlled fashion, providing a fundamental understanding of the interaction between the pressures and the LC. As there exists no present knowledge on how IOP and ICP affects LC microstructure in vivo, it is be important to assess whether changes in IOP or ICP affect LC microstructure at all; the only animal previous animal study assessing the effects of both IOP and ICP on the eye looked only the changes in the optic nerve surface.[50]

The rationale behind performing this study in vivo is that traditional tissue testing such as tensile stretch are difficult for the small and inaccessible structures of the posterior human eye, such as the LC microstructure. [103], [104] Furthermore, examination of ex-vivo eyes can impact both tissue property as well as change the environment experienced by the eye (no ocular blood pressure, temperature change, cell death, inflammation etc.). The findings of this study will allow us to determine whether IOP or ICP actually affect the LC microstructure and allow us to translate those findings into human subjects.

By choosing a wide range of IOP and ICP conditions, our findings are applicable to a range of conditions that lead to vision loss, including ones other than primary open angle glaucoma. For example, investigating the acute effect of IOP rise on the LC microstructure improves our understanding of acute angle closure glaucoma, where blockage of the trabecular meshwork outflow can lead to a sudden rise in IOP. [105] Furthermore, investigating the effect of ICP on the eye improves our understanding of a range of diseases that can cause vision loss by elevating ICP, such as sleep apnea[106], idiopathic intracranial hypertension[107], [108] and brain tumors. We hypothesize that increasing IOP will cause beam thinning and increases in pore diameter and that increasing ICP will cause beam thickening and decreases in pore diameter.

Paragraph.

5.1.1 Animals and Methodology

5.1.1.1 Animals

Five healthy, adult, macaque monkeys were used for this experiment. All procedures in this study were approved by the University of Pittsburgh's Institutional animal care and use committee (IACUC) and adhered to both the guidelines set forth in the National Institute of

Health's Guide for the Care and Use of Laboratory Animals [109] and the Association of research in vision and ophthalmology (ARVO) statement for the use of animals in ophthalmic and vision research. This cohort included two females (Monkey 1 - age 12 years, Monkey 2 – age 15) and three males (Monkey 3 – age 14 years, Monkey 4 – age 8.5, Monkey 5 – age 8). Both eyes of monkey 5 were used to examine the association between eyes in the same primate.

5.1.1.2 Anesthesia

Animals were anesthetized with ketamine (20-30 mg/kg) and midazolam (0.25 mg/kg) and then intubated and maintained with isoflurane anesthesia (2%) for the duration of the experiment. Prior to imaging, animals were paralyzed using vecuronium bromide (2mg/hr) to reduce ocular movements during scanning, and were artificially ventilated to maintain an end-tidal CO₂ of 35mmHg. Animals were scanned with their body in the prone position and head held upright and facing the OCT device.

5.1.1.3 Pressure Control

IOP was controlled via gravity-based perfusion through a 27-gauge needle inserted into the anterior chamber after thorough irrigation of the cannula to remove all air bubbles. A saline reservoir was raised above the height of the globe to set the IOP (5, 15, 30, and 40mmHg). The lateral ventricle was cannulated with a lumbar catheter (Medtronic, Minneapolis, MN), also attached to a saline reservoir and thoroughly irrigated, to control ICP. The height of the reservoir was adjusted to achieve a target ICPs of 5, 10, 25 and 40mmHg, although it was not always possible to reach those exact target ICPs. ICP was simultaneously and continuously measured with a fiber-optic pressure sensor inserted into the parenchyma of the brain (ICP EXPRESS

monitoring system; DePuy Synthes, Raynham, MA). The pressure transducer was zeroed at eye level while submerged in saline solution.

5.1.1.4 Experimental Setting

The animals were anesthetized and OCT scans of the ONH region were acquired at baseline and at each pressure setting (Figure 19). ICP was adjusted and then IOP was modulated in the various pressure settings while acquiring OCT images at each setting. A minimum of 5 minutes were given after changing pressure to reduce the viscoelastic effect on the eye. [110] After completing all IOP modulations, ICP was adjusted to a different pressure and the IOP modulation was repeated.

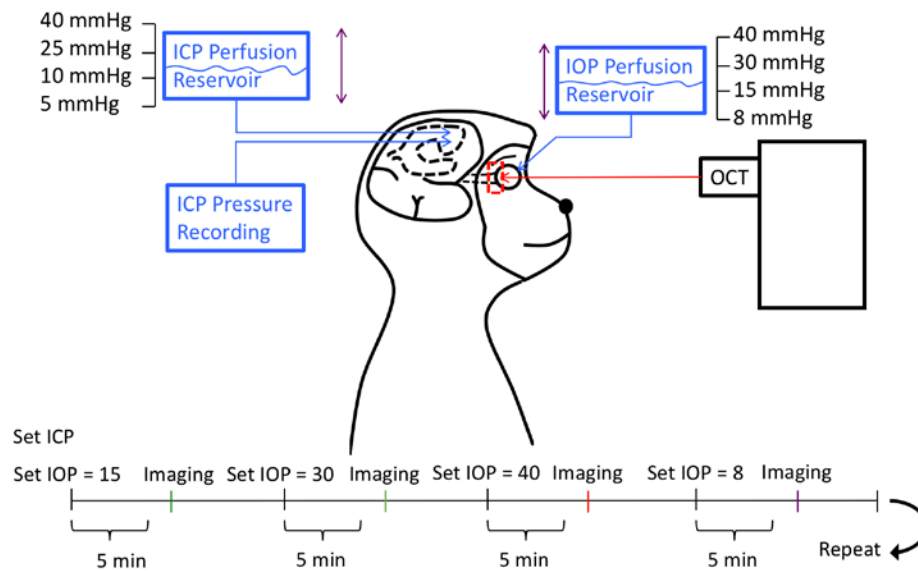


Figure 17. (A) Experimental setup. Intraocular pressure (IOP) and intracranial pressure (ICP) were controlled using a gravity-based perfusion system. OCT imaging of the lamina cribrosa (LC) (red box) was performed 5 minutes after altering IOP and ICP. At every given ICP, IOP was altered and the OPTIC NERVE HEAD was imaged after 5 minutes at every IOP condition. After completing all IOP conditions, a new ICP was set and the IOP conditions repeated.

5.1.1.5 OCT Imaging

The pupils were dilated using tropicamide for ease of image acquisition. A rigid gas permeable contact lens (Boston EO, Boston, MA) was fitted to each scanned eye to improve image quality. The eyes were kept open using a wire speculum and the cornea was kept moist with artificial tears every 5 minutes. At every IOP and ICP condition, 4 OCT scans of the LC were taken. All eyes were scanned in a 5mm x 5mm x 2mm volume (512 x 512 x 1024 samplings in both scanning settings) centered on the optic nerve and LC using the Bioptigen spectral domain OCT.

5.1.1.6 Image Analysis

Images were subjectively inspected and those where no LC microstructure was detected were discarded from analysis. Qualified images were segmented using the segmentation method presented in Aim 1, to quantify beam thickness, pore diameter and beam thickness to pore diameter ratio.[94], [111], [112]

The remaining images were subjectively graded for segmentation quality based on pores and beams visibility. An experienced observer masked to the experimental setting in which the images were acquired determined the image quality on a scale from 1-3, with 1 being the worst and 3 being the best quality (Figure 18).

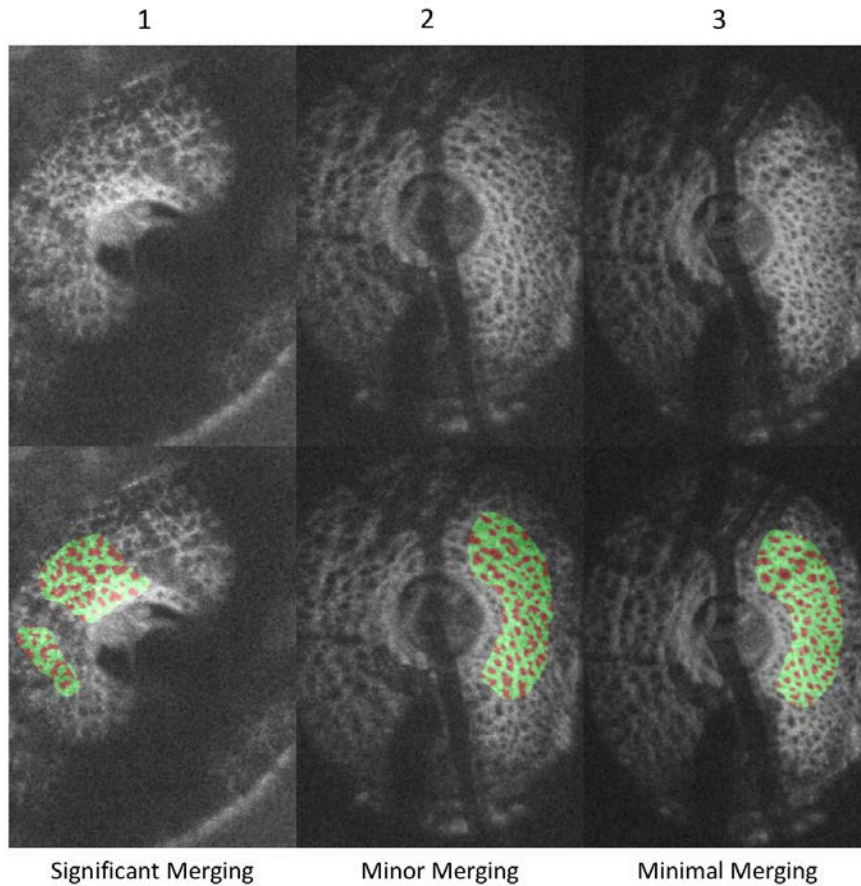


Figure 18. Assessment of segmentation quality. Examples of images rated as 1, 2, and 3.

Because the visible LC varied between images acquired in the various pressure settings, we limited the analysis only to regions visible in all images to prevent the confounding effect related to quantification of different areas of the LC. Images were registered by rigid-body translation and rotation in 3D to align the LC microstructure (Figure 19). A volume of the LC, visible on all scans, was used for analysis in order to determine the change in 3D LC microstructure on a corresponding region.

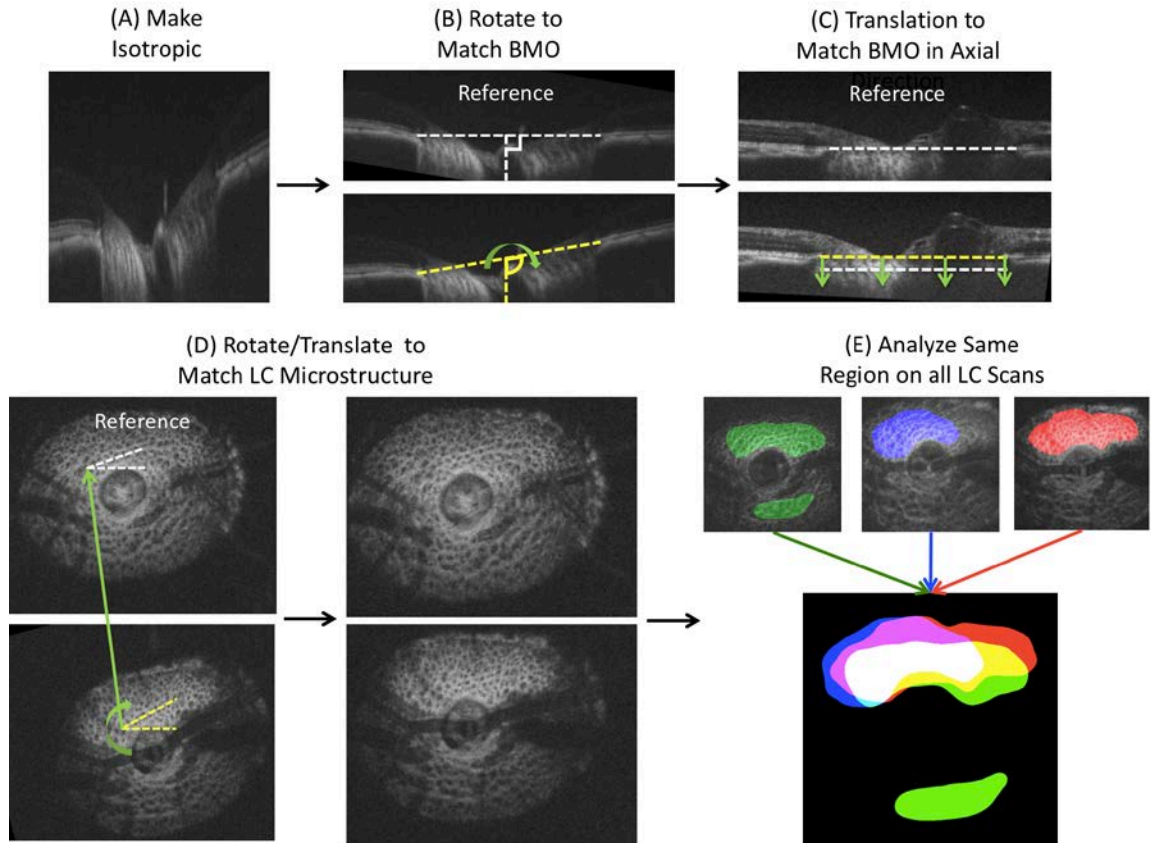


Figure 19. Image analysis procedure. (A) Images were adjusted for isotropic dimensions, (B) and rotated to match the angle of Bruch membrane opening (BMO). (C) Images were translated in the axial direction to match the axial height of the BMO. (D) The microstructures were aligned manually via 3D rotation and translation. (E) Visible LC was denoted and a common overlapping region (white color region) was used for analysis.

5.1.1.7 Reproducibility

The reproducibility of the segmentation analysis and quality grading was assessed by measuring the imprecision standard deviation of repeated measurements using a measurement error model. [98] The relative imprecision was computed by dividing imprecision standard deviation by the

average measurement. Low imprecision indicated high reproducibility in the segmentation as well as the quality grading.

5.1.1.8 Statistical Analysis

Random intercept linear mixed effects models were used to determine the effect of either IOP or ICP and image quality on LC microstructure, while the other pressure remained at baseline (IOP = 15mmHg and ICP = 10 mmHg).[91] The linear mixed model allowed us to account for the use of both eyes in some primates.

5.1.2 Results

Images were acquired from six eyes of the five animals and scans with non-visible LC were removed from the analysis. Worse image quality tended to occur at the extreme IOP conditions (5 – 10 mmHg and 40 – 50 mmHg), as well as extremely high ICP (Figure 20).

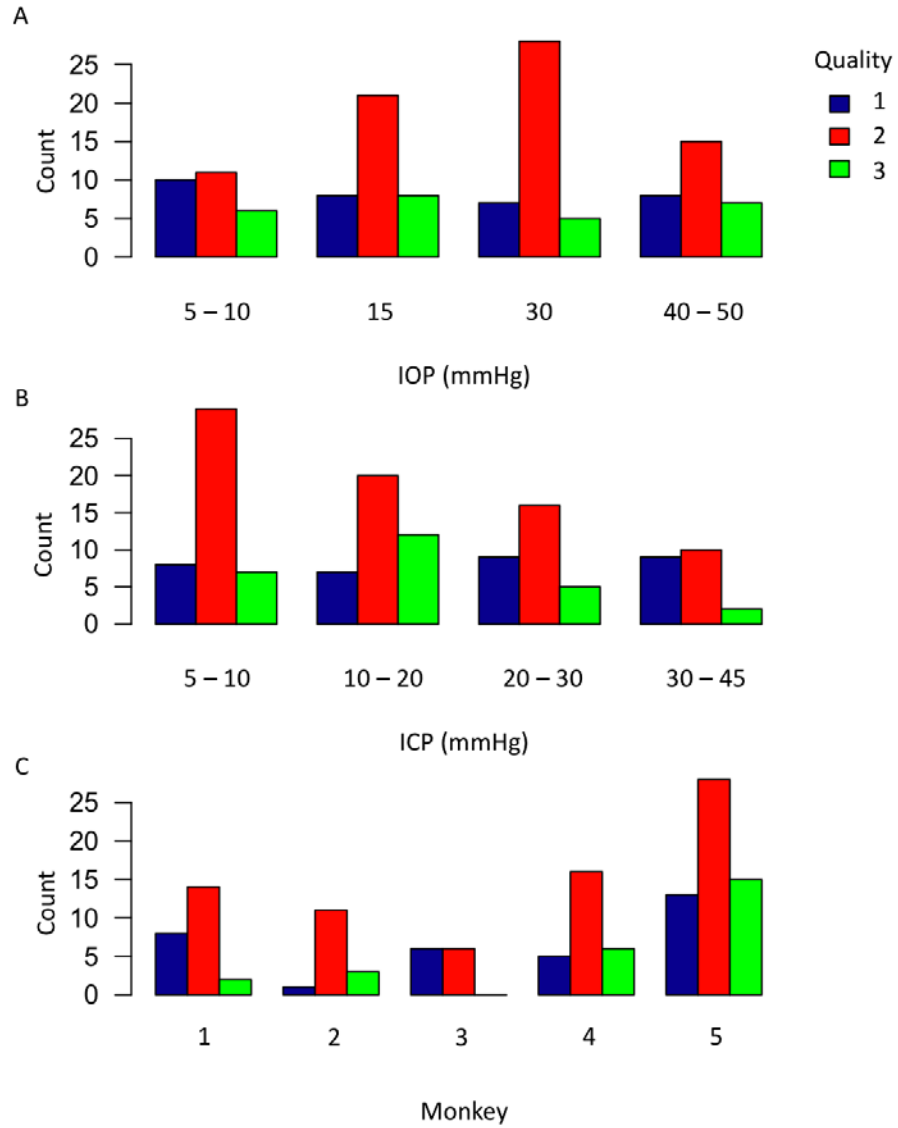


Figure 20. Image quality metrics. Histogram of (A) IOP setting per image quality and (b) ICP setting per image quality (C) image quality per monkey.

5.1.2.1 Repeatability

The repeatability of measurements was excellent, with all LC microstructure parameters having a relative imprecision SD less than 5%, with beam thickness and pore diameter performing better than beam-pore ratio. The manual delineation of quality had a larger relative imprecision, close to 10%. However, it is important to note that the quality difference never exceed 1 between the two graders.

5.1.2.2 How LC Microstructure Changed with IOP

We could not detect a statistically significant association between IOP and LC microstructure at baseline ICP (10mmHg). However, the subjective grading for image quality was associated with the LC microstructure parameters, with higher quality associated with smaller beams thickness, larger pore diameter and decrease beam thickness to pore diameter ratio. (Table 4)

Table 4. Estimate of the effect of intraocular pressure (IOP) and image quality on lamina cribrosa (LC) microstructure. Bold font marked statistically significant effect. Au – arbitrary units.

LC Parameter	Parameter	Effect Size	Standard Error	P
Beam thickness (pixels/mmHg)	IOP	-0.005	0.006	0.488
	Quality	-0.305	0.131	0.025
Pore Diameter (pixels/mmHg)	IOP	-0.007	0.006	0.226
	Quality	0.284	0.114	0.018
Beam Pore Ratio (Au/mmHg)	IOP	0.000	0.001	0.856
	Quality	-0.042	0.014	0.004

5.1.2.3 How LC microstructure changed with ICP

We could not detect a statistically significant association between ICP and LC microstructure at baseline ICP. Furthermore, we did not detect a statistically significant association between quality and LC microstructure when assessing between ICP and LC microstructure. (Table 5)

Table 5. Estimate of the effect of intracranial pressure (ICP) and image quality on lamina cribrosa (LC) microstructure. Bold font marked statistically significant effect.

LC Parameter	Parameter	Effect Size	Standard Error	P
Beam thickness	ICP	0.006	0.009	0.537
	Quality	-0.004	0.154	0.981
Pore Diameter	ICP	-0.009	0.007	0.232
	Quality	0.168	0.122	0.178
Beam Pore Ratio	ICP	0.001	0.001	0.371
	Quality	-0.015	0.014	0.284

5.1.3 Discussion

This study represents the first in vivo characterization of the acute effects of IOP and ICP on the 3D LC microstructure. We demonstrate the ability to visualize and quantify in vivo LC microstructure changes as a result of altered IOP and ICP. While previous studies provide epidemiologic evidence of a potential link in the role of IOP and ICP with disease,[44], [48], [113], [114] our study represents the first attempt to assess in an in vivo model that the LC microstructure acutely deforms in accordance under the influence of both IOP and ICP.

Unfortunately, when assessing how IOP or ICP alone deformed LC microstructure while keeping the other pressure normal, we did not find a statistically significant difference in how

IOP or ICP alone deformed LC microstructure. This is illustrated in the slope of how LC microstructure change from IOP and ICP being non-significantly different from 0. Despite this, it is clear subjectively that there are indeed changes occurring at the level of the LC microstructure, with larger pores seen in some of the higher IOP conditions.

While these findings are disappointing, it is likely due to the limited data provided by only 5 monkey at either baseline IOP or baseline ICP. This results in a maximum of 8 data points per eye, with most being less than 8 due to poor image quality at the extreme ends of IOP and ICP. Therefore, it will be necessary to include all the available data in a more comprehensive model, as will be discussed in Experiment 2-2, to fully understand how the LC microstructure deforms to a combination of IOP and ICP.

The effect of quality on the LC microstructure is an important aspect to consider when analyzing how LC microstructure change. As can be seen in Table 4, better quality segmentations were associated with increased pore diameter, decreased beam thickness and increased beam thickness to pore diameter ratio. This is logical as poorer image quality leads to blur the LC, resulting in poorly defined beams and pore structures. The blurriness tends to reduce the size of smaller pores, making them poorly defined. This results in segmentations which overestimates the beam thickness and underestimates pore size, resulting in the findings seen here. The fact that LC microstructure was associated with quality when assessing IOP, but not ICP, is likely a result of the fact that small ICP changes is not expected to degrade the ocular media through which OCT images.

5.2 EXPERIMENT 2-2: ASSESSING THE RESPONSE OF LC MICROSTRUCTURE TO BOTH IOP AND ICP

Due to the complex anatomy at the level of the optic nerve head of the eye, especially given the regions over which IOP and ICP act, additional models are required to understand the behavior of the LC microstructure. Specifically, it will be important to not look at IOP or ICP separately, but to combine together in a model to understand how they work with one another.

One important consideration not addressed in Experiment 2-1 is the idea that the effect of IOP on the eye may depend on the current ICP level, with the opposite being true as well. This can be seen intuitively in Figure 21, where despite both having the same TLPD, represent very different conditions for the eye. In this case, it would be critical to understand how ICP interacts with the effect of TLPD on the eye.

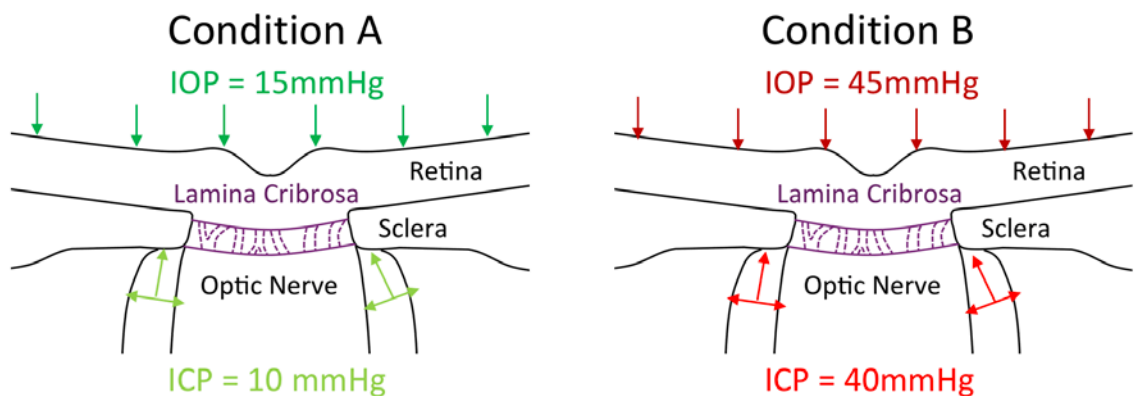


Figure 21. Diagram demonstrating the optic nerve under two different pressure conditions. In both cases, the translamellar pressure difference would be 5mmHg.

While a simple linear model is useful to identify change, it is unlikely that a simple linear model as outlined in Experiment 2-1 would capture the full effect of both IOP and ICP on the eye.

The effect of IOP and ICP are likely to be complex. For example, most biological materials are not linear elastic and would not be expected to have a linear stress-strain curve.[115] There already exists evidence of non-linearity in mechanical response in the eye; scleral biomechanics in monkey eyes show distinct anisotropic and non-linear mechanical response to changes in IOP.[116]

Therefore, there are three major questions we are interested in addressing the Experiment 2-2. First, we want to see whether including both IOP and ICP in the same model improved our ability to assess change in the LC microstructure. Second, we want to see whether the addition of interaction component to our models will improve our models. Finally, we want to examine the effect of adding a non-linear quadratic component to IOP and ICP. We hypothesize that there will be significant interactions between IOP and ICP on the eye and that the eyes behaved non-linearly with respect to pressure.

5.2.1 Animals and Methodology

The animals were the same as described in Experiment 2-1. The methodology remained the same as Experiment 2-1 until the statistical analysis.

5.2.1.1 Statistical Analysis – Model 1, Linear Models

The models used assessed how IOP, ICP, translaminal pressure difference (TLPD; IOP-ICP), and image quality affected LC microstructure. The models can be seen in Table 6, which the specific equation for IOP + ICP + quality shown in Equation 3.

Table 6. List of model name as well as the parameters used inside the model.

Linear Models Tested
TLPD + quality
IOP + ICP + quality

$$\text{LC Microstructure} = \alpha + \alpha_i + \eta \text{ TLPD} + \beta \text{ ICP} + \nu \text{ quality}$$

Equation 3: Generalized form of the linear mixed effect models for assessment of LC microstructure with both TLPD and ICP components. The specific model written here is TLPD + ICP + quality. Red outlines the variables and green outlines the estimates of the slope for that particular variable.

Akaike information criterion (AIC), a numerical method of balancing between model fit and model complexity, was used to select the best model where the model with lower AIC being superior. A $p < 0.05$ was considered as statistically significant. R Language and Environment for Statistical Computing program (version 3.1.1), was used for the statistical analysis. [91]

5.2.1.2 Statistical Analysis – Model 2, Interaction Model

In order to test the interaction between the various pressure conditions, interactions were added to the models tested earlier, as well as from Experiment 2-1. The specific models tested is shown in Table 7 and an example of the linear mixed effect model for TLPD * ICP + quality is shown in Equation 4. Note that the interaction models have their base effects, both TLPD and ICP individually, as well as the interaction between the two. The rationale behind using models where TLPD interact with ICP is because TLPD alone may not fully describe the relationship between IOP and ICP, as illustrated in Figure 21.

Table 7. List of interaction models tested as part of the analysis.

Interaction Models
IOP + quality + (IOP x quality)
ICP + quality + (ICP x quality)
TLPD + ICP + quality + (TLPD x ICP)
TLPD + ICP + quality + (TLPD x ICP) + (ICP x quality) + (TLPD x ICP x quality)
IOP + ICP + quality + (IOP x ICP)
IOP + ICP + quality + (IOP x ICP) + (ICP x quality) + (IOP x ICP x quality)
TLPD + IOP + quality + (TLPD x IOP)

$$\text{LC Microstructure} = \alpha + \alpha_i + \eta \text{ TLPD} + \beta \text{ ICP} +$$

$$\eta \text{ TLPD ICP} + \nu \text{ quality}$$

Equation 4: Generalized form of the linear mixed effect models for assessment of LC microstructure with interaction between the variables. The specific model written here is TLPD * ICP + quality. Red outlines the interaction variables and green outlines the non-interaction variables.

5.2.1.3 Statistical Analysis – Model 3, Quadratic model

In order to assess non-linear effects, an additional quadratic component was added to the best model from the interaction models. The generalized form of the model can be seen in Equation 5. Similar to Experiment 2-1, AIC was used to select the better model, with the model with lower AIC being superior. It is important to note that due to the complexity of the model, p-values on the individual component of the linear mixed effect model are not as meaningful. Therefore, all the effects were plotted to comprehend how LC microstructure changed with IOP and ICP. R Language and Environment for Statistical Computing program (version 3.1.1), was used for the statistical analysis. [91]

$$\text{LC Microstructure} = \alpha + \alpha_i + \eta \text{ TLPD} + \beta \text{ TLPD}^2 + \gamma \text{ ICP} + \delta \text{ ICP}^2 + \eta \text{ TLP ICP} + \nu \text{ quality}$$

Equation 5: Generalized form of the linear mixed effect models, with quadratic components (red) and interactions (green), for assessment of LC microstructure with interaction between the variables.

5.2.2 Results

5.2.2.1 Model 1 – TLPD and Quality

When assessing the effect of TLPD on the LC parameters, the linear mixed effect models showed a trend for decreased beam thickness, increased pore diameter, and decreased beam to pore ratio with increased TLPD (Figure 6). Modeling the effect of TLPD and scan quality on LC parameters have shown that both TLPD and scan quality were statistically significantly associated with each of the LC parameters (Table 8). Larger TLPD was associated with reduced beam thickness, increase in pore diameter and decrease in beam-pore ratio. Despite the dependence on quality, the trend of LC microstructure vs. TLPD was consistent regardless of the signal quality cutoff that was used.

Table 8. Estimate of the effect of translaminar pressure difference (TLPD) and image quality on lamina cribrosa (LC) microstructure. Bold font marked statistically significant effect. Au – arbitrary units.

LC Parameter	Parameter	Effect Size	Standard Error	P
Beam Thickness	TLPD ($\mu\text{m}/\text{mmHg}$)	-0.033	0.016	0.036
	Quality ($\mu\text{m}/\text{au}$)	-0.801	0.376	0.037
Pore Diameter	TLPD ($\mu\text{m}/\text{mmHg}$)	0.019	0.009	0.045
	Quality ($\mu\text{m}/\text{au}$)	1.160	0.221	0.000
Beam Pore Ratio	TLPD ($\mu\text{m}/\text{mmHg}$)	-0.002	0.001	0.004
	Quality ($\mu\text{m}/\text{au}$)	-0.079	0.016	<0.001

5.2.2.2 Model 1 – IOP, ICP and Quality

Models that included IOP, ICP and image quality as predictors for LC microstructure parameters demonstrated a statistically significant negative effect for IOP on beam thickness and beam-pore ratio (Table 9). ICP was not significant in any of the models whereas image quality had a significant effect on all three parameters.

Table 9. Estimate of the effect of intraocular pressure (IOP), intracranial pressure (ICP) and image quality on lamina cribrosa (LC) microstructure. Bold font marked statistically significant effect. Au – arbitrary units.

LC Parameter	Parameter	Effect Size	Standard Error	P
Beam Thickness	IOP ($\mu\text{m}/\text{mmHg}$)	-0.043	0.020	0.033
	ICP ($\mu\text{m}/\text{mmHg}$)	0.018	0.025	0.479
	Quality ($\mu\text{m}/\text{au}$)	-0.861	0.384	0.029
Pore Diameter	IOP ($\mu\text{m}/\text{mmHg}$)	0.020	0.012	0.103
	ICP ($\mu\text{m}/\text{mmHg}$)	-0.018	0.015	0.240
	Quality ($\mu\text{m}/\text{au}$)	1.165	0.227	0.000
Beam Pore Ratio	IOP ($\mu\text{m}/\text{mmHg}$)	-0.0023	0.0009	0.011
	ICP ($\mu\text{m}/\text{mmHg}$)	0.0017	0.0011	0.125
	Quality ($\mu\text{m}/\text{au}$)	-0.0798	0.0165	<0.001

5.2.2.3 Model 2 – Interaction models

As a number of models were assessed, it was not possible to list all the AIC values for each of the different model. However, in general, the models including interaction between the variables tend to be worse (higher AIC) compared to the models without interactions between the variables. However, in every case, there were specific interaction models that performed significantly better than the non-interaction models. The performance of the models for beam thickness (Table 10), pore diameter (Table 11) and beam thickness to pore diameter ratio (Table 12) were listed below.

Table 10. Comparison of the various models with interactions for beam thickness. Lower AIC denotes the better model. * denotes interaction effect between the variables. Bold denotes best performing model as judged by AIC.

Model	AIC
Best non-interaction model	
TLPD + quality	617.3
Interaction models	
IOP + quality + (IOP x quality)	618.8
ICP + quality + (ICP x quality)	620.6
TLPD + ICP + quality + (TLPD x ICP)	615.4
TLPD + ICP + quality + (TLPD x ICP) + (ICP x quality) + (TLPD x ICP x quality)	620.3
IOP + ICP + quality + (IOP x ICP)	620.6
IOP + ICP + quality + (IOP x ICP) + (ICP x quality) + (IOP x ICP x quality)	624.2
TLPD + IOP + quality + (TLPD x IOP)	619.6

The best model, judged via the lowest AIC for beam thickness (Table 10) was TLPD * ICP + quality, with TLPD + quality coming close as a second option (less than 2 AIC difference). However, it is important to note that the models did not always improve with an additional interaction term. In fact, the worst model was the one with the most variables: TLPD * IOP * quality.

Table 11. Comparison of the various models with and without interactions for pore diameter. Lower AIC denotes the better model. * denotes interaction effect between the variables. Bold denotes best performing model as judged by AIC.

Model	AIC
Best non-interaction model	
TLPD + quality	574.1
Interaction models	
IOP + quality + (IOP x quality)	575.0
ICP + quality + (ICP x quality)	576.0
TLPD + ICP + quality + (TLPD x ICP)	567.7
TLPD + ICP + quality + (TLPD x ICP) + (ICP x quality) + (TLPD x ICP x quality)	571.4
IOP + ICP + quality + (IOP x ICP)	570.9
IOP + ICP + quality + (IOP x ICP) + (ICP x quality) + (IOP x ICP x quality)	575.6
TLPD + IOP + quality + (TLPD x IOP)	575.3
Best non-interaction model	580.8

For pore diameter, the best model was TLPD * ICP + quality, without any other model within 2 AIC from it (Table 11). Finally, for beam thickness to pore diameter ratio, the best model was also TLPD * ICP + quality, without any other model that were comparable.

Table 12. Comparison of the various models with and without interactions for beam thickness to pore diameter ratio. Lower AIC denotes the better model. * denotes interaction effect between the variables. Bold denotes best performing model as judged by AIC.

Best non-interaction model	AIC
TLPD + quality	-293.7
Interaction models	
IOP + quality + (IOP x quality)	-291.4
ICP + quality + (ICP x quality)	-291.2
TLPD + ICP + quality + (TLPD x ICP)	-300.8
TLPD + ICP + quality + (TLPD x ICP) + (ICP x quality) + (TLPD x ICP x quality)	-297.4
IOP + ICP + quality + (IOP x ICP)	-290.1
IOP + ICP + quality + (IOP x ICP) + (ICP x quality) + (IOP x ICP x quality)	-286.8
TLPD + IOP + quality + (TLPD x IOP)	-289.7
Best non-interaction model	
TLPD + quality	-284.6

As the interaction terms increased the complexity of the model, the interpretation of the findings of the model were interpreted graphically. The plots showing how beam thickness (Figure 22), pore diameter (Figure 23), and beam thickness to pore diameter ratio (Figure 24) was altered as a function of IOP and ICP. In all cases, there were strong interactions, which can be seen by the contour map as well as the sampled points at specific IOP and ICP. Furthermore, all 3 plots show a region at around 10mmHg – 20mmHg ICP, where increasing IOP results in minimal deformation on LC microstructure.

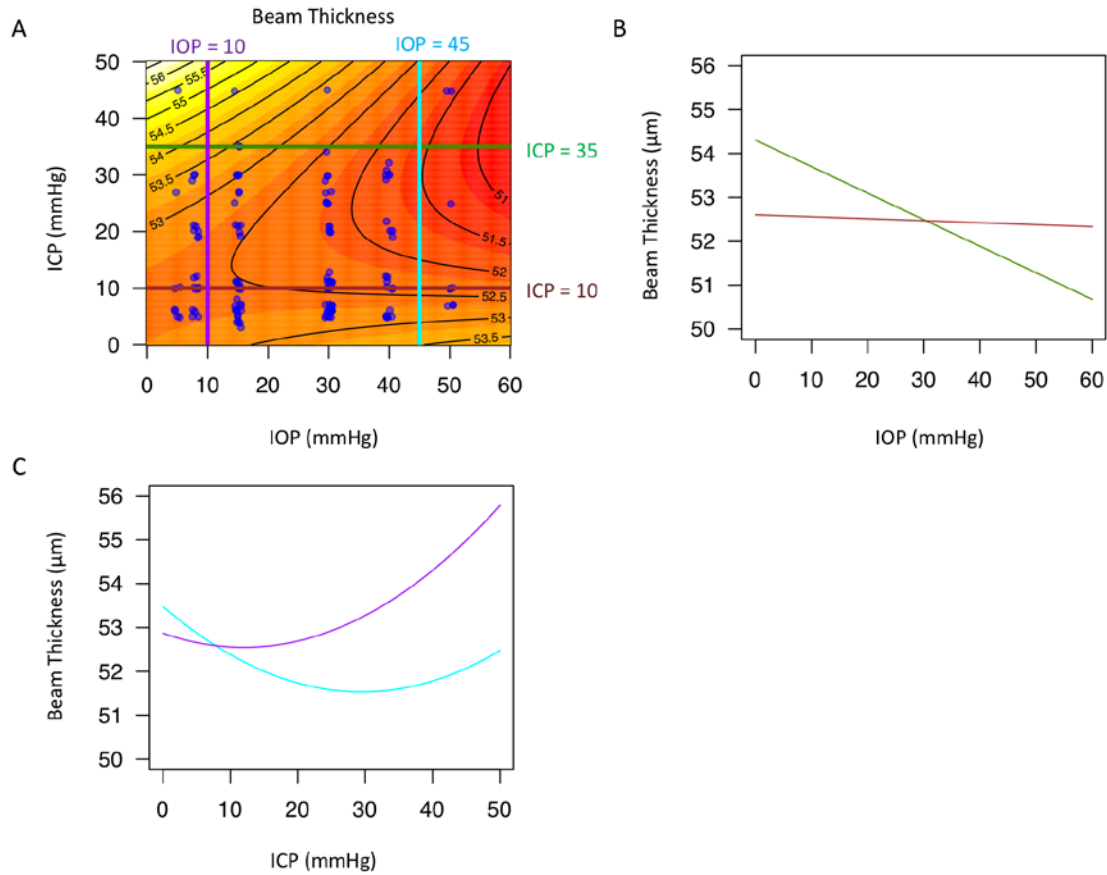


Figure 22. Change in LC beam thickness to pore diameter ratio with intraocular (IOP) and intracranial (ICP) pressure. (A) Contour plot showing change in beam pore ratio as a function of IOP and ICP. Black lines indicate the contour line at a particular value. Translucent gray dots indicate points sampled in the dataset. A sample of the contour plot at a set of (B) ICP (ICP = 10mmHg, light green; ICP = 40mmHg, dark green) and (C) IOP (IOP = 10mmHg, purple, IOP = 45mmHg) demonstrate the complex interaction between IOP and ICP on beam thickness.

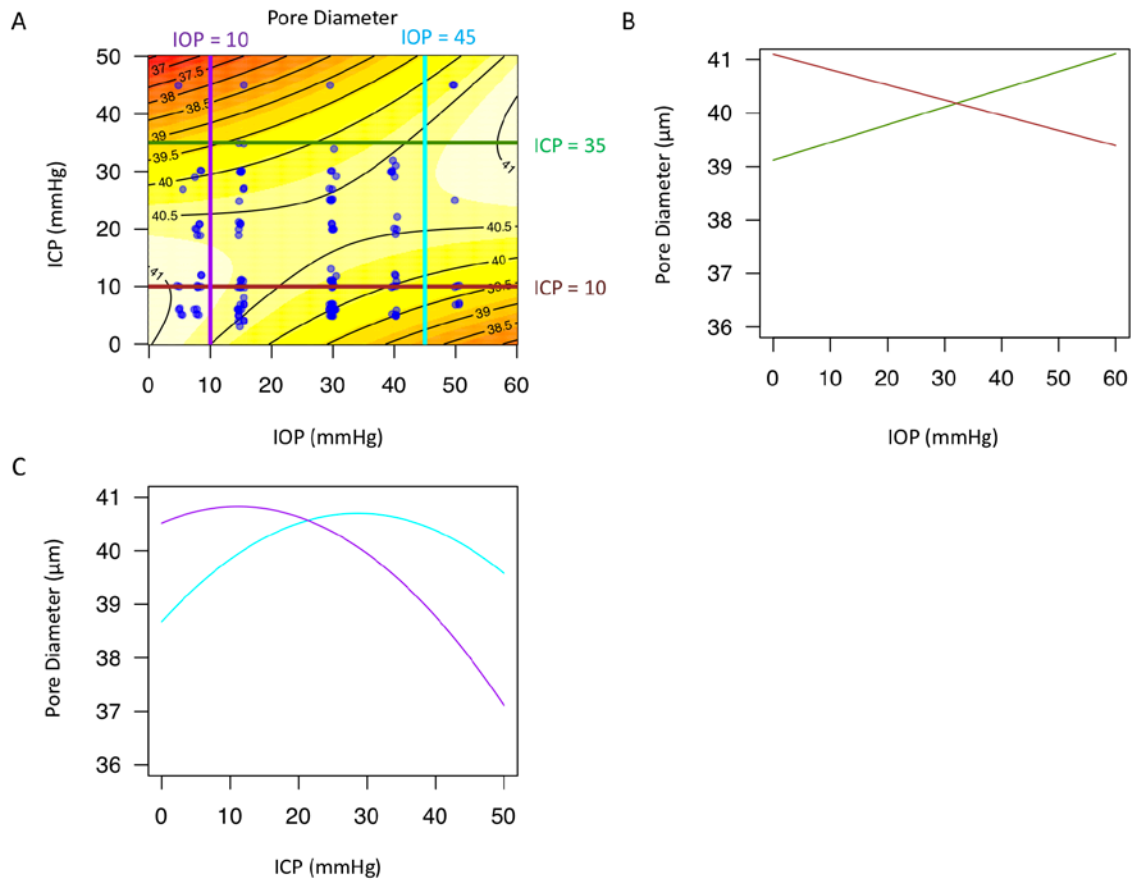


Figure 23. Change in LC pore diameter with intraocular (IOP) and intracranial (ICP) pressure. (A) Contour plot showing change in beam pore ratio as a function of IOP and ICP. Black lines indicate the contour line at a particular value. Translucent gray dots indicate points sampled in the dataset. A sample of the contour plot at a set of (B) ICP (ICP = 10mmHg, light green; ICP = 40mmHg, dark green) and (C) IOP (IOP = 10mmHg, purple, IOP = 45mmHg) demonstrate the complex interaction between IOP and ICP on pore diameter.

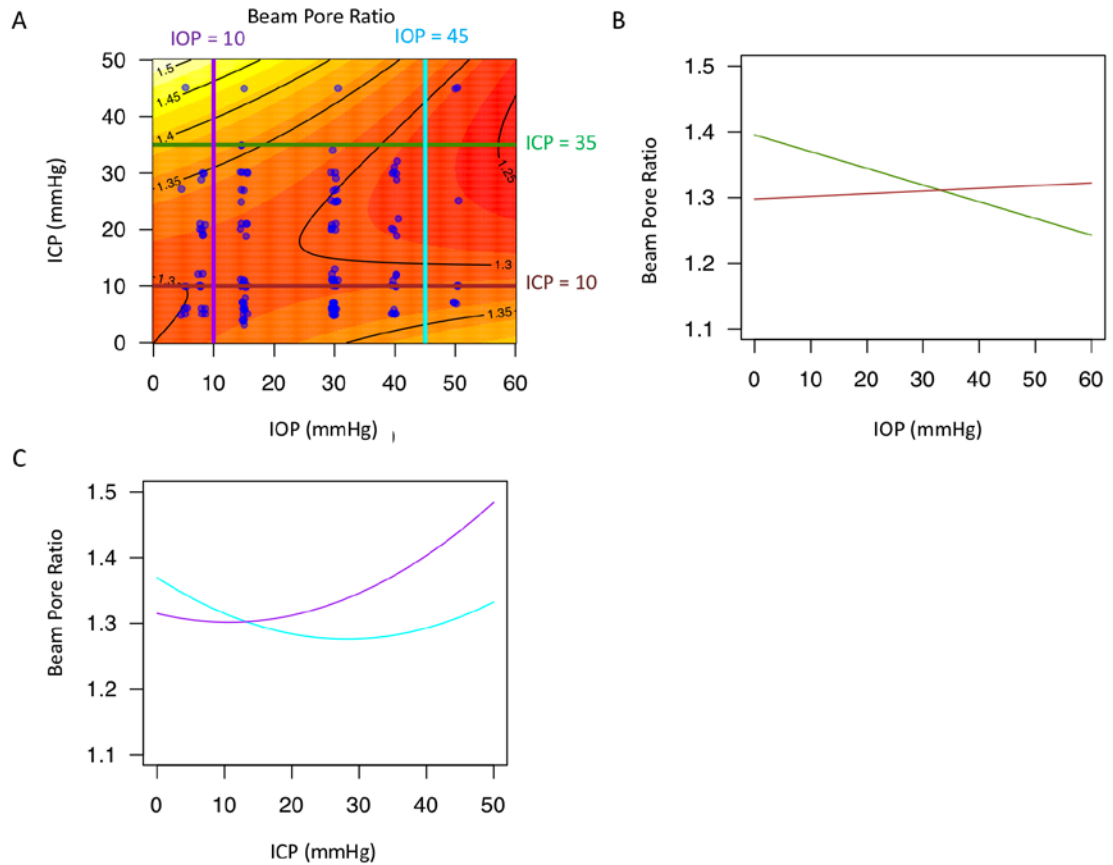


Figure 24. Change in LC beam thickness to pore diameter ratio with intraocular (IOP) and intracranial (ICP) pressure. (A-C) Contour plot showing change in beam thickness as a function of IOP and ICP. Black lines indicate the contour line at a particular value. Transparent gray dots indicate points sampled in the dataset. A sample of the contour plot at a set of (B) ICP (ICP = 10mmHg, light green; ICP = 40mmHg, dark green) and (C) IOP (IOP = 10mmHg, purple, IOP = 45mmHg) demonstrate the complex interaction between IOP and ICP on beam thickness to pore diameter ratio.

5.2.2.4 Model 3 – Quadratic Model

The addition of quadratic components to the best model from the interaction models significantly improved the AIC of two of the model (> 2 decrease), but not for pore diameter (Table 13). Overall, the trend of how IOP and ICP affected the LC microstructure did not change.

Table 13. Comparison of AIC of models with only interactions with models with interactions and quadratic components.

LC microstructure parameter	Interaction only model	Interaction + quadratic model
Beam thickness	615.4	605.3
Pore diameter	567.7	571.3
Beam thickness to pore diameter ratio	-300.8	-306.3

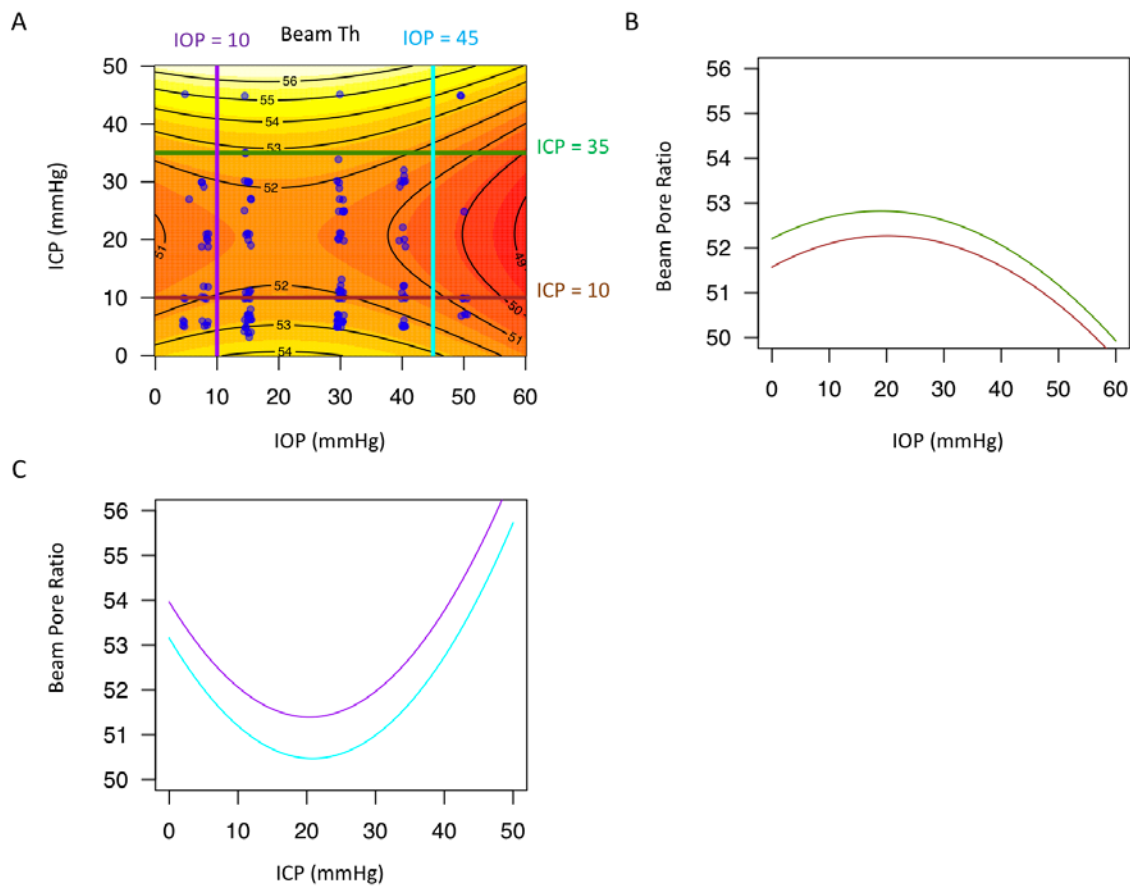


Figure 25. Quadratic model of how IOP and ICP influence beam thickness. (A) Heat map of how IOP and ICP affect the beam thickness, red indicates lower values, while yellow indicate higher value. Blue dots indicate the points with actual data in the results. Lines indicates the samplings taken to create plot (B) and (C). (B) Beam thickness to pore diameter as an influence of IOP, with two separate ICP shown (10 – brown, 45 – green). (C) Beam thickness to pore diameter as an influence of ICP, with two separate IOP shown (10 – purple, 45 – teal).

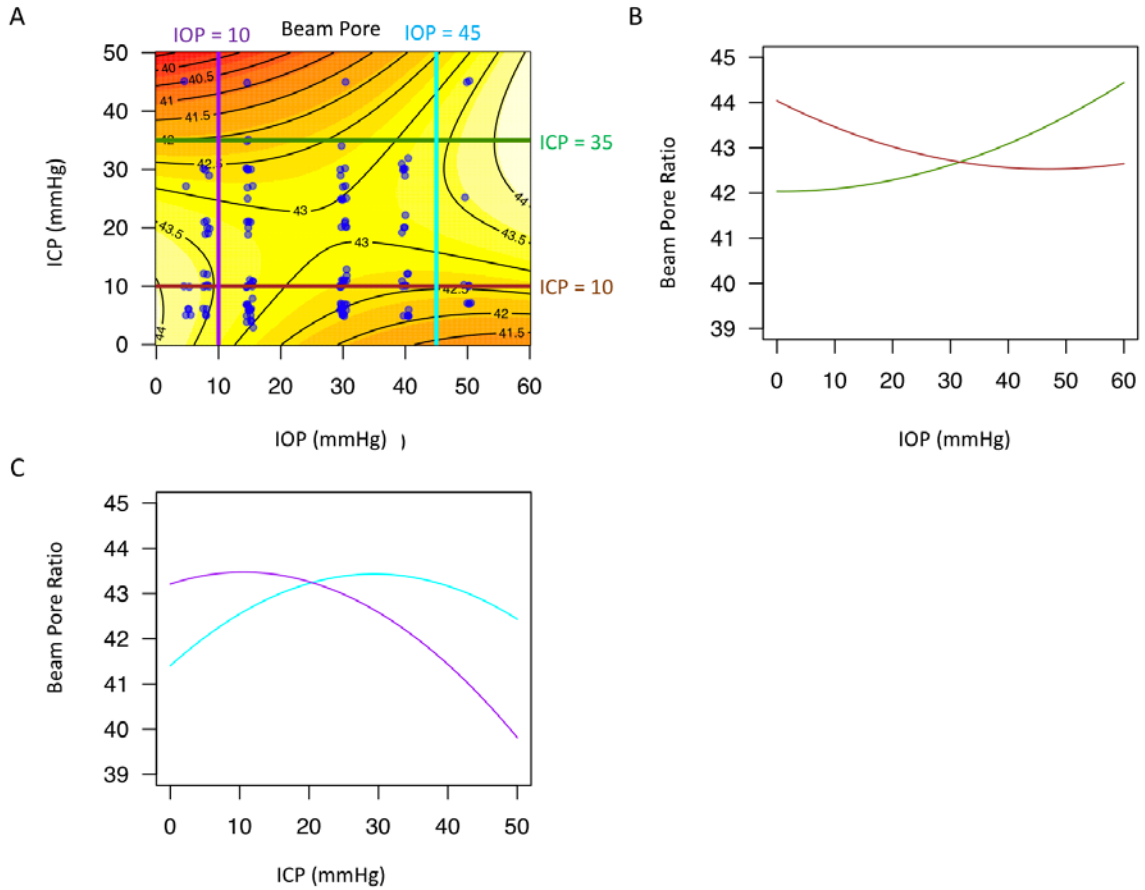


Figure 26. Quadratic model of how IOP and ICP influence pore diameter. (A) Heat map of how IOP and ICP affect the beam thickness, red indicates lower values, while yellow indicate higher value. Blue dots indicate the points with actual data in the results. Lines indicates the samplings taken to create plot (B) and (C). (B) Beam thickness to pore diameter as an influence of IOP, with two separate ICP shown (10 – brown, 45 – green). (C) Beam thickness to pore diameter as an influence of ICP, with two separate IOP shown (10 – purple, 45 – teal).

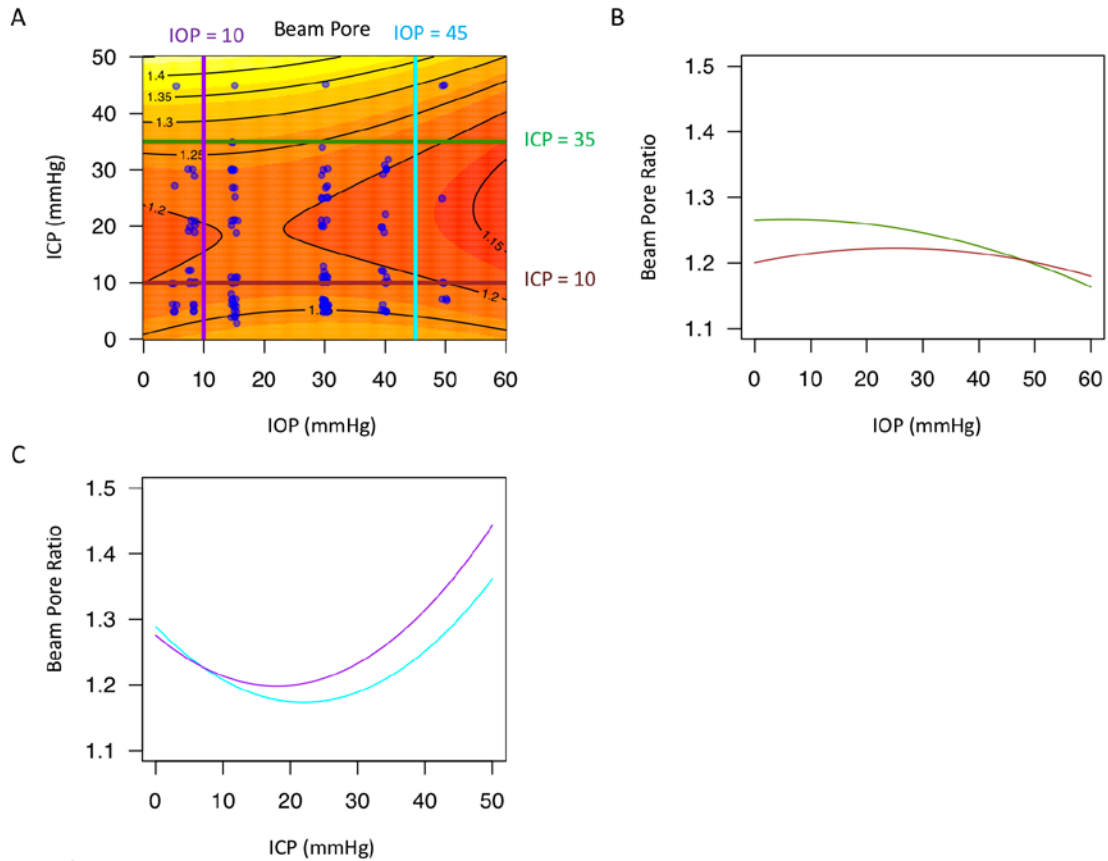


Figure 27. Quadratic model of how IOP and ICP influence beam thickness to pore diameter ratio. (A) Heat map of how IOP and ICP affect the beam thickness to pore diameter ratio, red indicates lower values, while yellow indicate higher value. Blue dots indicate the points with actual data in the results. Lines indicates the samplings taken to create plot (B) and (C). (B) Beam thickness to pore diameter as an influence of IOP, with two separate ICP shown (10 – brown, 45 – green). (C) Beam thickness to pore diameter as an influence of ICP, with two separate IOP shown (10 – purple, 45 – teal).

5.2.3 Discussion

This experiment represents the first in vivo report of how both IOP and ICP alter the LC microstructure. It enables us to identify that both IOP and ICP act together to affect the LC, with

a complex interaction between IOP and ICP. Furthermore, we find that a non-linear model is a better fit for assessing how beam thickness and beam thickness versus pore diameter ratio are affected by changes in IOP and ICP.

5.2.3.1 Model 1 – Linear Models

Using AIC analysis, we demonstrate that models with TLPD are more informative than those having the IOP and ICP separately. This finding is in agreement with a previous study that demonstrated that TLPD is a better predictor of optic disc surface changes than either IOP or ICP alone.[50] This emphasizes the importance of considering both IOP and ICP when aiming to accurately characterize the microstructure response to pressure. This finding has to be cautiously interpreted as it might be confounded by the relatively small sample size (which favors simpler models when assessing AIC).

In normal physiological situations, IOP is higher than ICP, resulting in a TLPD of approximately 5mmHg.[51], [117] Therefore, a TLPD much higher than 5mmHg represent a glaucomatous phenotype, while lower TLPD much lower than 5mmHg represent an intracranial hypertension phenotype. In cases of high TLPD, we identified beam thinning and pore enlargement. There are a variety of mechanisms through which beam thinning and pore enlargement could result in disease. First, the pore expansion could result in stretching and activation of the astrocytes along with biological responses such as extracellular matrix remodeling. [118], [119] Second, damage from acute deformation may also have a vascular component. Capillaries pass through the LC beams, nourishing the axonal bundles passing through. [120] Beam strain and thinning can compromise perfusion and nourishment to the axon bundles, especially given the expansion of axonal pores.

Low TLPD, representing situations with elevated intracranial pressure, are associated with beam thickening and shrinking of the pores, which may be explained by ICP acting concentrically in the sub-arachnoid space around the optic nerve (Figure 3). These microstructural changes can lead to strangulation of the axoplasmic flow, consistent with previous models demonstrating impaired axoplasmic transport at the level of the LC in animal models of papilledema. [121] These changes may contribute to the swelling and substantial deformation of the ONH tissues associated with intracranial hypertension. [122]

When we model the effect of IOP and ICP on LC parameters, only IOP was significantly associated with LC microstructure (Table 2). This is a bit counterintuitive as one might hypothesize that ICP itself would have a direct effect on LC microstructure, as elevated ICP in a concentric ring around the optic nerve would cause compression of the LC, leading to beam thickening and reduced pore diameter. While the results for ICP are compatible with these trends, they are not significant and weaker than the effect of IOP. These results suggest that ICP acts to modulate the effect of IOP, but may not strongly deform LC microstructure by itself. The effect of acute ICP and IOP modulation on the ONH surface [50] and the LC surface [123] has been previously reported. However, it is important to recognize that the cited studies assessed surface changes, which is not necessarily indicative of what is occurring in the LC microstructure.

The microstructural changes in LC we reported, are in the same magnitude as previously modeled.[124] As expected, a marked difference in the response to pressure modulations was noted between animals, which may reflect the individual biomechanical properties of each primate LC. This highlights the importance of analyzing eye specific response to changes in pressure, rather than pooling across animals, and of developing methods to determine

biomechanical properties of individual eyes. [103] The variability of the LC microstructure's response to changes in IOP and ICP may help explain the variability in response to these pressures in diseases such as glaucoma [33] and intracranial hypertension. [125]

5.2.3.2 Model 2 – Interactions model

As per our initial hypothesis, there is a significant interaction between how IOP and ICP affected LC microstructure. It is critical to note that not just any interactions improved the AIC. In fact, adding interactions generally made the models worse. This makes sense when considering the definition of AIC, which balances both model fit and model complexity. Models which only add complexity, without improving fit, were penalized.

The TLPD * ICP + quality model is substantially better than any other model, with or without interactions. The strength of the model can be seen in that it was the best model for assessing all three LC microstructure parameters. This model has all the characteristics we would hypothesize to be important: a significant interaction between TLPD and ICP, as well as the presence of both IOP (in the form of TLPD) and ICP information. Again, we can go back to our diagram in Figure 21, a TLPD of 5mmHg at an ICP of 10mmHg (IOP = 15mmHg) is a very different clinical situation than a TLPD of 5mmHg at an ICP of 30 (IOP = 45mmHg). Therefore, it would be critical to have ICP interacting with TLPD.

Looking on the plots gives a sense of the complexities of the results. While the linear models (Model 1) show that beams decrease in thickness and pores increase in diameter with increased TLPD, the interaction analysis shows a much more complex trend. The trend seen in the linear models only appeared at high ICP levels. Furthermore, at very low ICP levels, there appears to be a trend towards increasing beam thickness and decreasing pore diameter with increases in IOP. These findings demonstrate the importance of adding the interaction term, as

the effect of IOP was highly dependent on the ICP level. Potential explanation for these findings include that at high ICP, there is large amount of circumferential pressure to constrict the LC. Therefore, the LC had more room to stretch with increasing IOP, causing the beams to thin and pores to increase in size with IOP.

Interestingly, there is a region around 10-20mmHg ICP (as well as even lower), where there is relatively little change in LC microstructure with IOP. This ICP range is normal or slightly above normal in the primates based on the opening cerebrospinal fluid pressure. This may represent an optimal ICP where IOP changes have limited influence on the eye, and help explain the clinical findings of healthy subjects have higher ICP compared to glaucoma. [48] Furthermore, it is important to note that this region didn't occur at too high of an intracranial pressure, where there would be significant concern for vision loss via intracranial hypertension and papilledema.

The relative stable reaction to increased translaminar pressure difference at slight above normal ICP could also indicate that the eye is better suited for increases in intraocular pressure rather than intracranial pressures. This may be due to the exposure of the eye to frequent occasions of elevated intraocular pressure, such as from blinking, rubbing of the eyeball, and other natural causes of elevated IOP. However, as ICP rises, increases in IOP or TLPD results in much greater deformation at the level of the LC microstructure.

5.2.3.3 Model 3 – Quadratic Model

The lower AIC shown by the quadratic model, despite being more complex than the earlier models, further demonstrates that the effect of IOP and ICP on the eye are non-linear. This means that even while maintaining ICP, an increase in IOP from 10 to 30mmHg result in a different deformation change than an increase in IOP from 30 to 50mmHg.

It is promising to see that the overall trend in how LC microstructure is deformed by IOP and ICP remains unchanged in the nonlinear model compared to the interaction model. There still remains a watershed zone around an ICP of 10-20mmHg over which we see less change in LC microstructure with increasing IOP. Interestingly, pore diameter is the only LC parameter that did not improve with the addition of the quadratic model. It is possible that the pores, which has very different biomechanical properties compared to beams (pores are composed of the axons of the retinal ganglion cell as well as supporting cells), deform differently from the beams under different pressure conditions.

Finally, we would like to note that more complex models are possible. Especially ones that include material properties regarding the eye. However, more complex models will tend to lower AIC in a small population of subjects due to the large number of variables. Future work will be required to investigate specific material properties such as hysteresis, creep and elastic moduli.

5.3 SUMMARY

We demonstrate in this Aim, for the first time in vivo, that both intraocular pressure and intracranial pressure deform the LC microstructure. Furthermore, the effect of IOP and ICP on the LC microstructure is non-linear and interacts strongly with one another. It is therefore important to consider both IOP and ICP when accurate investigation of the LC response to either pressure is sought.

6.0 CHARACTERIZATION OF THE EFFECT OF GLAUCOMA ON HUMAN LAMINA CRIBROSA

In the third aim of this proposal, we are taking the tools we developed in Aim 1 and the knowledge from our animal studies in Aim 2 and to apply them in vivo to humans. Here, we seek to understand how the LC microstructure differs with glaucoma. Our goal is to assess a number of features, including (1) whether the LC microstructure changes with disease, (2) whether the path LC pores take through the LC change with disease, and (3) whether glaucoma influences the biomechanics of the LC as reflected in the LC microstructure response to acute changes in IOP.

Identification of LC microstructure parameters that is altered in the disease enables us to use the segmentation analysis to identify patients with glaucoma. Furthermore, as there exists little work characterizing how LC microstructure is altered in vivo with disease, it enables improved understanding of glaucoma pathogenesis and the resulting findings in the LC. First paragraph. The figure below is inserted so that there is an item in the sample List of Figures.

6.1 3-1: COMPARING LC MICROSTRUCTURE IN HEALTHY AND GLAUCOMATOUS EYES

The LC macrostructure has been studied extensively using both histology as well as in vivo using OCT. [24], [80], [101], [126], [127] However, little information exist about how the LC

microstructure differs between healthy and glaucoma eyes. The goal of this experiment is to establish for the first time, in vivo, the difference in LC microstructure in healthy compared to diseased eyes, as well as determining the association between LC microstructure and functional measures of ocular health. We hypothesize that subjects with glaucoma will demonstrate thicker LC beams and thinner LC pores in comparison with healthy controls as a result of tissue remodeling and axonal loss.

6.1.1 Methods

Sixty-eight eyes (19 healthy and 49 glaucomatous) of 47 subjects were scanned using swept source OCT. The LC was automatically segmented using the software described in Aim 1. The parameters analyzed were verified in the previous experiments and include: pore count, pore area, pore aspect ratio, pore diameter and beam thickness, lamina area, lamina volume and lamina volume fraction. Lamina volume was computed as the entire volume of the visible lamina and lamina area represents the maximum intensity projection of the volume in the A-scan direction. Lamina volume fraction was computed as the ratio of lamina beam volume to total lamina volume.

6.1.1.1 Statistical Analysis

Linear mixed effects models were constructed to assess the effect of age, clinical diagnostic group and disease severity, using visual field mean deviation (VF MD) as a surrogate indicator, with the LC parameters. Statistical analysis was performed using R Language and Environment for Statistical Computing program (version 2.15.1; <http://www.R-project.org>).[91] P-values < 0.05 were considered statistically significant.

6.1.2 Results

The average age of healthy and glaucoma subjects were 40.9 ± 11.3 and 70.9 ± 9.4 years, respectively. Average VF MD was -0.50 ± 0.08 dB for healthy eyes and -7.84 ± 8.75 dB for glaucomatous eyes. A sample of C-mode slices through the LC of healthy and glaucomatous eyes are shown in Figure 28A-D.

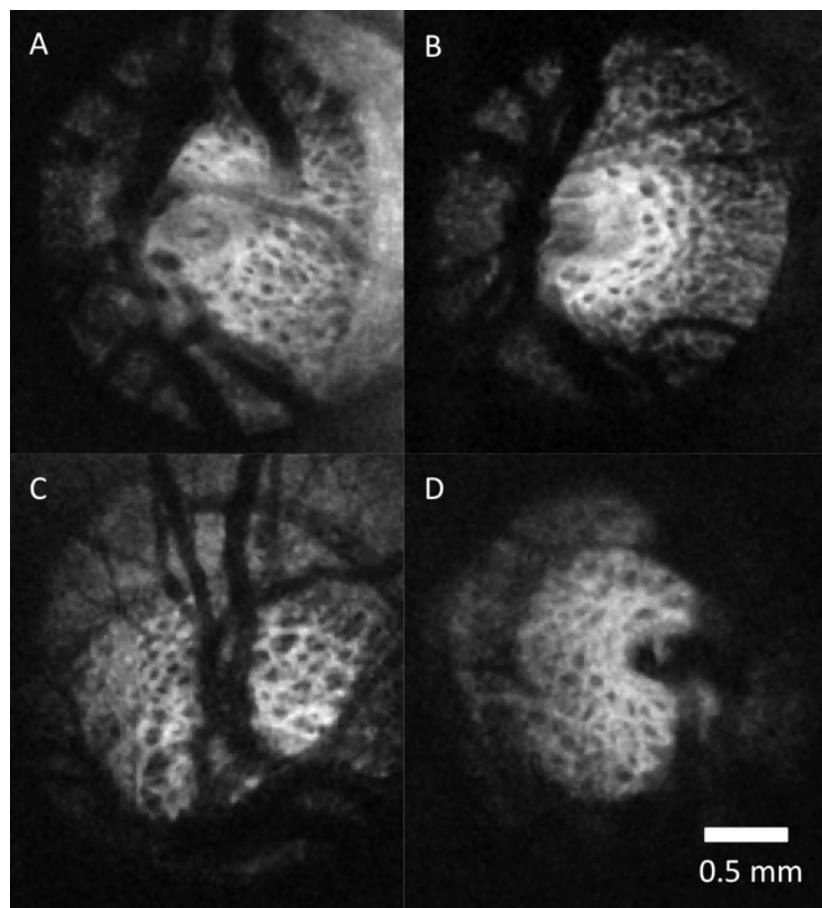


Figure 28. Lamina cribrosa C-mode of healthy (A-B) and glaucomatous (C-D) eyes. No systematic differences are subjectively apparent between healthy and glaucomatous eyes.

Differences in LC microstructure between glaucomatous and healthy eyes are not subjectively obvious. An example of a processed image of the LC in multiple levels of C-modes is shown in Figure 29A-D to illustrate the performance of the segmentation analysis in 3D.

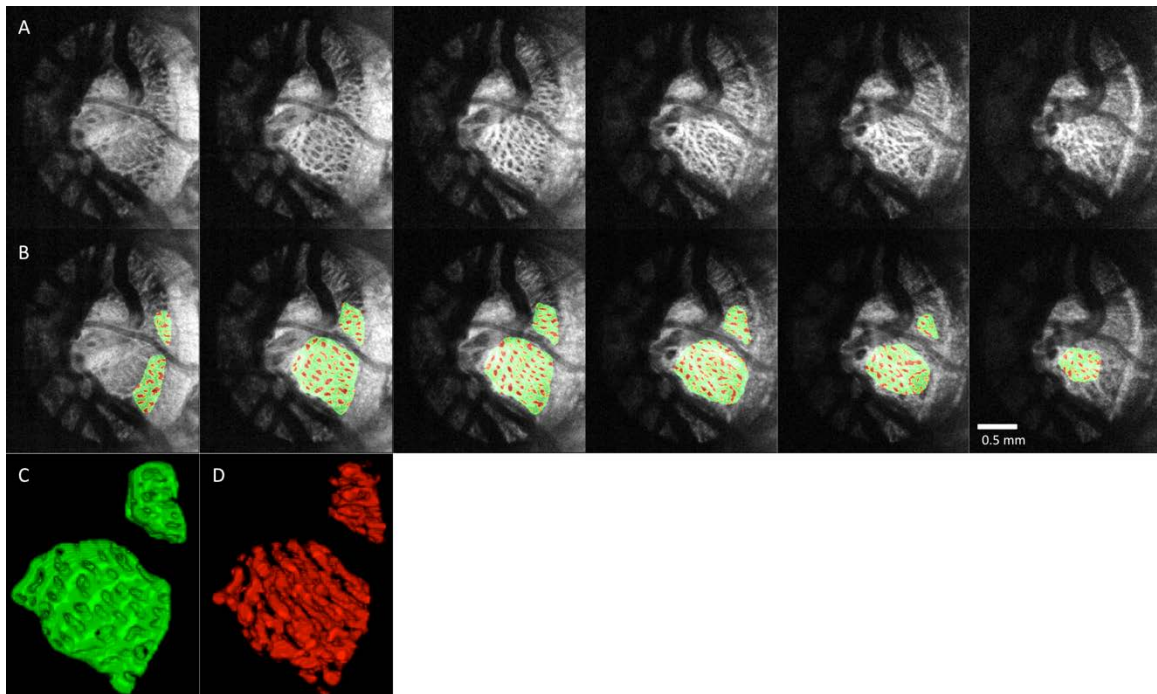


Figure 29. Segmentation examples. (A) C-mode stacks of the LC of a healthy eye stepping down 50 μm slices. (B) The same slices after segmentation with laminar beams in green and laminar pores in red. 3D reconstruction of the LC (C) beams and (D) pores.

None of the LC microstructure parameters showed statistically significant association with age. Comparing the LC microstructure parameters between healthy and glaucomatous eyes, only beam thickness to pore diameter ratio and pore diameter standard deviation were statistically significantly higher in glaucomatous eyes (Table 14). However, examining the LC microstructure as a function of VF MD demonstrated significant relationship for several parameters (Table 15). Average beam thickness, pore diameter SD and beam thickness to pore

diameter ratio increased with worsening VF MD. Average pore diameter decreased with worsening VF MD.

Table 14. Difference in LC microstructure between healthy and glaucomatous eyes. The fixed effect represents the linear mixed effect model of the difference between healthy and glaucomatous eyes. Positive fixed effect indicates an increase in the parameter with disease. Statistically significant parameters are marked with bold font.

LC Parameters	Healthy (SD)	Glaucoma (SD)	Fixed effect (95% CI)	P
Pore count	37.0 (18.8)	57.4 (24.7)	3.31 (-11.7, 18.3)	0.67
Pore density (pores/mm ²)	80.5 (23.5)	78.6 (22.5)	-3.69 (-20.0, 12.6)	0.66
Pore area (μm ²)	1970 (310)	1800 (330)	-94.9 (-312, 122)	0.40
Pore volume (mm ³)	0.0238 (0.0161)	0.0319 (0.0183)	0.010 (-0.012, 0.001)	0.90
Pore diameter average (μm)	24.6 (2.56)	22.5 (2.3)	-1.32 (-2.88, 0.25)	0.11
Pore diameter SD (μm)	0.405 (0.022)	0.433 (0.022)	0.022 (-0.008, -0.036)	<0.01
Pore aspect ratio	2.06 (0.14)	2.04 (0.11)	0.00015 (-0.076, 0.076)	0.99
Beam thickness average (μm)	46.7 (3.2)	50.0 (3.4)	1.80 (-0.38, 3.99)	0.11
Beam thickness SD (μm)	0.337 (0.013)	0.348 (0.017)	0.0095 (-0.0025, 0.022)	0.13
Beam thickness to pore diameter ratio	1.91 (0.21)	2.25 (0.31)	0.20 (0.019, 0.38)	0.04
Lamina area (mm ²)	0.684 (0.284)	1.220 (0.54)	0.53 (-0.13, 0.20)	0.24
Lamina volume (mm ³)	0.147 (0.071)	0.235 (0.124)	0.098 (-0.051, 0.023)	0.54
Lamina volume fraction	0.841 (0.055)	0.857 (0.050)	-0.0109 (-0.0256, 0.0474)	0.56

Table 15. Structure function relationship between LC microstructure and visual fields mean deviation (VF MD).

The fixed effect represents the linear mixed effect model of change per VF MD. Positive fixed effect indicates an increase in the parameter with worsening disease. Bold indicates statistically significant results.

	Fixed effect (95% confidence interval)	P-value
Pore count	1.30 (0.72, 1.89)	<0.01
Pore density (pores/mm ²)	0.429 (-0.258, 1.116)	0.22
Pore area (μm ²)	-11.8 (-22.1, 1.5)	0.03
Pore volume (mm ³)	0.000435 (-0.00005, 0.000928)	0.09
Pore diameter average (μm)	-0.0907 (-0.1648, -0.0167)	0.02
Pore diameter SD (μm)	0.000731 (0.000022, 0.001440)	0.05
Pore aspect ratio	0.000833 (-0.003104, 0.004770)	0.67
Beam thickness average (μm)	0.162 (0.056, 0.267)	<0.01
Beam thickness SD (μm)	-0.0000764 (-0.0006102, 0.0004573)	0.78
Beam thickness to pore diameter ratio	0.0182 (0.0095, 0.0266)	<0.01
Lamina area (mm ²)	0.0184 (0.0046, 0.0323)	0.01
Lamina volume (mm ³)	0.00310 (-0.00033, 0.00653)	0.08
Lamina volume fraction	-0.000250 (-0.001854, 0.001355)	0.76

6.1.3 Discussion

In this experiment, we quantify in vivo 3D LC microstructure non-invasively in healthy and glaucomatous eyes using OCT. While most published in vivo studies are limited to assessing surface features and macroscopic characteristics such as local surface abnormalities and total LC thickness, our study is the first to automatically quantify in vivo the LC microstructure in 3D.[67], [81], [128] This feature is crucial for comprehensive evaluation of glaucoma associated changes in the LC as the axons trespassing the lamina are prone to the deleterious glaucomatous effect throughout the entire LC, not just at the surface. Moreover, because the microstructure differences between glaucoma and healthy eyes are not readily apparent in a complex structure such as the LC, an automated quantification method is required in order to identify difference that may not be obvious. Using the segmentation method described in Experiment 1-1, we

identified several structural features that were significantly different between healthy and glaucomatous eyes.

6.1.3.1 Age Related Changes

We did not detect a statistically significant effect of age on the LC microstructure parameters. This is in agreement with prior histology and imaging work showing that although the LC stiffens with age [129] and increases in total thickness, [130] the microstructure are not significantly altered. [102] This is surprising since many other collagenous structures of the body, such as tendons [131], [132] and skin [133], [134] experience tremendous changes in their mechanical properties as well as ability to respond to stress as part of the aging process. However, it is important to note that this study featured a limited number of healthy eyes with suboptimal age distribution and therefore this finding require further examination in a larger cohort.

6.1.3.2 Comparing Healthy and Glaucomatous Eyes

Our results show an association between certain LC microstructure and glaucoma diagnosis (Table 14). We demonstrate a significant increase in beam thickness to pore diameter ratio in glaucoma compared to healthy eyes. While this result does not show causation as our data acquired in a cross-sectional study, it may represent LC remodeling due to the elevated IOP, creating thicker laminar beams to distribute the increased stress. Axonal loss as well as remodeling contribute to smaller LC pores, creating a change in beam thickness to pore diameter ratio with disease. We also observe a significant increase in pore diameter standard deviation in glaucomatous eyes. This may represent focal damage in glaucoma causing some pores to change in size.

In our study, we did not detect a difference in pore aspect ratio between healthy and glaucoma eyes. Previous studies report slanted pores with increased pore aspect ratio in glaucomatous eyes as assessed by fundus photography. [135] However, fundus photography only represents a projection image or the sum of all reflections along the axis of the detector. Therefore, fundus photography is not taking into account the 3D nature of the LC. Pores oriented in a diverging or converging manner would appear elongated on projection view even if they experienced no physical elongation.

6.1.3.3 Microstructure Parameters and Functional Damage

Several more parameters were statistically significant when comparing LC microstructure parameters and the continuous variable of VF MD (Table 15). The advantage of using VF MD is that we are no longer dichotomizing the study population into healthy and glaucoma. Instead, we are able to compare LC microstructure with a range of disease severity and are better able to capture significant changes. Similar to the results of the comparison between the diagnostic groups, both beam thickness to pore diameter ratio and pore diameter standard deviation were increased with more advanced disease severity (lower VF MD). This suggests that in advanced disease, more remodeling in the LC occurred, causing further beam thickening relative to pores. The increase in pore count and lamina area with advanced disease is likely due to the exposure of the lamina in enlarged cupping with larger loss of pre-laminar tissue. This likely contributed to the borderline significance in the lamina volume as well. The decrease in pore area with more severe disease reflects the shrinking pores due to axonal loss.

While the results of this experiment initially appear to contradict our findings in Experiment 2, the difference between the experiments could be explained by the chronicity of the findings. In the present study, we reported that glaucomatous eyes had thicker beams and

smaller pores compared to healthy eyes. However, Experiment 2 showed a decrease in beam thickness and an increase in pore diameter under increase in pressure. The increased beam thickness to pore diameter ratio found here likely reflect remodeling of the LC over time or even LC collapse under chronic pathologic levels of strain. Therefore, while the eyes might acutely have decreased beam thickness and increase pore size under IOP elevation, eventual remodeling and thickening of the beams to resist the pressure in the eye and the axonal loss lead to reduced pores size. These findings emphasize the importance of assessing the pressure effect on the LC both in acute and chronic models to better characterize the changes occurring in this region over the course of the disease.

6.2 EXPERIMENT 3-2: DIFFERENCES IN INDIVIDUAL LC PORE PATH BETWEEN HEALTHY AND GLAUCOMATOUS EYES

Deformation of the LC with the ensuing disturbance to the axoplasmic flow has been long suggested as the potential mechanism for glaucomatous damage leading to impaired delivery of nutrients and survival factors to retinal ganglion cell axons. [23],[136], [137] Experimental models have demonstrated an accumulation of axonal material, including mitochondria and survival factors at the level of the LC.[137], [138] However, despite its hypothesized mechanism, there have been few studies assessing how the axons travel through the LC.[139]

Characterization of individual pore paths is now possible using the segmentation analysis developed in previous experiments. The next step in utilizing this technique is to use the 3D quantification to trace individual pores and to characterize how they traverse the LC. The

purpose of this experiment was to investigate in vivo the hypothesis that the axons of glaucomatous eyes take a more tortuous path through the LC compared to healthy eyes.

6.2.1 Methods

72 subjects (10 healthy, 23 glaucoma suspect, 48 glaucoma eyes) were recruited for this study and scanned using swept source OCT and underwent visual field testing as stated under the recruitment of human subjects.

6.2.1.1 Tracking Analysis

LC pore microstructure was automatically segmented using the method described in Aim 1. The images were made isotropic ($4.065\mu\text{m}/\text{pixel}$ in all dimensions) prior to proceeding with the analysis.

Pore path was traced automatically in ImageJ using a particle tracking algorithm (MTrack2; <http://valelab.ucsf.edu/~nstuurman/ijplugins/MTrack2.html>), which allowed tracing of individual pores through the LC volume. To improve identification of pore paths from one C-mode to the next, the tracings were constrained such that pores could move a maximum of $20\mu\text{m}$ in the transverse direction between consecutive C-modes (spaced $4\mu\text{m}$ apart). This value was chosen because it is smaller than a typical pore diameter (around $25\mu\text{m}$), ensuring that adjacent pores were not selected for tracing. This value is large enough to allow some translational movement in the pores, but not enough to erroneously identify adjacent pores. Only pores that could be traced for a distance of at least $60\mu\text{m}$ in the z-direction were selected for analysis. Pore paths were subjectively assessed in 3D to ensure proper tracing (Figure 30) prior to inclusion in the analysis. The average depth of pores tracked in each eye was recorded.

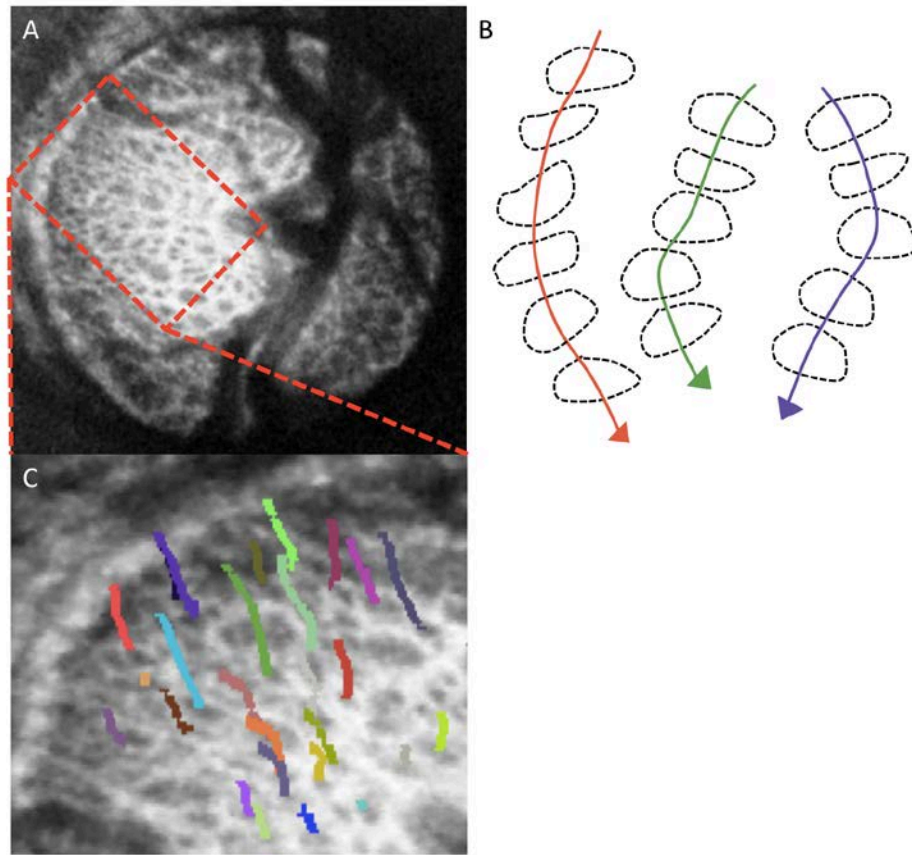


Figure 30. (A) Original C-mode view of the lamina cribrosa. Red outline represented the region that is zoomed in part (C). (B) Pore paths were traced with respect to depth via the centroid of the segmented pores. (C) 3D view of a tracing from a subset of pores (27 out of 81).

6.2.1.2 Assessment of Pore Trajectory Relative to the Disc

In order to characterize pore trajectory within the LC, we first determined the center of the optic nerve as the centroid of the Bruch membrane opening (BMO). The trajectory was defined as the distance to pore moved towards the center of the optic nerve using the method described in Figure 31. Our convention was that a positive value implies a LC pores path towards the center of the optic nerve as it traversed the LC from anterior to posterior. A negative value implies that

the pores path goes from the periphery towards the center. The change in distance was computed for each pore and averaged across all pores for a given eye. This distance was normalized based on the depth of pore path, as it was expected that pores that were traced for longer depth would have more movement in the x-y direction compare to pores that are successful traced only for a relatively short depth.

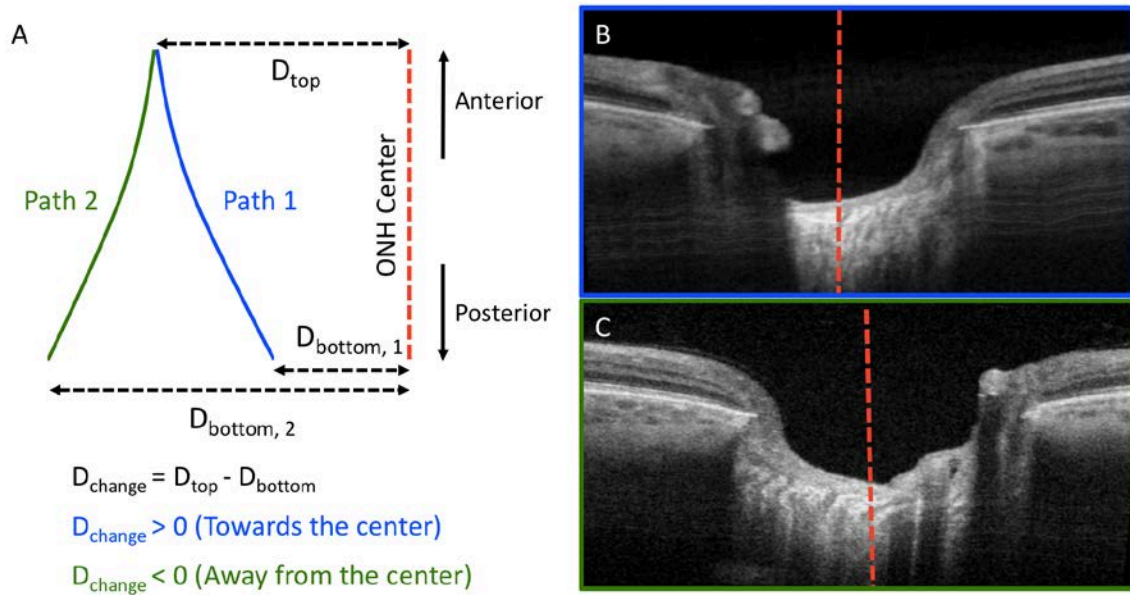


Figure 31. (A) Method of identification of pore path relative to the center of the optic nerve. Two sample paths: one moving towards the optic nerve center (path 1, blue) and was defined as a positive value and one moving away from the center (path 2, green) and defined as a negative value. (B) Example of LC identified to have pores going towards the optic nerve center (vertical red line) and (C) away from the center (vertical red line).

6.2.1.3 Assessment of Pore Tortuosity

Pore tortuosity was assessed by dividing the distance along the pore centroid path divided by the hypothetical straight path connecting the most anterior pore centroid to the most posterior pore. All tortuosity values must be 1, or greater and the larger the value the more tortuous pore path.

6.2.1.4 Statistical Analysis

A one sample Kolmogorov-Smirnov test was used to determine each eye's tortuosity distribution in order to assess the measurement distribution. A linear mixed effect analysis was used to determine 1) pore depth, 2) pore path towards the center and 3) pore tortuosity as dependent on diagnosis and VF MD. The linear mixed effect models were random intercept models, with the random effect of each eye accounting for the expected autocorrelation between eyes.

6.2.2 Results

6.2.2.1 Depth of LC Pore Path Tracking

The average depth LC pore were tracked was $157\pm 16\mu\text{m}$, $159\pm 15\mu\text{m}$ and $140\pm 14\mu\text{m}$ for healthy, glaucoma suspect and glaucoma eyes, respectively. Glaucomatous eyes had statistically significantly shorter lower depth tracked compared with healthy ($p=0.002$) and glaucoma suspects ($p<0.001$).

6.2.2.2 Pore Trajectory Relative to the Disc

Both pore path change and pore tortuosity were normally distributed. Thus, it was appropriate to average the distributions within each eye to have a summary value. Average pore paths within the LC traversed toward the ON center for a distance of $22.9\pm 2.8\mu\text{m}$ between the anterior and

posterior surfaces of analyzable LC, which was statistically significant from 0 ($p < 0.001$). Average pore path change was $87 \pm 114 \mu\text{m}$, $87 \pm 111 \mu\text{m}$, and $97 \pm 85 \mu\text{m}$ for healthy, glaucoma suspect and glaucoma eyes, respectively. We did not detect a significant difference in average LC pore path change. We did not detect a statistically significant difference amongst the diagnostic categories after normalizing by the average depth of pores traced.

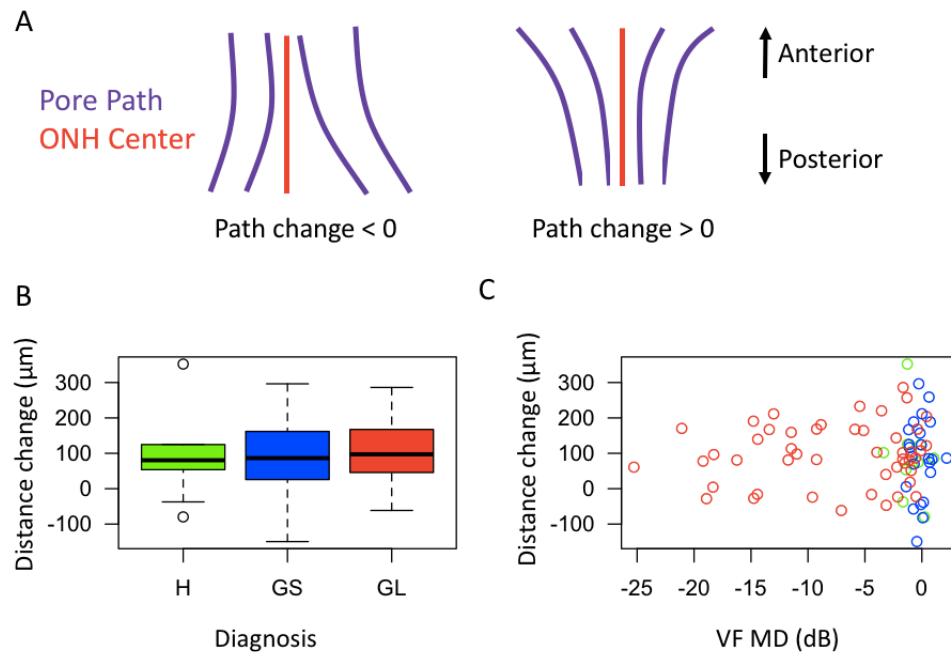


Figure 32. (A) Schematic demonstration of examples of negative path change (pores path travel away from ON center going from anterior to posterior) and positive path change (pores path travel towards the ON center). (B) Boxplot of pore path change with respect to diagnosis (H – healthy, GS – glaucoma suspect, GL – glaucomatous eyes) and (C) scatter plot of pore path change with visual field mean deviation.

6.2.2.3 Pore Tortuosity

Pore tortuosity in glaucomatous eyes (1.46 ± 0.08) was significantly higher than in healthy (1.40 ± 0.04 , $p = 0.03$) and glaucoma suspect eyes (1.39 ± 0.07 , < 0.01) (Figure 33C). Glaucomatous eyes also had larger variance compared to healthy and glaucoma suspect ($p = 0.02$, < 0.01 ,

respectively) (Figure 33D). Glaucoma severity, as determined by VF MD, did not affect the pore tortuosity (Figure 33E).

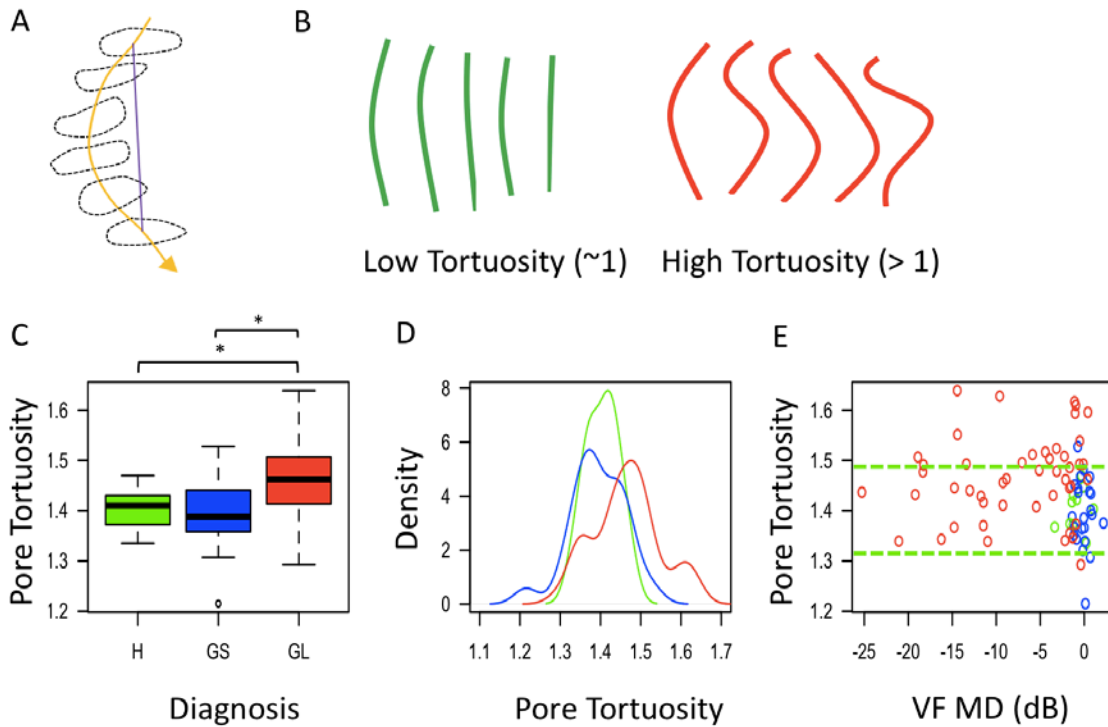


Figure 33. (A) Pore tortuosity was defined by dividing the distance traveled by the pore centroid (yellow line) by the shortest distance between the top and bottom pores (purple line). (B) Schematic showing examples of low tortuosity (green) and high tortuosity (red). (C) Boxplot of tortuosity as a function of diagnosis (H – healthy, GS – glaucoma suspect, GL – glaucomatous eyes). (D) Probability density distribution of pore tortuosity as a function of disease (Red – healthy, Blue – glaucoma suspect, Red – glaucomatous eyes). (E) Pore tortuosity as a function of visual field mean deviation, with the green lines denoting the 95% confidence interval of the healthy eyes.

6.2.3 Discussion

We demonstrate in Experiment 3-2 that glaucoma eyes have more tortuous pores compared to healthy eyes. This is a previously undescribed phenomenon, either in vivo or in histology, which

potential implications in both assessing glaucoma as well as understanding the disease. Characterization of how individual pores traverse the LC represents an examples of the type of analysis that can be completed using the tools developed in this thesis.

The ability to characterize the LC pore path in vivo in comparison with histology have several advantages and disadvantages that should be considered. While characterizing these structures in histology would allow the tracing of individual axons with depth, cryosectioning the LC could alter the microstructure and the path of the axons. Furthermore, in histology, tortuosity would be influenced by how adjacent sections are registered to one another in the 3D reconstructions, which can influence results as this is done post-hoc. OCT has the advantage of acquiring detailed 3D imaging of the LC without external perturbation that could alter the tortuosity of the microstructure. While the limited transverse resolution of conventional OCT (~15-20um) does not permit characterization of individual axons, it does allow the characterization of the path of pores which reflects the path of the axons. These pore paths can serve as a surrogate for the path of axons, as previous histology studies have demonstrated that the vast majority of axons follow their LC pore path.[139] In addition, due to the limitations of OCT technology, we can only assess visible LC microstructure that is not obstructed by blood vessel or thick prelaminar tissue. As such, interpretations of these studies must always keep these advantages and disadvantages in mind.

6.2.3.1 Depth of LC Pore Path Tracking

There are significant differences between diagnostic categories with respect to the average depth of LC pores tracked. Previous histological[24] and in vivo studies[68], [140], [141] demonstrate significantly thinner LC in glaucoma eyes, and find that thinner LC was associated with lower

visual field mean deviation. Therefore, the decreased depth tracked in our glaucomatous eyes is likely related to their clinical status. However, the depth LC pores are tracked is approximately 20% lower than the average LC thickness in other studies.[68], [141] This is probably due to the fact that while it is possible to see the posterior LC on B-scans, it is difficult to achieve adequate imaging of the posterior LC to perform segmentation on LC microstructure. Therefore, we expect that the average depth tracked to be lower than that of analyses of OCT macrostructure on individual B-scans.

6.2.3.2 Pore Trajectory

Regardless of diagnostic categories, the pore trajectory analysis demonstrate that pore path tends to converge towards the center of the optic nerve between the anterior and posterior aspects of the LC. This may be a result of bottlenecking of the retinal ganglion cell axons at the level of the optic nerve canal opening, causing the axons to converge towards the center.

We also expect that there is a difference in how much central movement is expected between healthy and glaucoma eyes. However, even after normalizing the distance traveled by the pore path towards the optic nerve center by the length of the pore path that is tracked, we did not detect a statistically significant difference between diagnostic categories.

Due to limitations of OCT, it is often not possible to image the pore path in the most posterior LC. In the posterior regions, image quality decreases such that it is difficult to determine the boundary of LC pores compared to beams. If it is possible to image deeper, we may expect that axonal paths begin to move peripherally once again as the optic nerve diameter increases due to myelination. While each eye in this study is summarized with an average pore tortuosity, more detailed analysis on how individual pore change tortuosity is possible. The characteristics of individual pores could be identified using a histogram to determine change.

6.2.3.3 Pore Tortuosity

While a number of histological studies demonstrate the blockage of axoplasmic flow at the level of the LC, [137], [138], [142] this study is the first to identify in vivo a potential mechanical reason for the blockage of flow. The increased tortuosity we observe in glaucomatous eyes may reduce axoplasmic flow and contribute to the symptoms of glaucoma. The increased tortuosity is likely a result of non-uniform strain and stress experienced by the LC, which has been identified even in models that don't consider its complex microstructure. [143] It is likely that these factors cause the axons to experience strains in different directions as the axons traverse the LC.

Our initial expectation is to find a progressive increase in tortuosity as glaucoma damage worsened. However, our results indicate that elevated tortuosity occurs at early stage of the disease (Figure 33E). It is possible that increased tortuosity is one of the first steps in glaucoma pathogenesis, which leads to axonal loss as axoplasmic flow is reduced. Being a cross-sectional study, we cannot determine the causality and additional longitudinal studies are required to elucidate whether the increase tortuosity is an early marker for disease, or even predispose patients to disease. In addition, there appears to be two categories of glaucoma eyes based on pore tortuosity, those who remained at the tortuosity level of healthy eyes (within the dashed green lines, Figure 35E) and those outside of it. Further studies are required to elucidate how these groups differ.

This experiment represents a first step towards characterizing the pore path and indirectly the axonal path within the LC. The ability to determine how the trajectory of these axons change with disease has the potential to improve our understanding of glaucoma pathogenesis, as well as improve glaucoma diagnosis.

6.3 EXPERIMENT 3-2: DIFFERENCES IN INDIVIDUAL LC PORE PATH BETWEEN HEALTHY AND GLAUCOMATOUS EYES

As we demonstrate in Aim 2 in a primate model, OCT imaging now permits the assessment of in vivo biomechanics of the LC, specifically the deformation of the LC under stress. In order to build on the knowledge gained in Aim 2, this experiment translates the findings of our animal studies to humans. This allows an understanding of how the human LC microstructure reacts to stress as well as whether LC microstructure biomechanics changes with disease. Assessing tissue biomechanics is important because changes in the mechanical properties of the LC microstructure can significantly alter the amount of force experienced by the axons passing through the LC, even with no structural changes. Furthermore, even if there exists no change in LC biomechanical response with disease, it is important to understand the distribution of strain within the LC to identify regions most likely at risk. Since astrocyte activation and remodeling due to IOP changes occur very early in the disease process [30], [118], how LC microstructure reacts to increase IOP is critical to quantify. In fact, if we are able to identify LC microstructure biomechanical responses that predisposes to damage, altered reaction of the LC microstructure has potential to serve as a marker for eyes that are especially vulnerable to pressure-related damage. We hypothesize that acute IOP elevation in humans will result in enlargement of LC pores and thinning of LC beams in humans, similar to the acute IOP elevation in primates in Aim 2. Furthermore, we expect that glaucoma eyes will experience reduced deformations compared to healthy eyes, due to the increased stiffness in their eyes.

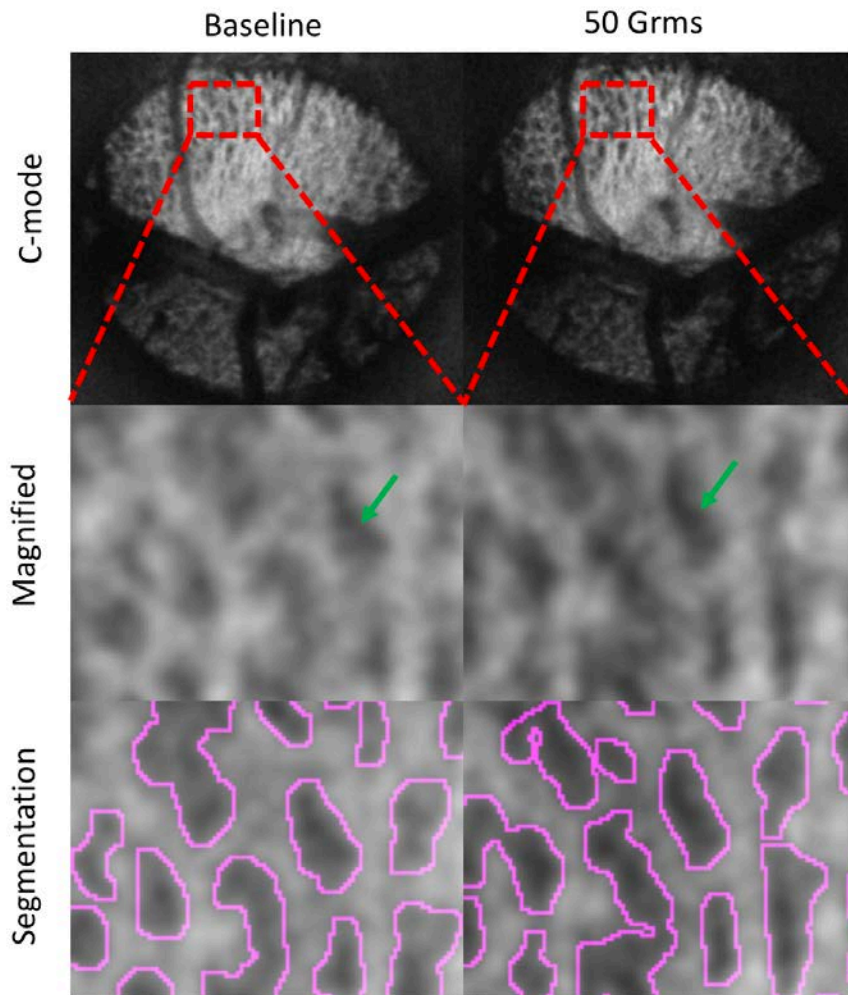


Figure 34. C-mode scans (top row) at baseline (left column) and elevated IOP (right column).

Magnification (middle row) shows changes in LC beam and pore microstructure with elevated IOP, such as altered pore size (green arrow). Segmented images (bottom row) with the automated outline overlain in purple.

6.3.1 Methods

6.3.1.1 Total Lamina Cribrosa Assessment

We enrolled 21 subjects (5 healthy, 5 glaucoma suspects, and 11 glaucoma) from the UPMC Eye Center cohort. All subjects had the same requirements as outlined in section C.1. To reduce the risk of IOP elevation, eyes with intraocular surgery within the last 6 months, as well as glaucoma

eyes with filtration surgery, were excluded from the study. One randomly selected eye per subject underwent acute IOP elevation using an ophthalmodynamometer (Figure 35) applied to the temporal sclera. The ophthalmodynamometer is a clinical tool routinely used in neuro-ophthalmic examination. The device applies a known force on the eye, measured in Grms, which is correlated with IOP, and used to be used to measure blood pressure in the central retinal artery. Swept source-OCT scans centered on the optic nerve head were acquired at (1) baseline, (2) with force equal to 30Grms (corresponds to approximately 30mmHg) applied to the eye, (3) 50Grms (corresponds to approximately 50mmHg) and (4) recovery. Based on the manufacturer's data and our own work, a baillart ophthalmodynamometer scale (Grms) of 30 and 50 Grms corresponds approximately to an IOP of 30mmHg and 50mmHg, respectively. The IOP elevation induced by the ophthalmodynamometer is confirmed by measuring IOP with the gold standard Goldmann's tonometry. The scanning pattern used is identical to the one described in Section 2.



Figure 35. Ophthalmodynamometer. The head of the device (left) is applied to the eye to elevated intraocular pressure. Adapted from Kagemann et al. [144]

Visible LC region are manually segmented for all scans: baseline, 30Grms, 50Grms and recovery. Scans without visible LC were discarded from further analysis. The scans were registered as a rigid body by aligning the BMO and then the LC microstructure, as described in Experiment 2-1 (Figure 19). Only regions of the visible LC overlapping in all pressure settings were automatically segmented and analyzed according to the protocol designed in experiment 1-1. The relative change in LC microstructure parameters were compared to baseline for all subsequent statistical analysis.

A linear mixed effect model was used to determine whether there was a difference in change in LC microstructure per IOP change between healthy, glaucoma suspect and glaucomatous eyes. Furthermore, a linear mixed effect model was used whether the change in LC microstructure per IOP change differed based on visual field mean deviation.

6.3.1.2 Individual Pore Analysis

In addition to overall analysis of changes in LC microstructure, we had also developed an automated method of matching in vivo individual LC pores under varying conditions, which was used in this project to evaluate changes in varying IOP conditions. This tool has broader application than just IOP elevation alone, as it could also be used to identify how LC pores change with time as well as with disease. In order to accomplish this, we had to identify the correct pore under baseline and IOP elevated conditions using a particle tracking algorithm (MTrack2; <http://valelab.ucsf.edu/~nsturman/ijplugins/MTrack2.html>). The following limits were implemented given the typical pores size identified in Experiment 3-1 to ensure accurate identification of pores: 1) The tracings were constrained such that pores could move a maximum of 20 μ m in the transverse direction under IOP elevation. 2) A minimum and maximum pore area change of 25% and 400%, respectively, was set to improve the performance of matching pores.

3) Finally, pores smaller than $400\mu\text{m}^2$ were excluded from subsequent analysis, as smaller pores tended to be noise or poorly matched LC pores. Examples of the matching process in one C-mode from a volume is shown in Figure 36.

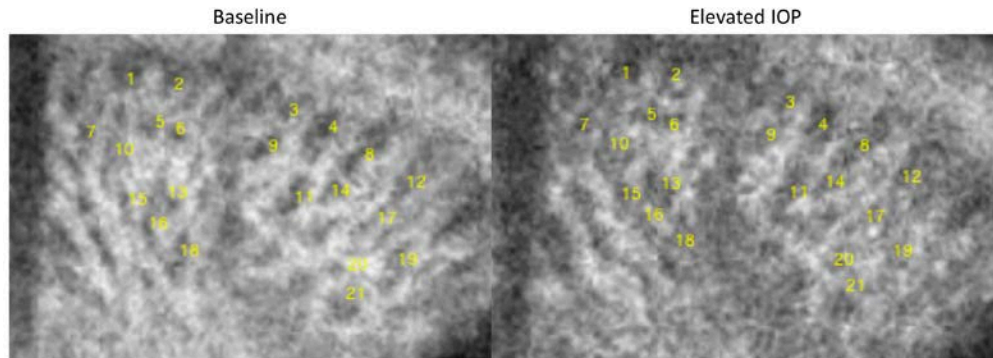


Figure 36. Automated identification of corresponding pores at baseline pressure (left) and at elevated pressure (right). The matching pores between the two scans were numbered so that they correspond to the number in the elevated IOP scan. Note that even in scans with bad quality, accurate identification of pores were achieved.

Due to the effect of noise and other potential artifacts affecting segmentation, smaller pores could experience more relative change in pore size compared to larger pores. Therefore, a model was created to simulate an increase or decrease in the pore perimeter (Figure 37). This model bases its assumption on the typical pore size and reproducibility characterized in Experiment 1-2. There, we find that the reproducibility for an average pore size of $1660\mu\text{m}^2$ is $50\mu\text{m}^2$. Assuming a round shape, this means that the typical loss of outer pixel boundary is approximately $1/3$ of a pixel radius. Therefore, the theoretical bound of change was assumed to be either an entire pixel perimeter more or less from the baseline area. The percentage of pores exceeding this limit was assessed to determine the change under IOP elevation.

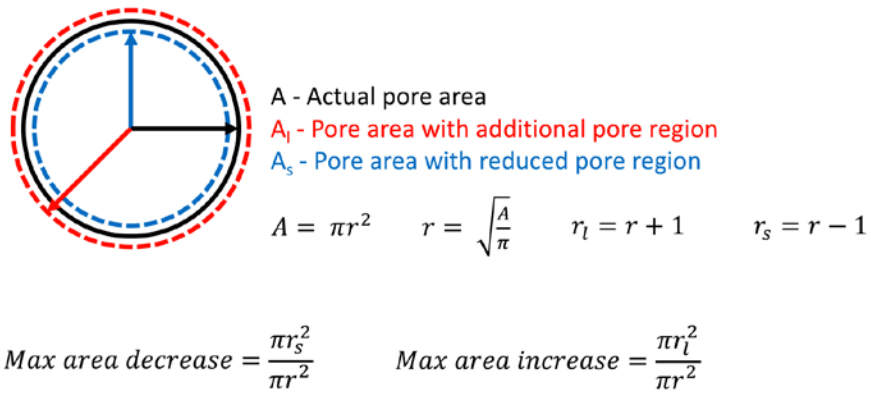


Figure 37. Method for determining range of maximum and minimum pore size change due to chance. The actual pore size (black circle) is allowed to increase (red circle) or decrease (blue circle) in size 1 full pixel thickness all the way around the pore. This full thickness increase is significantly larger than the imprecision of the measurement. This is used to create a boundary beyond which pore size change is unlikely to have occurred due to chance.

The pore area change was defined by the pore area under IOP elevation divided by pore area at baseline. This value was then converted to binary logarithm (log₂) for the purpose of setting doubling in pore area equivalent to halving pore area in term of area change. All subsequent analysis using change in pore area use the log₂ change, where 0 indicates no change, positive values indicate increase in area and negative value indicate decrease in area (Figure 40). When assessing average pore area change, the log₂ change was average before being unlogged to get an average percentage change in area.

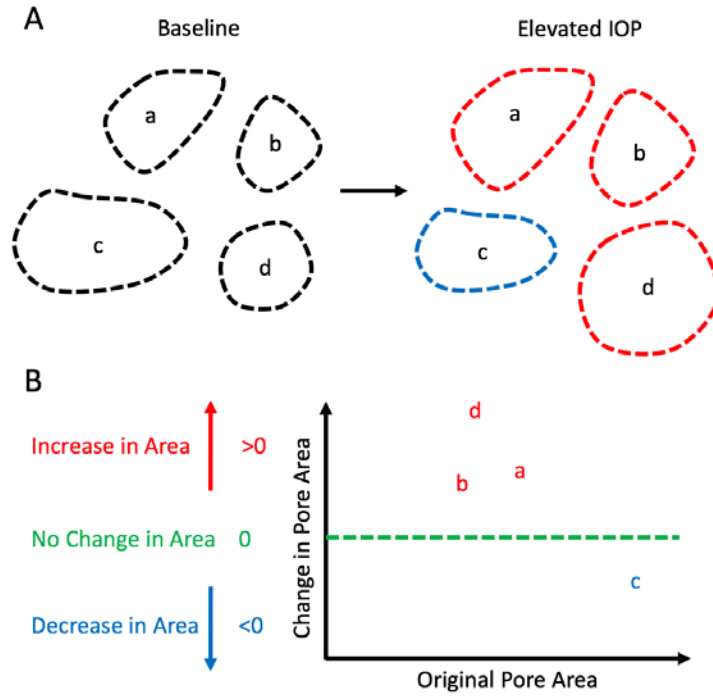


Figure 38. Assessment of individual pore area change. (A) Examples of a series of pores at baseline (left) and under elevated IOP (right). Pores that increase in size was colored red, while pores that decreased in size in blue. (B) Plot of how change in pore area was dependent on the original pore area. Green represents no change in pore area, which results in a log base 2 change of 0.

In a subset of 6 eyes, a single C-mode from the matched volumes were selected and manual traced to identify the matching pore sets. The manual tracing was considered as gold standard and the sensitivity and specificity of the automated selection process was quantified by comparing to the manual tracing.

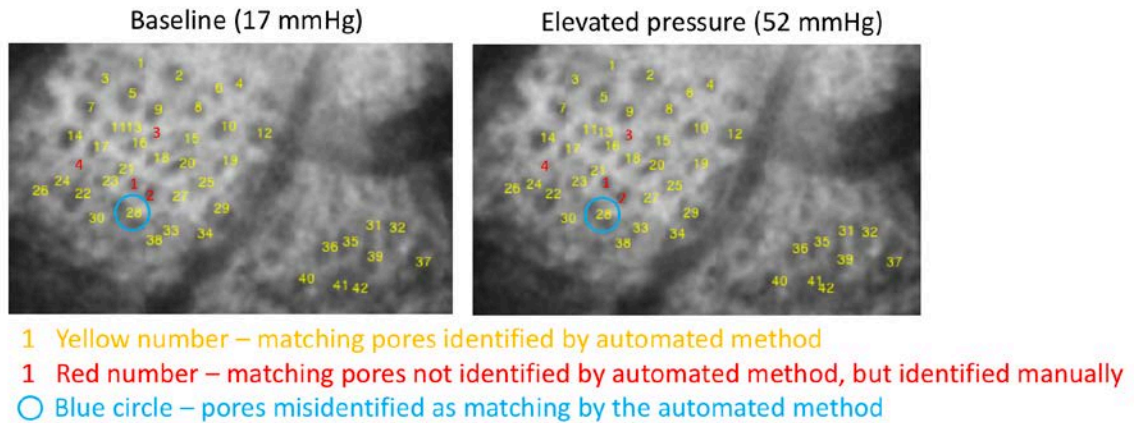


Figure 39. One LC C-mode (out of 61) under two pressure conditions showing the identification of individual LC pores at baseline and with elevated pressure. Matching pores are identified by individual number.

Areas near blood vessels and with poor visibility were excluded from analysis.

6.3.2 Results

We scanned a total of healthy and glaucoma eyes. Average age of healthy, glaucoma suspect and glaucoma patient is 28.5 ± 11.6 , 54.1 ± 12.2 , and 59.0 ± 11.6 years, respectively. Average visual field mean deviation was -1.1 ± 1.4 , -1.3 ± 1.2 , and -1.0 ± 1.9 dB, respectively. Average IOP at 30 Grms was 32.0 ± 3.5 mmHg and 50 Grms was 48.7 ± 6.4 mmHg.

6.3.2.1 Total Lamina Cribrosa Assessment

IOP elevation to 30Grms induced an average beam thickness, pore diameter, and beam thickness to pore diameter ratio change from baseline of -0.14 ± 5.80 , -0.77 ± 4.61 and $0.85 \pm 7.41\%$, respectively. IOP elevation to 50Grms induced an average beam thickness, pore diameter, and beam thickness to pore diameter ratio change from baseline of $-0.02 \pm 8.30\%$, $-3.91 \pm 6.94\%$ and $-0.49 \pm 4.11\%$, respectively. The microstructural response to pressure modulation divided by the

clinical diagnostic groups is presented in Figure 40. No statistically significant difference was detected amongst the diagnostic categories in the LC microstructure response to 30 Grms or 50 Grms. Considering the wide variability in the diagnostic categories, it was unlikely additional patients would have resulted in statistically significant difference amongst the groups.

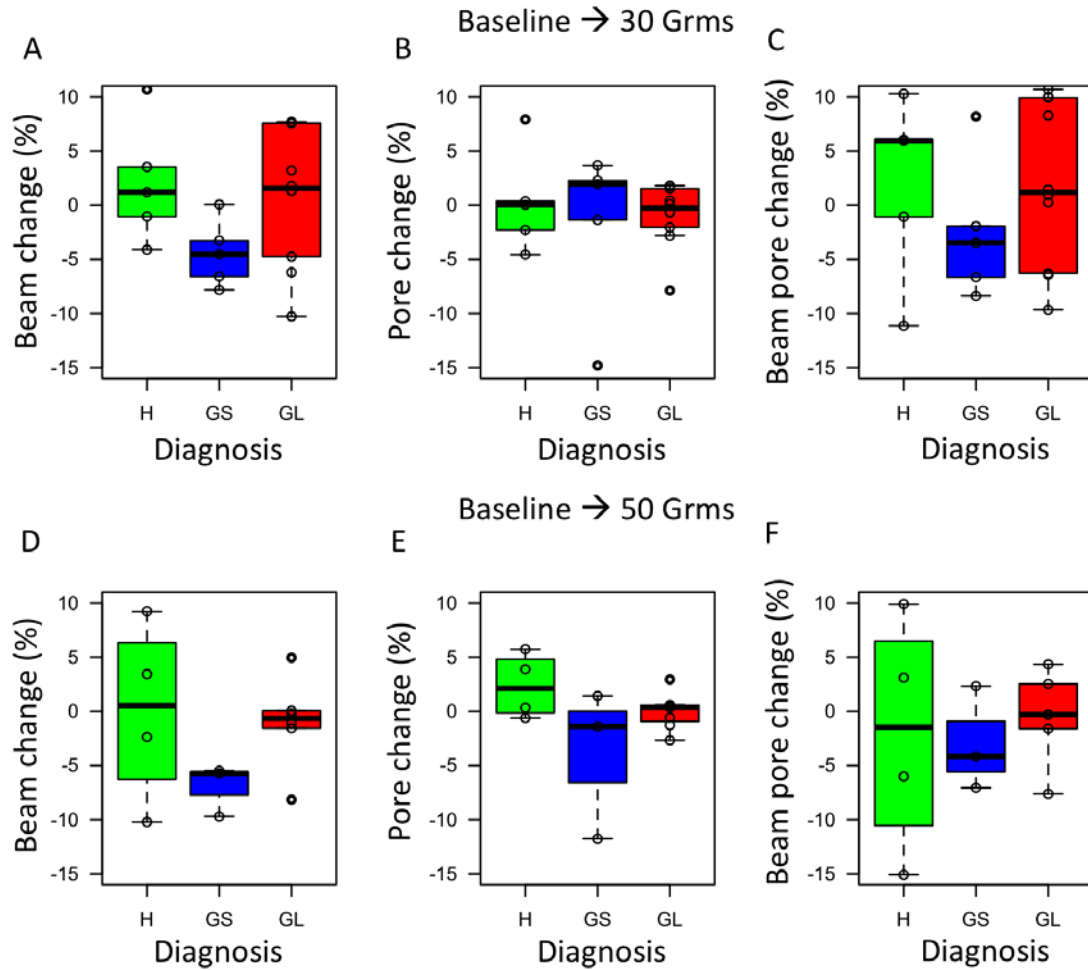


Figure 40. Boxplots of (A) beam thickness, (B) pore diameter and (C) beam thickness to pore diameter ratio changes between baseline to 30 Grms. Changes from baseline to 50 Grms are presented in D – F.

There was a statistically significant correlation between the change in LC microstructure at 30 Grms and 50 Grms (Figure 40). It showed a linear trend with $p < 0.001$ for all three parameters.

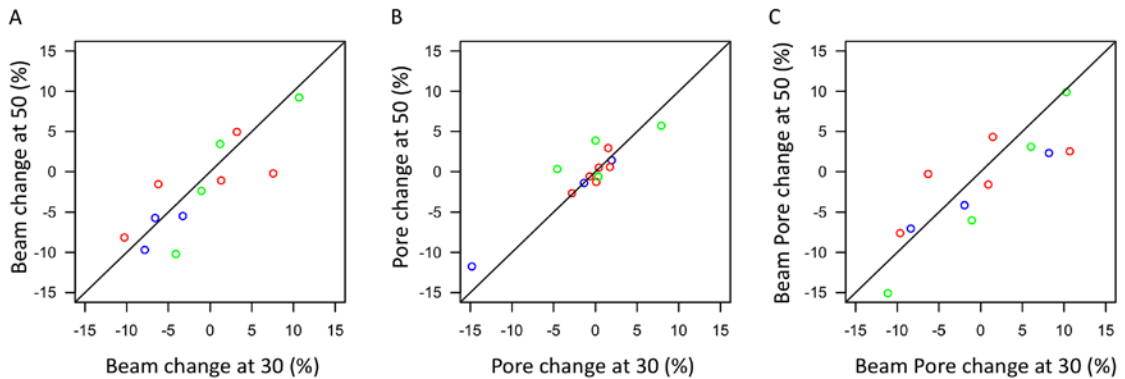


Figure 41. Scatterplot of (A) beam thickness, (B) pore diameter and (C) beam thickness to pore diameter ratio change under a force of 30 Grms compare to the change under at a force of 50 Grms. Black line is the equality line. Green – healthy, blue – glaucoma suspects, red – glaucoma.

6.3.2.2 Individual Pore Analysis

The sensitivity and specificity of identifying matching pores across pressure conditions, using the manual matching as the gold standard, was $97.7 \pm 2.3\%$ and $84.9 \pm 6.1\%$, respectively.

There were significant variations within a given eye in individual pores response to pressure modulation with some pores becoming larger while other becoming smaller. At elevated IOP, average change in individual pore area was $9.3 \pm 3.0\%$, $12.1 \pm 4.0\%$ and $1.3 \pm 4.8\%$ for healthy, glaucoma suspect, and glaucoma eyes, respectively (Figure 45). The change in glaucomatous eyes was significantly smaller compared with both healthy and glaucoma suspects (both $p < 0.01$).

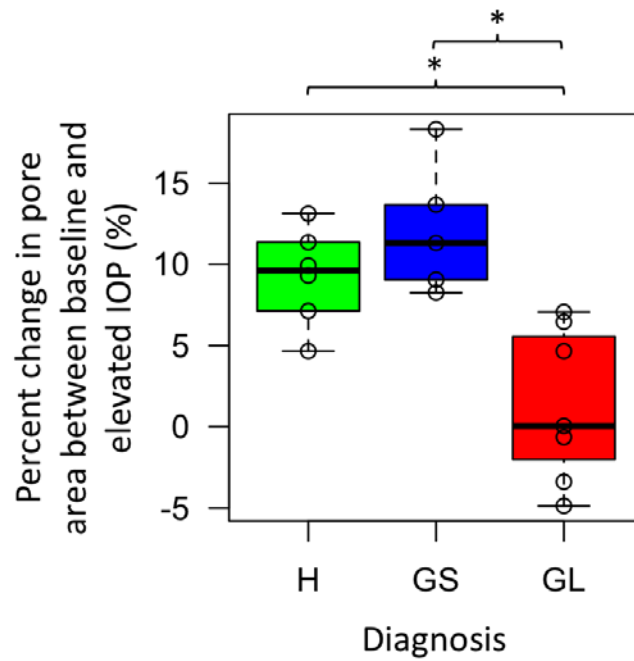


Figure 42. Boxplot of percent change in pore area under IOP elevation between the diagnostic categories.

H – healthy, GS – glaucoma suspect, GL – glaucoma.

When assessing pore area change, it was noted that the change was dependent on the initial area. Smaller pores experienced more relative change in pore size compared to larger pores. However, there were no difference in absolute pore size change as pore area increased. (Figure 43)

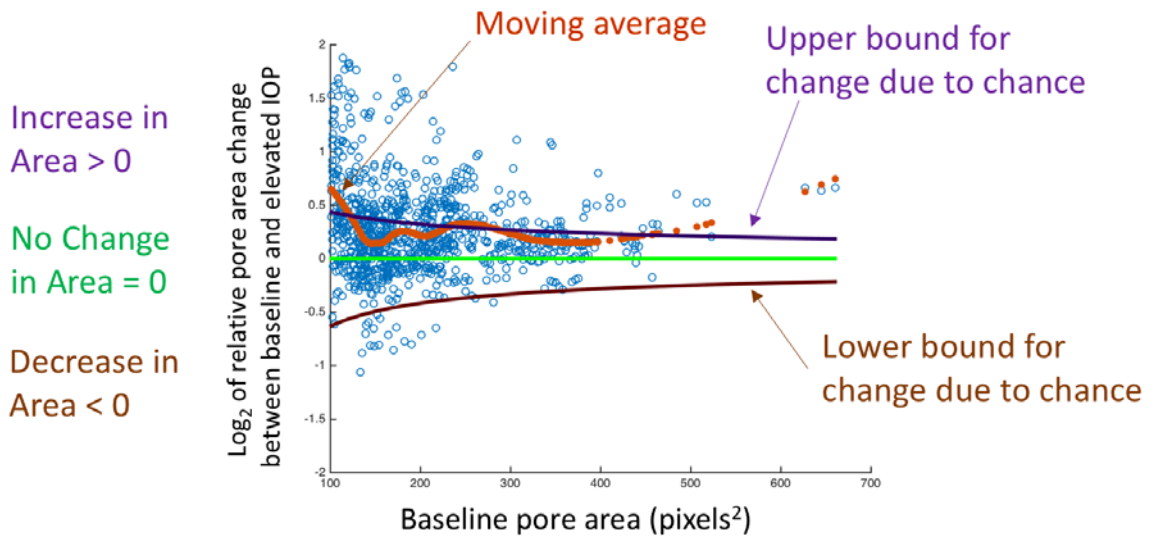


Figure 43. Individual LC pores change as a function of pore area at baseline with most changes occurring in smaller pores and the moving average is consistently above zero.

6.3.3 Discussion

This study represents the first in vivo assessment of LC microstructure biomechanical response in human eyes. As seen in this final study, there is significant variations in how certain individuals react to change in IOP. We cannot detect a significant difference in how the total LC microstructure change with respect to diagnostic categories. However, by matching pores at baseline and under elevated IOP, we are able to identify that pore area generally increase, with the increase being significantly more prominent in healthy eyes compared to glaucoma eyes. These findings emphasize the importance of individualized biomechanical testing of the LC, especially on a pore by pore level, as significant heterogeneity exists within diagnostics categories, as well as eyes.

6.3.3.1 Total Lamina Cribrosa Assessment

We did not detect a difference in the acute LC microstructure response of glaucomatous eyes compared with healthy eyes. Our initial expectation was that glaucomatous eyes would experience a decrease in beam thickness and increase in pore diameter, with the eye being stretched by the elevated IOP. However, it was clear that there were a number of both healthy and glaucoma eyes whose beams thickened and pores decreased in diameter in response to IOP elevation. Furthermore, it is important to note that the assessment represents an overall assessment, which is based on averaging all the beam and pore changes. This may average out localized changes, which are expected to occur in any complex 3D biomechanical structure. Thus, it is especially important to begin to develop and utilize tools that can identify localized changes, such as the individual pore analysis described here.

We demonstrated that the trend of microstructure changes occurring at 30 Grms is similar to the trend occurring at 50 Grms. This finding suggest that the vast majority of the changes occurred between baseline to 30 Grms. It may be a result of collagen fibers being almost fully stretched at 30 Grms, with relatively small changes beyond this level. These results are in agreement with pervious study showing that the ONH surface deforms similarly at 30 mmHg and 50 mmHg. [50] However, our study is the first to demonstrate the effect on LC microstructure in vivo.

Finally, there were no significant correlations between global LC microstructure deformation and various glaucoma parameters (visual field mean deviation, retinal nerve fiber layer thickness, central corneal thickness and IOP). We had expected to find a relationship with respect to central corneal thickness [145], which has been associated with optic nerve size, and age, which is known to cause changes in collagen. [146] However, the lack of association

between central corneal thickness and LC microstructure change may reflect that the biomechanics of the optic nerve is complex and depend on additional factors beside the collagen.

6.3.3.2 Individual Pore Analysis

In order to alleviate one of the main limitations of the global LC analysis, we developed an automated method of matching in vivo individual LC pores under varying conditions. We used this method to analyze the individual pore deformations in response to IOP modulation. Previous study used deformable registration to identify change under pressure, [147] but it does not have the ability to identify and trace individual pores changes. Our study is the first in vivo analysis of individual pores change under pressure modulation. We would like to emphasize that as we move forward, it will be increasingly important to use these type of localized analysis, as glaucoma damage is typically localized to certain locations. Furthermore, this method can be useful for assessing changes in individual pores as part of aging, along the course of glaucoma, etc.

The individual pore matching demonstrated excellent performance in identifying matching pores under IOP elevation, with high sensitivity (98%). Although the specificity is lower (85%), it is important to remember that this parameter is less of a concern in these studies. While we would ideally like to identify all matching pores, it is far better to identify fewer accurately matching pores, rather than a large number of non-matching pores. Non-matching pores could significantly skew the data, especially with large variations in pore size (if a large pore was mistakenly paired with a small pore).

In the study, we reported that LC pores of glaucoma eyes deformed less than those of healthy eyes. The reduced deformation in the glaucoma indicates that those eyes are stiffer than those of healthy eyes. This may be due to intrinsic damage caused by glaucoma, repeated exposure to periods of elevated IOP causing remodeling to stiffen the beams. Yet, our glaucoma

group was substantially older than our healthy group which might exaggerate the reduction in in deformation as it has been shown that aging causes stiffening the LC. [133], [146]

The finding of smaller pores experiencing more change in area than larger pores under IOP elevation has a number of ramifications. Assuming that large distortions and strains have deleterious effect on axons, our results indicate that smaller pores are at higher risk of causing damage compared to larger pores. The functional implication of this finding should be tested in future longitudinal studies.

6.4 SUMMARY

We have identified in this Aim that there are significant differences in LC microstructure between healthy and glaucomatous eyes, with the later having thicker beams and smaller pores compared with healthy eyes. The finding of increase tortuosity in the eyes of glaucoma eyes is especially intriguing. This may represent a mechanical change in the path of the axons that is prone to the obstruction of axoplasmic flow. Further investigation into these finding could potentially identify as a very early manifestation of glaucoma damage, before permanent damage has already occurred. Finally, we have demonstrated the first finding of in vivo differences in the biomechanics of LC microstructure between healthy and glaucoma only captured when evaluating the effect on individual pore level.

7.0 DISSERTATION SYNOPSIS

This thesis represents the first in vivo assessment of 3D LC microstructure, demonstrating findings that would not be possible without modern day OCT imaging. These experiments have established that a novel automated assessment of the LC microstructure is feasible and demonstrate its use in assessment of glaucoma as well as improving our understanding of glaucoma pathogenesis.

In Aim 1, we demonstrate the feasibility of using automated segmentation to analyze the LC. After developing the automated LC segmentation tool, we find that the automated segmentation performed similar to that of manual human controls. The segmentation algorithm is also highly reproducible, with an imprecision between scans of the less than 5% across the board.

In Aim 2, we utilize the segmentation tools developed in Aim 1 to identify LC microstructure deformation in response to alterations in both IOP and ICP. We demonstrate significant interactions between the two, indicating that both pressures should be considered for accurate evaluation of LC microstructure response to pressure. Furthermore, the experiments indicate the importance of considering both IOP and ICP for thorough evaluation of glaucoma.

In Aim 3, we use the lessons gleaned from our animal model to identify changes in LC microstructure in humans. We identify differences in LC microstructure in glaucomatous eyes compared to healthy. Glaucomatous eyes have larger beam thickness and smaller pores, likely a

result of remodeling and axonal loss. These results are the opposite of what is seen under acute pressure elevation, likely reflecting the difference between acute and chronic effects. Furthermore, we demonstrate that pores of glaucoma eyes were more tortuous compared to healthy eyes, providing a potential mechanism for blockage of axoplasmic flow at the level of the LC. Finally, we identify that there was significant difference in the response to an increase in IOP at the individual pore level between healthy and glaucomatous eyes, and that smaller pores are specifically prone to larger changes compared to larger pores.

7.1 LIMITATIONS

While LC microstructure analysis has the potential to significantly improve our understanding of glaucoma, there are technical limitations that must be considered when interpreting the results of our experiments as well as future assessments of LC microstructure. Furthermore, there remains significant hurdles to be overcome before LC microstructure analysis can be implemented in the clinical setting.

A main limitation of this study, similar to most other *in vivo* imaging studies analyzing the LC, is related to the ability to capture the entire LC, which is highly dependent on the characteristics of the blood vessels and prelaminar tissue overlying the LC. This inevitable limitation is related to the complex structure of the optic nerve head region and the physical properties of the OCT technology. Due to the vascular pattern at the optic nerve, the region best visualized is the temporal LC, with less analyzable LC in other regions. Despite the temporal region being less sensitive to glaucomatous damage than superior or inferior regions, [148] our study still has sufficient power to demonstrate significant changes in the LC of glaucomatous

eyes compared to healthy eyes. OCT development to improve our ability to visualize larger regions of the LC would enhance the utility of LC microstructure assessment.

While our experiments in primates and humans demonstrate significant changes in LC microstructure with IOP and ICP, it is important to remember that these are acute changes only. Considering that glaucoma is a chronic progressive disease, the acute experiments create the foundation for future projects that would assess the chronic effect where apoptosis and remodeling has an important role. Comparing the acute and chronic effects will allow us to determine the contribution of these biological factors to the disease process.

7.2 FUTURE WORK

This thesis represents a first step towards both assessing the LC microstructure clinically, as well as understanding how LC microstructure is altered in glaucoma. Given the novelty of the technique, there exists a number of potential avenues for investigation of the LC microstructure. One of main limitations of the present technique is the requirement of having clearly visible LC microstructure. In doing so, we are limited to only regions without thick prelaminar tissue or vessel covering the anterior LC. Future work may incorporate compensation techniques to improve contrast in regions of low signal to noise. [149] This may enable the visualization of structure previously unseen and less visible regions and permit a more compressive analysis of LC microstructure.

As glaucoma is a slowly progression chronic disease, it is critical to identify how the LC is remodeling after modifying both IOP and ICP. Specifically, it is important to identify whether IOP over time will result in thickening of the beams due to remodeling to sustain the IOP.

While both Aim 3 feature experiments assessing individual LC pores changes with IOP modulation, it is critical to not limit ourselves only to this analysis. Assessment of how individual pores change is especially promising for longitudinal studies, where we can identify how certain LC pores change and remodel over time. It will provide information on aging effects on the LC, to help differentiate glaucoma damage from age-related changes. It will be especially interesting to follow the progression of LC pore change, as well as progression of glaucoma. For example, we could answer whether there exists specific LC microstructure features that more predisposes a patient to progression, allowing us to identify patients especially prone to disease.

7.3 CONCLUSION

We have developed a novel method for in vivo automated assessment of LC microstructure. In doing so, we have identified that it is critical consider both IOP and ICP when assessing the LC microstructure, as they both deform the LC, with significant interaction between them. Furthermore, we have identified a number of LC microstructure differences in healthy and glaucomatous eyes, which may reflect axonal loss as well as remodeling with disease. The assessment of LC microstructure using OCT holds great promise for both glaucoma diagnosis and improving our understanding of disease pathogenesis.

BIBLIOGRAPHY

- [1] H. A. Quigley, “Number of people with glaucoma worldwide,,” Br. J. Ophthalmol., vol. 80, no. 5, pp. 389–393, May 1996.
- [2] H. A. Quigley and A. T. Broman, “The number of people with glaucoma worldwide in 2010 and 2020,,” Br. J. Ophthalmol., vol. 90, no. 3, pp. 262–267, Mar. 2006.
- [3] C. F. Burgoyne, “A biomechanical paradigm for axonal insult within the optic nerve head in aging and glaucoma,,” Exp. Eye Res., vol. 93, no. 2, pp. 120–132, Aug. 2011.
- [4] J. Albon, P. P. Purslow, W. S. S. Karwatowski, and D. L. Easty, “Age related compliance of the lamina cribrosa in human eyes,,” Br. J. Ophthalmol., vol. 84, no. 3, pp. 318–323, Mar. 2000.
- [5] Eye Diseases Prevalence Research Group, “Prevalence of open-angle glaucoma among adults in the United States,,” Arch. Ophthalmol., vol. 122, no. 4, p. 532, 2004.
- [6] W. Mackenzie, *A Practical Treatise on the Diseases of the Eye*. Longman, Brown, Green & Longmans, 1854.
- [7] E. M. Van Buskirk and G. A. Cioffi, “Glaucomatous Optic Neuropathy,,” Am. J. Ophthalmol., vol. 113, no. 4, pp. 447–452, Apr. 1992.
- [8] H. A. Quigley, “Open-angle glaucoma,,” N. Engl. J. Med., vol. 328, no. 15, pp. 1097–1106, 1993.
- [9] Y. H. Kwon, J. H. Fingert, M. H. Kuehn, and W. L. M. Alward, “Primary Open-Angle Glaucoma,,” N. Engl. J. Med., vol. 360, no. 11, pp. 1113–1124, Mar. 2009.
- [10] G. A. Cioffi, F. J. Durcan, C. A. Girkin, and others, “Basic and Clinical Science Course (BCSC) Section 10: Glaucoma,,” San Franc. CA Am. Acad. Ophthalmol., vol. 7, 2008.
- [11] B. T. Gabelt and P. L. Kaufman, “Changes in aqueous humor dynamics with age and glaucoma,,” Prog. Retin. Eye Res., vol. 24, no. 5, pp. 612–637, 2005.
- [12] J. Gottanka, D. H. Johnson, P. Martus, and E. Lütjen-Drecoll, “Severity of optic nerve damage in eyes with POAG is correlated with changes in the trabecular meshwork,,” J. Glaucoma, vol. 6, no. 2, pp. 123–132, 1997.

- [13] J. Alvarado, C. Murphy, and R. Juster, "Trabecular Meshwork Cellularity in Primary Open-angle Glaucoma and Nonglaucomatous Normals," *Ophthalmology*, vol. 91, no. 6, pp. 564–579, Jun. 1984.
- [14] N. G. Congdon, Q. Youlin, H. Quigley, P. T. Hung, T. H. Wang, T. C. Ho, and J. M. Tielsch, "Biometry and Primary Angle-closure Glaucoma among Chinese, White, and Black Populations," *Ophthalmology*, vol. 104, no. 9, pp. 1489–1495, Sep. 1997.
- [15] N. Gupta, L.-C. Ang, L. N. de Tilly, L. Bidaisee, and Y. H. Yücel, "Human glaucoma and neural degeneration in intracranial optic nerve, lateral geniculate nucleus, and visual cortex," *Br. J. Ophthalmol.*, vol. 90, no. 6, pp. 674–678, 2006.
- [16] H. A. Quigley, "Neuronal death in glaucoma," *Prog. Retin. Eye Res.*, vol. 18, no. 1, pp. 39–57, Jan. 1999.
- [17] C. F. Burgoyne, J. Crawford Downs, A. J. Bellezza, J.-K. Francis Suh, and R. T. Hart, "The optic nerve head as a biomechanical structure: a new paradigm for understanding the role of IOP-related stress and strain in the pathophysiology of glaucomatous optic nerve head damage," *Prog. Retin. Eye Res.*, vol. 24, no. 1, pp. 39–73, Jan. 2005.
- [18] J. Crawford Downs, M. D. Roberts, and I. A. Sigal, "Glaucomatous cupping of the lamina cribrosa: A review of the evidence for active progressive remodeling as a mechanism," *Exp. Eye Res.*, vol. 93, no. 2, pp. 133–140, Aug. 2011.
- [19] M. Ds, B. Ah, and J. Gw, "Orthograde and retrograde axoplasmic transport during acute ocular hypertension in the monkey.," *Invest. Ophthalmol. Vis. Sci.*, vol. 16, no. 5, pp. 426–441, May 1977.
- [20] G. D, T. T, and K. T, "Axoplasmic flow during chronic experimental glaucoma. 1. Light and electron microscopic studies of the monkey optic nervehead during development of glaucomatous cupping.," *Invest. Ophthalmol. Vis. Sci.*, vol. 17, no. 9, pp. 838–846, Sep. 1978.
- [21] M. Salinas-Navarro, L. Alarcón-Martínez, F. J. Valiente-Soriano, M. Jiménez-López, S. Mayor-Torroglosa, M. Avilés-Trigueros, M. P. Villegas-Pérez, and M. Vidal-Sanz, "Ocular hypertension impairs optic nerve axonal transport leading to progressive retinal ganglion cell degeneration," *Exp. Eye Res.*, vol. 90, no. 1, pp. 168–183, Jan. 2010.
- [22] C. Balaratnasingam, W. H. Morgan, L. Bass, G. Matich, S. J. Cringle, and D.-Y. Yu, "Axonal Transport and Cytoskeletal Changes in the Lamellar Regions after Elevated Intraocular Pressure," *Invest. Ophthalmol. Vis. Sci.*, vol. 48, no. 8, pp. 3632–3644, Aug. 2007.
- [23] H. A. Quigley, S. J. McKinnon, D. J. Zack, M. E. Pease, L. A. Kerrigan–Baumrind, D. F. Kerrigan, and R. S. Mitchell, "Retrograde axonal transport of BDNF in retinal ganglion cells is blocked by acute IOP elevation in rats," *Invest. Ophthalmol. Vis. Sci.*, vol. 41, no. 11, pp. 3460–3466, 2000.

- [24] H. A. Quigley, R. M. Hohman, E. M. Addicks, R. W. Massof, and W. R. Green, "Morphologic changes in the lamina cribrosa correlated with neural loss in open-angle glaucoma.," *Am. J. Ophthalmol.*, vol. 95, no. 5, p. 673, 1983.
- [25] M. Wilczek, "The lamina cribrosa and its nature," *Br. J. Ophthalmol.*, vol. 31, no. 9, pp. 551–565, Sep. 1947.
- [26] K. M. Miller and H. A. Quigley, "The clinical appearance of the lamina cribrosa as a function of the extent of glaucomatous optic nerve damage," *Ophthalmology*, vol. 95, no. 1, pp. 135–138, Jan. 1988.
- [27] H. A. Quigley and E. M. Addicks, "Regional differences in the structure of the lamina cribrosa and their relation to glaucomatous optic nerve damage.," *Arch. Ophthalmol.*, vol. 99, no. 1, pp. 137–143, 1981.
- [28] M. D. Roberts, V. Grau, J. Grimm, J. Reynaud, A. J. Bellezza, C. F. Burgoyne, and J. C. Downs, "Remodeling of the Connective Tissue Microarchitecture of the Lamina Cribrosa in Early Experimental Glaucoma," *Invest. Ophthalmol. Vis. Sci.*, vol. 50, no. 2, pp. 681–690, Feb. 2009.
- [29] H. Yang, G. Williams, J. C. Downs, I. A. Sigal, M. D. Roberts, H. Thompson, and C. F. Burgoyne, "Posterior (Outward) Migration of the Lamina Cribrosa and Early Cupping in Monkey Experimental Glaucoma," *Invest. Ophthalmol. Vis. Sci.*, vol. 52, no. 10, pp. 7109–7121, Sep. 2011.
- [30] M. R. Hernandez, "The optic nerve head in glaucoma: role of astrocytes in tissue remodeling," *Prog. Retin. Eye Res.*, vol. 19, no. 3, pp. 297–321, May 2000.
- [31] D. R. Anderson, S. M. Drance, M. Schulzer, and others, "Natural history of normal-tension glaucoma.," *Ophthalmology*, vol. 108, no. 2, p. 247, 2001.
- [32] M. O. Gordon, M. A. Kass, and for the Ocular Hypertension Treatment Study Group, "The Ocular Hypertension Treatment Study: Design and Baseline Description of the Participants," *Arch Ophthalmol*, vol. 117, no. 5, pp. 573–583, May 1999.
- [33] A. Sommer, J. M. Tielsch, J. Katz, H. A. Quigley, J. D. Gottsch, J. Javitt, and K. Singh, "Relationship between intraocular pressure and primary open angle glaucoma among white and black Americans: the Baltimore Eye Survey," *Arch. Ophthalmol.*, vol. 109, no. 8, pp. 1090–1095, 1991.
- [34] P. Mitchell, W. Smith, K. Attebo, and P. R. Healey, "Prevalence of Open-angle Glaucoma in Australia: The Blue Mountains Eye Study," *Ophthalmology*, vol. 103, no. 10, pp. 1661–1669, Oct. 1996.
- [35] A. Iwase, Y. Suzuki, M. Araie, T. Yamamoto, H. Abe, S. Shirato, Y. Kuwayama, H. K. Mishima, H. Shimizu, G. Tomita, Y. Inoue, and Y. Kitazawa, "The prevalence of primary open-angle glaucoma in Japanese: The Tajimi Study," *Ophthalmology*, vol. 111, no. 9, pp. 1641–1648, Sep. 2004.

- [36] M. He, P. J. Foster, J. Ge, W. Huang, Y. Zheng, D. S. Friedman, P. S. Lee, and P. T. Khaw, "Prevalence and clinical characteristics of glaucoma in adult Chinese: a population-based study in Liwan District, Guangzhou," *Invest. Ophthalmol. Vis. Sci.*, vol. 47, no. 7, p. 2782, 2006.
- [37] Gordon MO, Beiser JA, Brandt JD, and et al, "The ocular hypertension treatment study: Baseline factors that predict the onset of primary open-angle glaucoma," *Arch. Ophthalmol.*, vol. 120, no. 6, pp. 714–720, Jun. 2002.
- [38] The AGIS Investigators, "The advanced glaucoma intervention study (AGIS): 7. the relationship between control of intraocular pressure and visual field deterioration," *Am. J. Ophthalmol.*, vol. 130, no. 4, pp. 429–440, Oct. 2000.
- [39] Heijl A, Leske M, Bengtsson B, and et al, "Reduction of intraocular pressure and glaucoma progression: Results from the early manifest glaucoma trial," *Arch. Ophthalmol.*, vol. 120, no. 10, pp. 1268–1279, Oct. 2002.
- [40] "Collaborative Normal Tension Glaucoma Study : Current Opinion in Ophthalmology," LWW. [Online]. Available: http://journals.lww.com/co-ophthalmology/Fulltext/2003/04000/Collaborative_Normal_Tension_Glaucoma_Study.6.aspx. [Accessed: 22-Jan-2016].
- [41] Leske M, Connell AS, Wu S, Hyman LG, and Schachat AP, "Risk factors for open-angle glaucoma: The barbados eye study," *Arch. Ophthalmol.*, vol. 113, no. 7, pp. 918–924, Jul. 1995.
- [42] J. J. Kanski and B. Bowling, *Synopsis of Clinical Ophthalmology*. Elsevier Health Sciences, 2012.
- [43] S. Asrani, R. Zeimer, J. Wilensky, D. Gieser, S. Vitale, and K. Lindenmuth, "Large diurnal fluctuations in intraocular pressure are an independent risk factor in patients with glaucoma.," *J. Glaucoma*, vol. 9, no. 2, pp. 134–142, 2000.
- [44] J. P. Berdahl, M. P. Fautsch, S. S. Stinnett, and R. R. Allingham, "Intracranial Pressure in Primary Open Angle Glaucoma, Normal Tension Glaucoma, and Ocular Hypertension: A Case–Control Study," *Invest. Ophthalmol. Vis. Sci.*, vol. 49, no. 12, pp. 5412–5418, Dec. 2008.
- [45] R. Ren, J. B. Jonas, G. Tian, Y. Zhen, K. Ma, S. Li, H. Wang, B. Li, X. Zhang, and N. Wang, "Cerebrospinal Fluid Pressure in Glaucoma: A Prospective Study," *Ophthalmology*, vol. 117, no. 2, pp. 259–266, Feb. 2010.
- [46] J. B. Jonas, E. Berenshtein, and L. Holbach, "Anatomic relationship between lamina cribrosa, intraocular space, and cerebrospinal fluid space," *Invest. Ophthalmol. Vis. Sci.*, vol. 44, no. 12, pp. 5189–5195, 2003.

- [47] W. H. Morgan, D.-Y. Yu, R. L. Cooper, V. A. Alder, S. J. Cringle, and I. J. Constable, "The influence of cerebrospinal fluid pressure on the lamina cribrosa tissue pressure gradient," *Invest. Ophthalmol. Vis. Sci.*, vol. 36, no. 6, pp. 1163–1172, 1995.
- [48] R. Ren, J. B. Jonas, G. Tian, Y. Zhen, K. Ma, S. Li, H. Wang, B. Li, X. Zhang, and N. Wang, "Cerebrospinal Fluid Pressure in Glaucoma: A Prospective Study," *Ophthalmology*, vol. 117, no. 2, pp. 259–266, 2010.
- [49] J. B. Jonas, N. L. Wang, D. Yang, R. Ritch, and S. Panda-Jonas, "Facts and Myths of Cerebrospinal Fluid Pressure for the Physiology of the Eye," *Prog. Retin. Eye Res.*
- [50] W. H. Morgan, B. C. Chauhan, D.-Y. Yu, S. J. Cringle, V. A. Alder, and P. H. House, "Optic disc movement with variations in intraocular and cerebrospinal fluid pressure," *Invest. Ophthalmol. Vis. Sci.*, vol. 43, no. 10, pp. 3236–3242, 2002.
- [51] D. Yang, J. Fu, R. Hou, K. Liu, J. B. Jonas, H. Wang, W. Chen, Z. Li, J. Sang, Z. Zhang, S. Liu, Y. Cao, X. Xie, R. Ren, Q. Lu, R. N. Weinreb, and N. Wang, "Optic Neuropathy Induced by Experimentally Reduced Cerebrospinal Fluid Pressure in Monkeys," *Invest. Ophthalmol. Vis. Sci.*, vol. 55, no. 5, pp. 3067–3073, May 2014.
- [52] J. G. Fujimoto, C. A. Puliafito, R. Margolis, A. Oseroff, S. De Silvestri, and E. P. Ippen, "Femtosecond optical ranging in biological systems," *Opt. Lett.*, vol. 11, no. 3, p. 150, Mar. 1986.
- [53] R. C. Youngquist, S. Carr, and D. E. N. Davies, "Optical coherence-domain reflectometry: a new optical evaluation technique," *Opt. Lett.*, vol. 12, no. 3, p. 158, Mar. 1987.
- [54] A. F. Fercher, K. Mengedocht, and W. Werner, "Eye-length measurement by interferometry with partially coherent light," *Opt. Lett.*, vol. 13, no. 3, p. 186, Mar. 1988.
- [55] D. Huang, E. A. Swanson, C. P. Lin, J. S. Schuman, W. G. Stinson, W. Chang, M. R. Hee, T. Flotte, K. Gregory, C. A. Puliafito, and J. G. Fujimoto, "Optical coherence tomography," *Science*, vol. 254, no. 5035, p. 1178, 1991.
- [56] S. Marschall, B. Sander, M. Mogensen, T. M. Jørgensen, and P. E. Andersen, "Optical coherence tomography—current technology and applications in clinical and biomedical research," *Anal. Bioanal. Chem.*, vol. 400, no. 9, pp. 2699–2720, May 2011.
- [57] W. Drexler and J. G. Fujimoto, "State-of-the-art retinal optical coherence tomography," *Prog. Retin. Eye Res.*, vol. 27, no. 1, pp. 45–88, Jan. 2008.
- [58] M. L. Gabriele, G. Wollstein, H. Ishikawa, L. Kagemann, J. Xu, L. S. Folio, and J. S. Schuman, "Optical Coherence Tomography: History, Current Status, and Laboratory Work," *Invest. Ophthalmol. Vis. Sci.*, vol. 52, no. 5, pp. 2425–2436, Apr. 2011.

- [59] M. Wojtkowski, R. Leitgeb, A. Kowalczyk, T. Bajraszewski, and A. F. Fercher, "In vivo human retinal imaging by Fourier domain optical coherence tomography," *J. Biomed. Opt.*, vol. 7, no. 3, pp. 457–463, 2002.
- [60] B. Hermann, E. J. Fernández, A. Unterhuber, H. Sattmann, A. F. Fercher, W. Drexler, P. M. Prieto, and P. Artal, "Adaptive-optics ultrahigh-resolution optical coherence tomography," *Opt. Lett.*, vol. 29, no. 18, pp. 2142–2144, Sep. 2004.
- [61] D. X. Hammer, R. D. Ferguson, M. Mujat, D. P. Biss, N. V. Iftimia, A. H. Patel, E. Plumb, M. Campbell, J. L. Norris, A. Dubra, and others, "Advanced capabilities of the multimodal adaptive optics imager," *Ophthalmic Technol. XXI Proc. SPIE*, vol. 7885, 2011.
- [62] M. Sarunic, M. A. Choma, C. Yang, and J. A. Izatt, "Instantaneous complex conjugate resolved spectral domain and swept-source OCT using 3x3 fiber couplers," *Opt. Express*, vol. 13, no. 3, pp. 957–967, 2005.
- [63] S. R. Chinn, E. A. Swanson, and J. G. Fujimoto, "Optical coherence tomography using a frequency-tunable optical source," *Opt. Lett.*, vol. 22, no. 5, pp. 340–342, Mar. 1997.
- [64] B. Potsaid, B. Baumann, D. Huang, S. Barry, A. E. Cable, J. S. Schuman, J. S. Duker, and J. G. Fujimoto, "Ultrahigh speed 1050nm swept source / Fourier domain OCT retinal and anterior segment imaging at 100,000 to 400,000 axial scans per second," *Opt. Express*, vol. 18, no. 19, pp. 20029–20048, Sep. 2010.
- [65] D. J. Fechtig, B. Grajciar, T. Schmoll, C. Blatter, R. M. Werkmeister, W. Drexler, and R. A. Leitgeb, "Line-field parallel swept source MHz OCT for structural and functional retinal imaging," *Biomed. Opt. Express*, vol. 6, no. 3, p. 716, Mar. 2015.
- [66] L. Kagemann, H. Ishikawa, G. Wollstein, P. M. Brennen, K. A. Townsend, M. L. Gabriele, and J. S. Schuman, "Ultrahigh-resolution Spectral Domain Optical Coherence Tomography Imaging of the Lamina Cribrosa," *Ophthalmic Surg. Lasers Imaging Off. J. Int. Soc. Imaging Eye*, vol. 39, no. 4 Suppl, pp. S126–S131, 2008.
- [67] E. J. Lee, T.-W. Kim, R. N. Weinreb, M. H. Suh, M. Kang, K. H. Park, S. H. Kim, and D. M. Kim, "Three-Dimensional Evaluation of the Lamina Cribrosa Using Spectral-Domain Optical Coherence Tomography in Glaucoma," *Invest. Ophthalmol. Vis. Sci.*, vol. 53, no. 1, pp. 198–204, Jan. 2012.
- [68] R. Inoue, M. Hangai, Y. Kotera, H. Nakanishi, S. Mori, S. Morishita, and N. Yoshimura, "Three-dimensional high-speed optical coherence tomography imaging of lamina cribrosa in glaucoma," *Ophthalmology*, vol. 116, no. 2, pp. 214–222, Feb. 2009.
- [69] B. Nuyen, K. Mansouri, and R. N. Weinreb, "Imaging of the Lamina Cribrosa using Swept-Source Optical Coherence Tomography," *J. Curr. Glaucoma Pract.*, vol. 6, no. 3, pp. 113–119, 2012.

- [70] S. Kiumehr, S. C. Park, D. Cyril, C. C. Teng, C. Tello, J. M. Liebmann, and R. Ritch, "In vivo evaluation of focal lamina cribrosa defects in glaucoma," *Arch. Ophthalmol.*, vol. 130, no. 5, pp. 552–559, May 2012.
- [71] J. Y. You, S. C. Park, D. Su, C. C. Teng, J. M. Liebmann, and R. Ritch, "Focal lamina cribrosa defects associated with glaucomatous rim thinning and acquired pits," *JAMA Ophthalmol.*, vol. 131, no. 3, pp. 314–320, Mar. 2013.
- [72] S. C. Park, A. T. Hsu, D. Su, J. L. Simonson, M. Al-Jumayli, Y. Liu, J. M. Liebmann, and R. Ritch, "Factors associated with focal lamina cribrosa defects in glaucoma," *Invest. Ophthalmol. Vis. Sci.*, vol. 54, no. 13, pp. 8401–8407, Dec. 2013.
- [73] C. Passmann and H. Ermert, "A 100-MHz ultrasound imaging system for dermatologic and ophthalmologic diagnostics," *IEEE Trans. Ultrason. Ferroelectr. Freq. Control*, vol. 43, no. 4, pp. 545–552, Jul. 1996.
- [74] "World Medical Association Declaration of Helsinki. Ethical principles for medical research involving human subjects.," *Bull. World Health Organ.*, vol. 79, no. 4, pp. 373–374, 2001.
- [75] J.-C. Mwanza, J. D. Oakley, D. L. Budenz, and D. R. Anderson, "Ability of Cirrus HD-OCT Optic Nerve Head Parameters to Discriminate Normal from Glaucomatous Eyes," *Ophthalmology*, vol. 118, no. 2, pp. 241–248.e1, Feb. 2011.
- [76] J.-C. Mwanza, R. T. Chang, D. L. Budenz, M. K. Durbin, M. G. Gendy, W. Shi, and W. J. Feuer, "Reproducibility of Peripapillary Retinal Nerve Fiber Layer Thickness and Optic Nerve Head Parameters Measured with Cirrus HD-OCT in Glaucomatous Eyes," *Invest. Ophthalmol. Vis. Sci.*, vol. 51, no. 11, pp. 5724–5730, Nov. 2010.
- [77] I. Grulkowski, J. J. Liu, B. Potsaid, V. Jayaraman, C. D. Lu, J. Jiang, A. E. Cable, J. S. Duker, and J. G. Fujimoto, "Retinal, anterior segment and full eye imaging using ultrahigh speed swept source OCT with vertical-cavity surface emitting lasers," *Biomed. Opt. Express*, vol. 3, no. 11, pp. 2733–2751, Oct. 2012.
- [78] M. F. Kraus, B. Potsaid, M. A. Mayer, R. Bock, B. Baumann, J. J. Liu, J. Hornegger, and J. G. Fujimoto, "Motion correction in optical coherence tomography volumes on a per A-scan basis using orthogonal scan patterns," *Biomed. Opt. Express*, vol. 3, no. 6, p. 1182, May 2012.
- [79] D. L. Budenz, P. Rhee, W. J. Feuer, J. McSoley, C. A. Johnson, and D. R. Anderson, "Sensitivity and specificity of the swedish interactive threshold algorithm for glaucomatous visual field defects1," *Ophthalmology*, vol. 109, no. 6, pp. 1052–1058, Jun. 2002.
- [80] I. A. Sigal, B. Wang, N. G. Strouthidis, T. Akagi, and M. J. A. Girard, "Recent advances in OCT imaging of the lamina cribrosa," *Br. J. Ophthalmol.*, vol. 98 Suppl 2, pp. ii34–ii39, Jul. 2014.

- [81] H.-Y. L. Park, S. H. Jeon, and C. K. Park, “Enhanced Depth Imaging Detects Lamina Cribrosa Thickness Differences in Normal Tension Glaucoma and Primary Open-Angle Glaucoma,” *Ophthalmology*, vol. 119, no. 1, pp. 10–20, Jan. 2012.
- [82] H. Ishikawa, D. M. Stein, G. Wollstein, S. Beaton, J. G. Fujimoto, and J. S. Schuman, “Macular Segmentation with Optical Coherence Tomography,” *Invest. Ophthalmol. Vis. Sci.*, vol. 46, no. 6, pp. 2012–2017, Jun. 2005.
- [83] J. S. Schuman, M. Hee, C. Puliafito, C. Wong, T. Pedut-Kloizman, C. Lin, E. Hertzmark, J. Izatt, E. Swanson, and J. Fujimoto, “Quantification of nerve fiber layer thickness in normal and glaucomatous eyes using optical coherence tomography,” *Arch. Ophthalmol.*, vol. 113, no. 5, pp. 586–596, May 1995.
- [84] J. M. Schmitt, S. H. Xiang, and K. M. Yung, “Speckle in Optical Coherence Tomography,” *J. Biomed. Opt.*, vol. 4, no. 1, pp. 95–105, 1999.
- [85] R. C. Gonzalez, *Digital image processing*. Pearson Education India, 2009.
- [86] K. Zuiderveld, “Contrast limited adaptive histogram equalization,” in *Graphics gems IV*, 1994, pp. 474–485.
- [87] W. Niblack, *An introduction to digital image processing*. Strandberg Publishing Company, 1985.
- [88] M. D. Abramoff, P. J. Magalhães, and S. J. Ram, “Image processing with ImageJ,” *Biophotonics Int.*, vol. 11, no. 7, pp. 36–42, 2004.
- [89] T. Hildebrand and P. Rügsegger, “A new method for the model-independent assessment of thickness in three-dimensional images,” *J. Microsc.*, vol. 185, no. 1, pp. 67–75, 1997.
- [90] M. Doube, M. M. Klosowski, I. Arganda-Carreras, F. P. Cordelières, R. P. Dougherty, J. S. Jackson, B. Schmid, J. R. Hutchinson, and S. J. Shefelbine, “BoneJ: Free and extensible bone image analysis in ImageJ,” *Bone*, vol. 47, no. 6, pp. 1076–1079, 2010.
- [91] Team RDC, “R: A language and environment for statistical computing,” *R Found. Stat. Comput.*, 2008.
- [92] S. Boker, M. Neale, H. Maes, M. Wilde, M. Spiegel, T. Brick, J. Spies, R. Estabrook, S. Kenny, T. Bates, P. Mehta, and J. Fox, “OpenMx: An Open Source Extended Structural Equation Modeling Framework,” *Psychometrika*, vol. 76, no. 2, pp. 306–317, Apr. 2011.
- [93] G. Dunn, *Design and analysis of reliability studies: The statistical evaluation of measurement errors*, vol. viii. London, England: Edward Arnold Publishers, 1989.
- [94] Z. Nadler, B. Wang, G. Wollstein, J. E. Nevins, H. Ishikawa, L. Kagemann, I. A. Sigal, R. D. Ferguson, D. X. Hammer, I. Grulkowski, J. J. Liu, M. F. Kraus, C. D. Lu, J. Hornegger, J. G. Fujimoto, and J. S. Schuman, “Automated lamina cribrosa

- microstructural segmentation in optical coherence tomography scans of healthy and glaucomatous eyes,” *Biomed. Opt. Express*, vol. 4, no. 11, pp. 2596–2608, Nov. 2013.
- [95] A. O. González-García, G. Vizzeri, C. Bowd, F. A. Medeiros, L. M. Zangwill, and R. N. Weinreb, “Reproducibility of RTVue Retinal Nerve Fiber Layer Thickness and Optic Disc Measurements and Agreement with Stratus Optical Coherence Tomography Measurements,” *Am. J. Ophthalmol.*, vol. 147, no. 6, pp. 1067–1074.e1, Jun. 2009.
- [96] L. A. Paunescu, J. S. Schuman, L. L. Price, P. C. Stark, S. Beaton, H. Ishikawa, G. Wollstein, and J. G. Fujimoto, “Reproducibility of Nerve Fiber Thickness, Macular Thickness, and Optic Nerve Head Measurements Using StratusOCT,” *Invest. Ophthalmol. Vis. Sci.*, vol. 45, no. 6, pp. 1716–1724, Jun. 2004.
- [97] J. Schindelin, I. Arganda-Carreras, E. Frise, V. Kaynig, M. Longair, T. Pietzsch, S. Preibisch, C. Rueden, S. Saalfeld, B. Schmid, J.-Y. Tinevez, D. J. White, V. Hartenstein, K. Eliceiri, P. Tomancak, and A. Cardona, “Fiji: an open-source platform for biological-image analysis,” *Nat. Methods*, vol. 9, no. 7, pp. 676–682, 2012.
- [98] J. L. Jaech, *Statistical analysis of measurement errors*. Wiley New York, 1985.
- [99] K. M. Ivers, C. Li, N. Patel, N. Sredar, X. Luo, H. Queener, R. S. Harwerth, and J. Porter, “Reproducibility of Measuring Lamina Cribrosa Pore Geometry in Human and Nonhuman Primates with In Vivo Adaptive Optics Imaging,” *Invest. Ophthalmol. Vis. Sci.*, vol. 52, no. 8, pp. 5473–5480, Jul. 2011.
- [100] T. Akagi, M. Hangai, K. Takayama, A. Nonaka, S. Ooto, and N. Yoshimura, “In Vivo Imaging of Lamina Cribrosa Pores by Adaptive Optics Scanning Laser Ophthalmoscopy,” *Invest. Ophthalmol. Vis. Sci.*, vol. 53, no. 7, pp. 4111–4119, Jun. 2012.
- [101] Dandona L, Quigley HA, Brown AE, and Enger C, “Quantitative regional structure of the normal human lamina cribrosa: A racial comparison,” *Arch. Ophthalmol.*, vol. 108, no. 3, pp. 393–398, Mar. 1990.
- [102] J. B. Jonas, C. Y. Mardin, U. Schlötzer-Schrehardt, and G. O. Naumann, “Morphometry of the human lamina cribrosa surface.,” *Invest. Ophthalmol. Vis. Sci.*, vol. 32, no. 2, pp. 401–405, 1991.
- [103] I. A. Sigal, J. L. Grimm, J. S. Schuman, L. Kagemann, H. Ishikawa, and G. Wollstein, “A method to estimate biomechanics and mechanical properties of optic nerve head tissues from parameters measurable using optical coherence tomography,” *IEEE Trans. Med. Imaging*, vol. 33, no. 6, pp. 1381–1389, Jun. 2014.
- [104] T.-W. Kim, L. Kagemann, M. J. A. Girard, N. G. Strouthidis, K. R. Sung, C. K. Leung, J. S. Schuman, and G. Wollstein, “Imaging of the lamina cribrosa in glaucoma: perspectives of pathogenesis and clinical applications,” *Curr. Eye Res.*, vol. 38, no. 9, pp. 903–909, Sep. 2013.

- [105] M. E. Nongpiur, J. Y. Ku, and T. Aung, “Angle closure glaucoma: a mechanistic review,” *Curr. Opin. Ophthalmol.*, vol. 22, no. 2, pp. 96–101, Mar. 2011.
- [106] V. A. Purvin, A. Kawasaki, and R. D. Yee, “Papilledema and obstructive sleep apnea syndrome,” *Arch. Ophthalmol.*, vol. 118, no. 12, pp. 1626–1630, 2000.
- [107] M. Wall and D. GEORGE, “Idiopathic intracranial hypertension,” *Brain*, vol. 114, no. 1, pp. 155–180, 1991.
- [108] D. I. Friedman and D. M. Jacobson, “Idiopathic intracranial hypertension,” *J. Neuroophthalmol.*, vol. 24, no. 2, pp. 138–145, 2004.
- [109] National Research Council (US) Committee for the Update of the Guide for the Care and Use of Laboratory Animals, *Guide for the Care and Use of Laboratory Animals*, 8th ed. Washington (DC): National Academies Press (US), 2011.
- [110] I. A. Sigal, J. G. Flanagan, I. Tertinegg, and C. R. Ethier, “Reconstruction of human optic nerve heads for finite element modeling,” *Technol. Health Care*, vol. 13, no. 4, pp. 313–329, 2005.
- [111] B. Wang, J. E. Nevins, Z. Nadler, G. Wollstein, H. Ishikawa, R. A. Bilonick, L. Kagemann, I. A. Sigal, I. Grulkowski, J. J. Liu, M. Kraus, C. D. Lu, J. Hornegger, J. G. Fujimoto, and J. S. Schuman, “In vivo lamina cribrosa micro-architecture in healthy and glaucomatous eyes as assessed by optical coherence tomography,” *Invest. Ophthalmol. Vis. Sci.*, vol. 54, no. 13, pp. 8270–8274, Dec. 2013.
- [112] B. Wang, J. E. Nevins, Z. Nadler, G. Wollstein, H. Ishikawa, R. A. Bilonick, L. Kagemann, I. A. Sigal, I. Grulkowski, J. J. Liu, M. Kraus, C. D. Lu, J. Hornegger, J. G. Fujimoto, and J. S. Schuman, “Reproducibility of in-vivo OCT measured three-dimensional human lamina cribrosa microarchitecture,” *PLoS ONE*, vol. 9, no. 4, p. e95526, Apr. 2014.
- [113] P. Wostyn, V. De Groot, D. Van Dam, K. Audenaert, and P. P. De Deyn, “The role of low intracranial pressure in the development of glaucoma in patients with Alzheimer’s disease,” *Prog. Retin. Eye Res.*, vol. 39, pp. 107–110, Mar. 2014.
- [114] J. P. Berdahl and R. R. Allingham, “Intracranial pressure and glaucoma:,” *Curr. Opin. Ophthalmol.*, vol. 21, no. 2, pp. 106–111, Mar. 2010.
- [115] Y. C. Fung, *Biomechanics*. New York, NY: Springer New York, 1990.
- [116] M. J. A. Girard, J.-K. F. Suh, M. Bottlang, C. F. Burgoyne, and J. C. Downs, “Scleral Biomechanics in the Aging Monkey Eye,” *Invest. Ophthalmol. Vis. Sci.*, vol. 50, no. 11, pp. 5226–5237, Nov. 2009.
- [117] J. C. Downs, C. F. Burgoyne, W. P. Seigfreid, J. F. Reynaud, N. G. Strouthidis, and V. Sallee, “24-Hour IOP Telemetry in the Nonhuman Primate: Implant System Performance

- and Initial Characterization of IOP at Multiple Timescales,” *Invest. Ophthalmol. Vis. Sci.*, vol. 52, no. 10, pp. 7365–7375, Sep. 2011.
- [118] R. S. Rogers, M. Dharsee, S. Ackloo, J. M. Sivak, and J. G. Flanagan, “Proteomics Analyses of Human Optic Nerve Head Astrocytes Following Biomechanical Strain,” *Mol. Cell. Proteomics*, vol. 11, no. 2, p. M111.012302, Feb. 2012.
- [119] R. P. Kirwan, C. H. Fenerty, J. Crean, R. J. Wordinger, A. F. Clark, and C. J. O’Brien, “Influence of cyclical mechanical strain on extracellular matrix gene expression in human lamina cribrosa cells in vitro,” *Mol Vis*, vol. 11, pp. 798–810, 2005.
- [120] A. W. Fryczkowski, B. S. Grimson, and R. L. P. Jr, “Scanning electron microscopy of vascular casts of the human scleral lamina cribrosa,” *Int. Ophthalmol.*, vol. 7, no. 2, pp. 95–100, Jun. 1984.
- [121] Tso MM and Hayreh S, “Optic disc edema in raised intracranial pressure: IV. Axoplasmic transport in experimental papilledema,” *Arch. Ophthalmol.*, vol. 95, no. 8, pp. 1458–1462, Aug. 1977.
- [122] M. J. Kupersmith, P. Sibony, G. Mandel, M. Durbin, and R. H. Kardon, “Optical Coherence Tomography of the Swollen Optic Nerve Head: Deformation of the Peripapillary Retinal Pigment Epithelium Layer in Papilledema,” *Invest. Ophthalmol. Vis. Sci.*, vol. 52, no. 9, pp. 6558–6564, Aug. 2011.
- [123] H. Tran, Y. Wang, B. Wang, G. Wollstein, M. A. Smith, L. Kagemann, H. Ishikawa, J. S. Schuman, E. Tyler-Kabara, and I. A. Sigal, “In-Vivo Lamellar and Scleral Canal Displacements During Acute Intracranial and Intraocular Pressure Elevation in Monkeys,” *Invest. Ophthalmol. Vis. Sci.*, vol. 56, no. 7, pp. 6150–6150, Jun. 2015.
- [124] I. A. Sigal, J. G. Flanagan, I. Tertinegg, and C. R. Ethier, “Finite Element Modeling of Optic Nerve Head Biomechanics,” *Invest. Ophthalmol. Vis. Sci.*, vol. 45, no. 12, pp. 4378–4387, Dec. 2004.
- [125] J. J. Corbett, P. J. Savino, H. S. Thompson, T. Kansu, N. J. Schatz, L. S. Orr, and D. Hopson, “Visual loss in pseudotumor cerebri: follow-up of 57 patients from five to 41 years and a profile of 14 patients with permanent severe visual loss,” *Arch. Neurol.*, vol. 39, no. 8, pp. 461–474, 1982.
- [126] E. J. Lee, T.-W. Kim, and R. N. Weinreb, “Reversal of lamina cribrosa displacement and thickness after trabeculectomy in glaucoma,” *Ophthalmology*, vol. 119, no. 7, pp. 1359–1366, Jul. 2012.
- [127] E. J. Lee, T.-W. Kim, M. Kim, and H. Kim, “Influence of Lamina Cribrosa Thickness and Depth on the Rate of Progressive Retinal Nerve Fiber Layer Thinning,” *Ophthalmology*, vol. 0, no. 0.

- [128] R. Inoue, M. Hangai, Y. Kotera, H. Nakanishi, S. Mori, S. Morishita, and N. Yoshimura, "Three-dimensional High-speed Optical Coherence Tomography Imaging of Lamina Cribrosa in Glaucoma," *Ophthalmology*, vol. 116, no. 2, pp. 214–222, Feb. 2009.
- [129] J. Albon, P. P. Purslow, W. S. S. Karwatowski, and D. L. Easty, "Age Related Compliance of the Lamina Cribrosa in Human Eyes," *Br. J. Ophthalmol.*, vol. 84, no. 3, pp. 318–323, Mar. 2000.
- [130] A. Kotecha, S. Izadi, and G. Jeffery, "Age-related changes in the thickness of the human lamina cribrosa," *Br. J. Ophthalmol.*, vol. 90, no. 12, pp. 1531–1534, Dec. 2006.
- [131] D. J. Tuite, P. a. F. H. Renström, and M. O'Brien, "The aging tendon," *Scand. J. Med. Sci. Sports*, vol. 7, no. 2, pp. 72–77, Apr. 1997.
- [132] J. Kohler, C. Popov, B. Klotz, P. Alberton, W. C. Prall, F. Haasters, S. Müller-Deubert, R. Ebert, L. Klein-Hitpass, F. Jakob, and others, "Uncovering the cellular and molecular changes in tendon stem/progenitor cells attributed to tendon aging and degeneration," *Aging Cell*, vol. 12, no. 6, pp. 988–999, 2013.
- [133] J. Uitto, "Connective tissue biochemistry of the aging dermis. Age-related alterations in collagen and elastin.," *Dermatol. Clin.*, vol. 4, no. 3, pp. 433–446, 1986.
- [134] J. Uitto, "The role of elastin and collagen in cutaneous aging: intrinsic aging versus photoexposure.," *J. Drugs Dermatol. JDD*, vol. 7, no. 2 Suppl, pp. s12–6, 2008.
- [135] G. Tezel, K. Trinkaus, and M. B. Wax, "Alterations in the morphology of lamina cribrosa pores in glaucomatous eyes," *Br. J. Ophthalmol.*, vol. 88, no. 2, pp. 251–256, Feb. 2004.
- [136] R. D. Fechtner and R. N. Weinreb, "Mechanisms of optic nerve damage in primary open angle glaucoma," *Surv. Ophthalmol.*, vol. 39, no. 1, pp. 23–42, Jul. 1994.
- [137] D. R. Anderson and A. Hendrickson, "Effect of Intraocular Pressure on Rapid Axoplasmic Transport in Monkey Optic Nerve," *Invest. Ophthalmol. Vis. Sci.*, vol. 13, no. 10, pp. 771–783, Oct. 1974.
- [138] Q. Harry and A. Earl, "Chronic experimental glaucoma in primates. II. Effect of extended intraocular pressure elevation on optic nerve head and axonal transport.," *Invest. Ophthalmol. Vis. Sci.*, vol. 19, no. 2, pp. 137–152, Feb. 1980.
- [139] J. E. Morgan, G. Jeffery, and A. J. E. Foss, "Axon deviation in the human lamina cribrosa," *Br. J. Ophthalmol.*, vol. 82, no. 6, pp. 680–683, Jun. 1998.
- [140] S. C. Park, C. G. V. De Moraes, C. C. Teng, C. Tello, J. M. Liebmann, and R. Ritch, "Enhanced Depth Imaging Optical Coherence Tomography of Deep Optic Nerve Complex Structures in Glaucoma," *Ophthalmology*, vol. 119, no. 1, pp. 3–9, Jan. 2012.

- [141] E. J. Lee, T. W. Kim, R. N. Weinreb, K. H. Park, S. H. Kim, and D. M. Kim, "Visualization of the lamina cribrosa using enhanced depth imaging spectral-domain optical coherence tomography," *Am. J. Ophthalmol.*, vol. 152, no. 1, pp. 87–95, 2011.
- [142] D. S. Minckler and M. O. Tso, "A light microscopic, autoradiographic study of axoplasmic transport in the optic nerve head during ocular hypotony, increased intraocular pressure, and papilledema.," *Am. J. Ophthalmol.*, vol. 82, no. 5, pp. 741–757, Nov. 1976.
- [143] I. A. Sigal and C. R. Ethier, "Biomechanics of the optic nerve head," *Exp. Eye Res.*, vol. 88, no. 4, pp. 799–807, Apr. 2009.
- [144] L. Kagemann, B. Wang, G. Wollstein, H. Ishikawa, J. E. Nevins, Z. Nadler, I. A. Sigal, R. A. Bilonick, and J. S. Schuman, "IOP Elevation Reduces Schlemm's Canal Cross-sectional Area," *Invest. Ophthalmol. Vis. Sci.*, Feb. 2014.
- [145] M. Pakravan, A. Parsa, M. Sanagou, and C. F. Parsa, "Central corneal thickness and correlation to optic disc size: a potential link for susceptibility to glaucoma," *Br. J. Ophthalmol.*, vol. 91, no. 1, pp. 26–28, Jan. 2007.
- [146] J. Albon, W. S. Karwatowski, N. Avery, D. L. Easty, and V. C. Duance, "Changes in the collagenous matrix of the aging human lamina cribrosa.," *Br. J. Ophthalmol.*, vol. 79, no. 4, pp. 368–375, Apr. 1995.
- [147] M. J. A. Girard, L. Zimmo, E. T. White, J. M. Mari, C. R. Ethier, and N. G. Strouthidis, "Towards a Biomechanically-Based Diagnosis for Glaucoma: In Vivo Deformation Mapping of the Human Optic Nerve Head," *ASME Proc.*, pp. 423–424, Jun. 2012.
- [148] C. Bowd, L. M. Zangwill, C. C. Berry, E. Z. Blumenthal, C. Vasile, C. Sanchez-Galeana, C. F. Bosworth, P. A. Sample, and R. N. Weinreb, "Detecting Early Glaucoma by Assessment of Retinal Nerve Fiber Layer Thickness and Visual Function," *Invest. Ophthalmol. Vis. Sci.*, vol. 42, no. 9, pp. 1993–2003, Aug. 2001.
- [149] J. M. Mari, N. G. Strouthidis, S. C. Park, and M. J. A. Girard, "Enhancement of lamina cribrosa visibility in optical coherence tomography images using adaptive compensation," *Invest. Ophthalmol. Vis. Sci.*, vol. 54, no. 3, pp. 2238–2247, Mar. 2013.